Propagation and Scattering of High-Intensity X-Ray Pulses in Dense Atomic Gases and Plasmas

Dissertation zur Erlangung des Doktorgrades
an der Fakultät für Mathematik, Informatik und Naturwissenschaften
Fachbereich Physik
der Universität Hamburg

vorgelegt von
Clemens Weninger

Hamburg, 2015

Tag der Disputation: 06.10.2015
Folgende Gutachter empfehlen die Annahme der Dissertation:
Dr. Nina Rohringer
Prof. Dr. Wilfried Wurth

In memory of my dear mother Helga Weninger

$\star$ 1957 † 2012

Abstract

Nonlinear spectroscopy in the x-ray domain is a promising technique to explore the dynamics of elementary excitations in matter. X-rays provide an element specificity that allows them to target individual chemical elements, making them a great tool to study complex molecules. The recent advancement of x-ray free electron lasers (XFELs) allows to investigate non-linear processes in the x-ray domain for the first time. XFELs provide short femtosecond x-ray pulses with peak powers that exceed previous generation synchrotron x-ray sources by more than nine orders of magnitude. This thesis focuses on the theoretical description of stimulated emission processes in the x-ray regime in atomic gases. These processes form the basis for more complex schemes in molecules and provide a proof of principle for nonlinear x-ray spectroscopy. The thesis also includes results from two experimental campaigns at the Linac Coherent Light Source and presents the first experimental demonstration of stimulated x-ray Raman scattering.

Focusing an x-ray free electron laser beam into an elongated neon gas target generates an intense stimulated x-ray emission beam in forward direction. If the incoming x-rays have a photon energy above the neon K edge, they can efficiently photo-ionize 1s electrons and generate short-lived core excited states. The core-excited states decay mostly via Auger decay but have a small probability to emit a spontaneous x-ray photon. The spontaneous emission emitted in forward direction can stimulate x-ray emission along the medium and generate a highly directional and intense x-ray laser pulse.

If the photon energy of the incoming x-rays however is below the ionization edge in the region of the pre-edge resonance the incoming x-rays can be inelastically scattered. This spontaneous x-ray Raman scattering process has a very low probability, but the spontaneously scattered photons in the beginning of the medium can stimulate Raman scattering along the medium. The scattering signal can thus be amplified by several orders of magnitude.

To study stimulated x-ray emission a generalized one-dimensional Maxwell-Bloch model is developed. The radiation is propagated through the medium with the help of the Maxwell equations and the radiation is coupled to the atomic system via the polarization. The atomic system is treated in the density matrix formalism and the time evolution of the coherences determine the polarization of the medium.

Zusammenfassung

Nichtlineare Spektroskopie im Röntgenbereich ist eine vielversprechende Technik, um die Dynamik von elementaren Anregungen in Materie zu erforschen. Die Wechselwirkung von Röntgenstrahlen mit Materie ist elementspezifisch und ermöglicht es individuelle chemische Elemente anzusprechen. Diese Eigenschaft ist besonders hilfreich, um komplexe Moleküle zu untersuchen. Der jüngste Fortschritt bei Freie-Elektronen-Lasern ermöglicht es zum ersten Mal nichtlineare Prozesse im Röntgenbereich zu untersuchen. Freie-Elektronen-Laser erzeugen Femtosekunden Röntgenpulse mit einer Maximalleistung, die vorherige Synchrotron Strahlungsquellen um neun Größenordnungen übertrifft. Diese Arbeit behandelt die theoretische Beschreibung von stimulierter Emission im Röntgenbereich von atomaren Gasen. Diese Prozesse bilden die Basis für komplexere Methoden in Molekülen und dienen als Machbarkeitsbeweis für nichtlineare Spektroskopie im Röntgenbereich. Die Arbeit enthält außerdem Resultate von zwei experimentellen Kampagnen an der Linac Coherent Light Source and präsentiert die erste experimentelle Demonstration von stimulierter Raman-Streuung im Röntgenbereich.

Ein Freie-Elektronen-Laser Puls, der in ein langgezogenes Gas Medium fokussiert wird, erzeugt einen intensiven Strahl aus stimulierter Emission im Röntgenbereich in Vorwärtsrichtung. Wenn die Photonenenergie der einkommenden Röntgenstrahlung über der K-Absorptionskante in Neon liegt, können die Röntgenstrahlen kurzlebige hochangeregte Zustände durch effiziente Photoionisation von 1s Elektronen erzeugen. Diese angeregten Zustände zerfallen hauptsächlich durch Auger-Zerfall, aber haben eine geringe Wahrscheinlichkeit, ein spontanes Röntgenphoton zu emittieren. Die spontane Emission in Vorwärtsrichtung kann die Emission von weiteren Röntgenphotonen entlang des Mediums stimulieren and einen intensiven Röntgenlaser Puls erzeugen.

Wenn die Photonenenergie des einkommenden Pulses allerdings knapp unterhalb der Ionisationskante in der Gegend der Resonanzen liegt, können die Röntgenstrahlen inelastisch gestreut werden. Diese spontane Raman-Streuung hat nur eine geringe Wahrscheinlichkeit, aber die spontan gestreuten Photonen am Anfang des Mediums können den Streuprozess im weiteren Medium stimulieren. Durch die stimulierte Raman-Streuung kann das Streusignal um mehrere Größenordnungen verstärkt werden.

Um die stimulierte Emission im Röntgenbereich zu untersuchen, wird ein generalisiertes eindimensionales Maxwell-Bloch Model entwickelt. Die Strahlung wird dabei mit Hilfe der Maxwell-Gleichungen durch das Medium propagiert und über die Polarisation an das atomare System gekoppelt. Das atomare System wird als Dichtematrix behandelt and die Zeitentwicklung der Kohärenzen bestimmt die Polarisation des Mediums.

List of publications

[1] **Stimulated Electronic X-Ray Raman Scattering**
Clemens Weninger, Michael Purvis, Duncan Ryan, Richard A. London, John D. Bozek, Christoph Bostedt,Alexander Graf, Gregory Brown, Jorge J. Rocca, and Nina Rohringer
Phys. Rev. Lett. **111**, 233902 (2013).

[2] **Stimulated resonant x-ray Raman scattering with incoherent radiation**
Clemens Weninger and Nina Rohringer
Phys. Rev. A **88**, 053421 (2013).

[3] **Transient-gain photoionization x-ray laser**
Clemens Weninger and Nina Rohringer
Phys. Rev. A **90**, 063828 (2014).

Contents

Chapter 1

Introduction

Since their discovery in 1895 by Wilhelm Conrad Röntgen x-rays have had a huge impact on science and are widely used in many areas ranging from physics, chemistry and biology to medical applications. X-rays are electromagnetic radiation with a short wavelength which can be comparable to the interatomic distances in molecules. This property makes them suitable to resolve the atomic structure of molecules via x-ray diffraction techniques. X-rays also have an element specificity that allows them to pump and probe specific elements and electronic shells. They are furthermore sensitive to the chemical environment and can reveal information about the oxidation state and chemical bonds. X-ray spectroscopy techniques have become vital methods in atomic and molecular physics as well as in solid-state physics and allow to study a wide range of phenomena.

The widespread use of x-rays in science and technology has driven the development of new x-ray radiation sources. X-ray sources have come a long way since the first x-ray tubes and the available x-ray flux and photon energy range have grown significantly over the last century. X-ray sources have recently experienced a revolution with the availability of x-ray free electrons lasers (XFELs). The first short wavelength free electron laser (FEL) to become operational was FLASH at DESY in Hamburg in 2005. FLASH is operating in the soft x-ray regime up to around 300 eV photon energy. In 2009 the Linac Coherent Light Source (LCLS) in Menlo Park, California went into operation and provides x-rays with photon energies of up to 10 keV. These large scale facilities provide x-ray pulses with femtosecond pulse duration and unprecedented brightness that exceeds 3rd generation storage-ring based x-ray sources by nine orders of magnitude.

Free-electron lasers facilitate a broad variety of different research areas [4], including

coherent diffractive imaging [5–8], matter in extreme conditions [9, 10], material science to study excitations in condensed matter systems [11–13] and catalysis in chemical reactions [14, 15].

The high intensity of XFELs allows for the first time to investigate the non-linear response of matter to x-ray radiation and to observe stimulated emission processes involving inner-shell transitions. Non-linear effects in the optical domain have been studied to a great extent due to the availability of high power optical lasers. The transfer of these non-linear effects to the x-ray domain has not been possible so far and only recently become feasible with the advance of the XFEL. This development leads to the emergence of non-linear spectroscopy in the x-ray domain. This thesis is dedicated to exploring the path towards non-linear spectroscopy in the x-ray domain as a viable tool for probing matter.

The predominant process in x-ray matter interaction in the soft x-ray regime up to a photon energy of several keV is single photon ionization [16]. An example of a non-linear process, involving the interaction with more than one x-ray photon, is multiple sequential photo-ionization. Exposing neon to x-ray intensities of $10^{18}\,\mathrm{W\,cm^{-2}}$ with a photon energy of 2 keV strips neon of all its 10 electrons by a sequence of inner shell photo-ionization and Auger decays [16]. At such high intensities the atoms can absorb multiple x-ray photons despite the femtosecond pulse duration and produce highly charged ions. In heavy atoms such as xenon the absorption of 8 x-ray photons with 1.5 keV photon energy leads to charge states as high as Xe^{36+} [17]. The efficient photo ionization of matter leads to severe radiation damage. The positively charged ions repel each other and lead to a Coulomb explosion of the molecules. This process provides a big challenge in x-ray scattering to resolve the atomic structure of big molecules before they disintegrate [18, 19].

Another example of a non-linear process is the formation of inner-shell double-core holes [20]. Inner shell photo-ionization leads to the formation of very short lived core holes that decay via Auger decay or fluorescence. If the x-ray intensity is sufficient a second core hole can be created before the first one decayed. The formation of double core-holes has been recently demonstrated in krypton [21]. The 1s single core-holes have a lifetime of only 170 attoseconds in krypton and the double core-holes have been observed by x-ray fluorescence measurements. Further recently observed non-linear processes include two-photon absorption at 5.6 keV by germanium [22], x-ray and

optical sum frequency generation [23] and second harmonic generation [24].

This thesis lays the groundwork for non-linear spectroscopy in the x-ray domain. The work presents a detailed theoretical study on stimulated x-ray emission and stimulated inelastic x-ray scattering from atoms. These are the building blocks for more complicated schemes in atoms and molecules and provide a proof of principle for non-linear x-ray spectroscopy. The thesis furthermore includes results from two experimental campaigns to demonstrate the feasibility of stimulated x-ray emission from dense atomic gases. The ultimate goal of nonlinear x-ray spectroscopy is to resolve complex dynamics involving multiple electronic and vibrational degrees of freedom with high spatial and temporal resolution. These dynamics are especially important for energy transport in light harvesting complexes and chemical dynamics in catalytic reactions [15, 25, 26]. The weak cross section of non-linear effects in the x-ray regime though provides a serious challenge.

1.1. X-ray free-electron lasers

X-ray free-electron lasers (XFELs) are novel, powerful x-ray sources that allow to study physical processes on length and time scales that have not been accessible with previous x-ray sources. XFELs exceed current synchrotron radiation sources in peak brilliance by nine orders of magnitude and can provide femtosecond x-ray pulses with up to 20 keV photon energy with around 10^{12} photons per pulse. Free-electron lasers were proposed in the 1970s [27] to generate tunable and high-power short wavelength radiation with femtosecond pulse durations.

Free-electron lasers are based on linear particle accelerators to generate high quality relativistic electron beams that pass through a periodic transverse magnetic field (undulator) to emit short wavelength radiation [28–32]. The magnetic field forces the electrons to wiggle in the transverse direction and emit spontaneous undulator radiation. The wavelength λ_r of the emitted radiation depends on the wiggler strength K and the period λ_u of the magnetic field in the undulator and the electron kinetic energy [33, 34, 32]

$$\lambda_r = \frac{\lambda_u}{2\gamma_0^2}(1 + K^2)\,. \tag{1.1}$$

The dimensionless wiggler strength K is proportional to the magnitude of the magnetic

field and the wiggler period. The Lorentz factor γ_0 is proportional to the kinetic energy of the electrons. It appears squared due to the combination of two different relativistic effects that shorten the emission wavelength. The relativistic moving electrons see a shorter undulator period contracted by γ_0 due to Lorentz contraction. Furthermore, the emitted radiation from the relativistic moving electrons gets a relativistic Doppler shift when transforming it into the laboratory frame.

For a sufficiently long undulator and a tightly collimated electron beam the interaction between the electrons and the emitted radiation leads to a periodic modulation of the electron density in the beam in longitudinal direction. This micobunching effect leads to a coherent emission and an exponential amplification of the initial spontaneous emission. This microbunching effect is the reason for the huge increase in emitted x-ray power from free-electron lasers compared to spontaneous undulator radiation. The coherent emission from the microbunches makes the radiated power proportional to the number of electrons squared N^2. For the incoherent spontaneous undulator radiation the radiated power only grows linearly with the number of electrons N.

Since the initial spontaneous undulator radiation from shot noise in the electron bunch seeds the amplification process, the generated x-ray radiation has a very poor temporal (longitudinal) coherence with a broadband, noisy spectrum. This self amplified spontaneous emission (SASE) has large shot to shot fluctuations of the pulse shape and the emission spectrum along with shifts of the central wavelength [35, 36]. FEL pulses have a high degree of spatial (transversal) coherence [37, 38], making them a good radiation source for x-ray imaging and diffraction. The high spatial coherence also allows for a very good focusing of the x-ray beam with sub-µm spot sizes [39, 40]. Despite the possibility of generating sub-10fs x-ray pulses, time resolved experiments with free-electron lasers are challenging. The relative arrival time of the FEL pulses is not stable and can vary by several hundreds of femtoseconds from shot to shot[41]. This arrival time jitter severely limits the time resolution in pump probe experiments with an external laser source. Synchronization of the FEL to laser sources [42] or arrival time measurements of the FEL pulse [43] are necessary to obtain time resolution beyond the arrival time jitter of the FEL.

There are several different schemes to improve the temporal coherence and stability of FEL radiation. One approach is to use an external coherent seed pulse for the amplification process [44–46]. If the external seed pulse is stronger than the spontaneous

undulator radiation the coherent seed is going to be amplified rather than the noise. This scheme is limited to the extreme ultraviolet regime (XUV) due to the lack of coherent x-ray sources at short wavelength. High harmonics from high power optical lasers are typically used as external seed pulse. Another approach to produce stable and narrowband FEL pulses is x-ray self-seeding. For this the first undulator segments are used to generate undulator radiation. The undulator radiation then passes through a monochromator to select a narrow band of the spectrum for further amplification. The filtered, narrowband and coherent radiation is then superimposed with the electron bunch again to act as a seed for the amplification in the remaining part of the undulator [47, 48].

Free-electron lasers require large-scale facilities and long linear particle accelerators. In traditional particle accelerators the electrons are accelerated in microwave cavities by electromagnetic fields. The microwave cavities can typically sustain acceleration gradients of several 10 MV/m. To obtain electron beams with GeV energies, necessary for hard x-ray generation, the linear accelerators have to be at least several hundred meters long. The undulators to generate the high power x-ray radiation can also span several hundred meters. The size and cost of these big facilities is one of the major drawback of free-electron lasers. There is a lot of development underway to make FELs more compact by using a different mechanism to accelerate the electrons to build table top facilities [49–51]. With the advance of high power optical lasers it is possible to generate GeV electron beams by laser-plasma acceleration. In this technique the huge electric fields in the plasma between the ions and electrons provide acceleration gradients on the GV/m scale. These huge acceleration gradients allow for very compact electron accelerators that are 1000 times shorter than conventional accelerators based on microwave cavities [52, 53]. Spontaneous undulator radiation in the soft x-ray regime from laser-plasma accelerated electron bunches has already been observed [54]. The quality of the laser-plasma accelerated electron beam in terms of energy spread, emittance and bunch charge is however not yet sufficient to obtain coherent x-ray emission from the electron bunches.

There are several free-electron laser facilities in user operation around the world. The first FEL facility to be available for experiments is FLASH [55, 56] at DESY in Hamburg, Germany since 2005. The 84 meter long superconducting accelerator generates electron bunches with up to 1.25 GeV kinetic energy. This FEL operates

in the VUV regime up to the carbon K-edge (284.2 eV, 4.36 nm) and operates in the SASE mode. A recent update FLASH II will also provide seeded FEL pulses by injecting high harmonic generated radiation as a seed pulse. The first user facility in the hard x-ray regime is the Linac Coherent Light Source (LCLS) [57] in Menlo Park, CA. The LCLS utilizes one-third of the 2-mile-long Stanford linear accelerator to accelerate electrons to energies of up to 14 GeV. The LCLS has a repetition rate of 120 Hz and provides photon energy spanning the soft x-ray regime from around 280 eV to the hard x-ray regime at around 10 keV with pulse energies of up to 2 mJ. The LCLS provides several beamlines to address a variety of different x-ray techniques and sample environments. The only other hard x-ray FEL facility currently in operation is SACLA [58] in Japan. SACLA provides around a factor of ten less x-ray flux compared to LCLS. FERMI@Elettra [59] in Trieste, Italy is a XUV seeded-FEL facility. High harmonic generation is used for seeding and the available photon energy ranges from 12 eV up to 124 eV.

There are several new FEL facilities under construction at the moment including the SwissFEL at the Paul Scherrer Institute in Switzerland and the European XFEL in Hamburg, Germany. The European XFEL consists of a 1.7 km long superconducting linear accelerator to provide a high repetition rate of up to 27 kHz and feed multiple undulators at the same time. The facility is supposed to start user operation in 2017 and provide an increase in x-ray peak brilliance by a factor of 10 compared to current XFELs.

The development of XFEL radiation sources finally opens up the opportunity to explore stimulated emission processes in the x-ray regime. Using the XFEL radiation to either photo-ionize inner-shell electrons or resonantly excite them to unoccupied orbitals leads to different emission processes. The following sections introduce the concept of stimulated x-ray emission from atoms following ionization (x-ray laser) and for resonant excitation (stimulated resonant inelastic scattering).

1.2. Atomic x-ray laser

Since the demonstration of the first optical laser by Ted Maiman in 1960 [60], scientists have been striving for lasers with shorter emission wavelength. Lasers are based on the principle of stimulated emission where an excited state in an atom can decay by interaction with a resonant photon, emitting an additional photon with identical

properties. In order for a medium to amplify radiation by stimulated emission the population of the excited state has to exceed the population of the lower lying final state. To achieve this population inversion, energy has to be injected into the system to bring a large population of electrons into the excited state.

To reach shorter emission wavelengths the energy separation between excited and final state has to be increased which results in a reduction of the excited state lifetime. This increases the necessary pump power to obtain a population inversion in the medium. The required pump power for stimulated emission thereby scales with $P_{\text{pump}} \propto \lambda^{-5}$ [61] for lifetime-broadened transitions and illustrates the challenge of short emission wavelength lasers. There is also a lack of efficient normal incidence x-ray mirrors, making a multi-pass x-ray laser cavity unfeasible. The idea is therefore to build single pass x-ray amplifiers by pumping elongated cylindrical plasmas to stimulate x-ray emission along the elongated direction of the plasma.

There are several methods to generate a population inversion in the amplification medium. The most direct approach is to use an intense x-ray source to photo-ionize inner shell electrons. This photo-ionization x-ray laser approach has been proposed since the 1960s [62–66]. Another approach is to pump a medium with one or more powerful optical lasers to produce a hot dense plasma and generate the population inversion by collisional excitation or recombination of electrons. The first laboratory lasers in the extreme ultraviolet (EUV) were demonstrated in 1984 [67, 68] with wavelengths of around 20 nm. Pumping thin foils of Tantalum MacGowan et al. demonstrated the first x-ray laser in the water window with a wavelength of 4.4 nm [69]. Using a transient collisional excitation scheme with two powerful pump lasers the efficiency of x-ray lasers can be increased [70]. These plasma based x-ray lasers provide laboratory scale table top x-ray sources. Jorge Rocca's group has pioneered the work on table top x-ray sources [71, 72] and demonstrated saturated x-ray emission down to 13.2 nm from nickel-like cadmium Cd^{+20} [71] with x-ray intensities up to $10^{10}\,\mathrm{W\,cm^{-2}}$.

The requirement of a very intense and short pump pulse has been the main challenge to achieve x-ray lasing on atomic transitions in the photo-ionization lasing scheme. With the advancement of free-electron lasers these intense pump sources are finally available and atomic x-ray lasers in the keV regime are feasible [73, 74]. Rohringer and coworkers demonstrated the first photo-ionization inner shell x-ray laser [75]. Using the LCLS free-electron laser to pump neon they showed exponential amplification of neon

K-α emission at 1.43 nm. In the experiment x-ray pulses from the LCLS were focused into a high pressure gas cell filled with neon. The XFEL pulse generates an elongated narrow plasma column with a transient population inversion between core electrons and valence electrons in neon. The core holes decay mostly via Auger decay, but have a small probability of undergoing fluorescence decay and emitting a spontaneous x-ray photon. The spontaneous emission process acts as a seed for the stimulated emission cascade along the narrow plasma column. The spontaneous emitted photons in the beginning of the gas cell that travel in forward direction along with the XFEL pulse can trigger stimulated emission processes in the inverted medium. This results in the exponential amplification of the initial seed photons and generates an intense, highly directed x-ray beam in forward direction.

1.3. Stimulated x-ray Raman scattering

Nonlinear spectroscopy is a powerful technique to study the dynamics of elementary excitations in matter. Nonlinear spectroscopy requires high intensities to trigger nonlinear responses in the system which can reveal additional information compared to linear spectroscopy. Linear spectroscopy typically gives information about excited state populations, absorption and transition dipoles. Nonlinear spectroscopy on the other hand can also probe quantum coherences [76] and allows to distinguish between homogeneous and inhomogeneous line broadening [77]. Nonlinear spectroscopy in the infrared and optical domain is a well established method and is used for vibrational analysis of biological and chemicals samples using coherent Raman scattering microscopy [78–83] and multidimensional spectroscopy [84–89].

These techniques require multiple tunable and coherent laser pulses. Due to great progress in laser technology these pulses are available in the infrared, optical and also UV domain. In the x-ray domain these coherent multi-pulse radiation sources are not available. X-ray spectroscopy has several benefits compared to optical spectroscopy. An advantage of x-ray spectroscopy is the element and orbital sensitivity due to the distinct binding energies of electronic shells in atoms and molecules. Fig. 1.1 shows the absorption cross section for Carbon and Iron as a function of photon energy. The curves show absorption edges where there is a big sudden increase in the absorption cross section. These jumps occur if the x-ray photon energy is big enough to access the next more tightly bound electronic shell. These absorption edges are specific for every

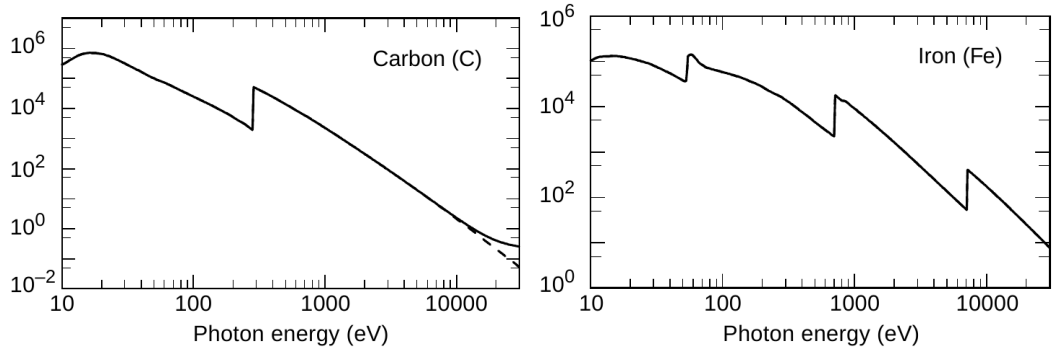

Figure 1.1.: X-ray absorption coefficients for Carbon and Iron [90].

chemical element and electronic shell. The Carbon K-edge binding energy of 1s core electrons is 284 eV. For the heavier Iron atom the K-edge is at 7.1 keV, the L_1 for 2s electrons is at 844 eV and the M_1 shell for 3s electrons is at 91 eV. Due to the element specificity x-rays can be used to excite and probe only certain elements and electronic shells in atoms and molecules. X-ray spectroscopy also provides chemical sensitivity. Fig. 1.2 shows the x-ray absorption near edge structure for different silver compounds at the silver L-edge. The different chemical environments influence the absorption cross

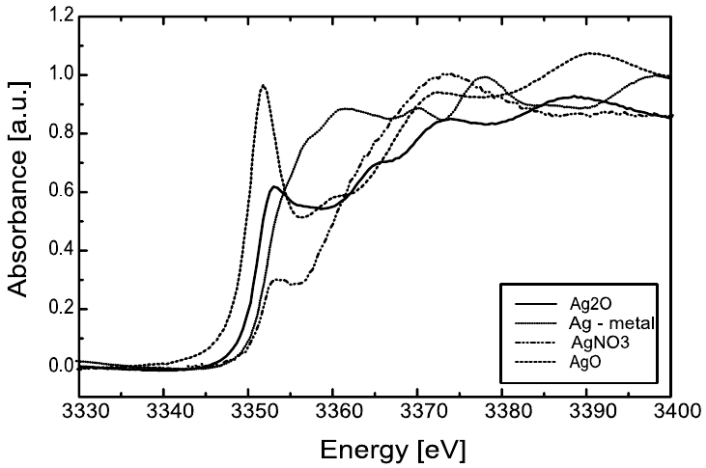

Figure 1.2.: X-ray absorption near edge structure for different silver compounds at the silver L-edge. Reprinted from "Solid-state NMR and XANES studies of lithium and silver silicate gels synthesized by the sol–gel route", J. Non-Cryst. Solids. **318**, A.A. Mrsea, P.L. Bryanta, F.J. Hormesb, L.G. Butlera, N. Satyanarayanac, B. Rambabu, 296 [91]. Copyright ©(2003), with permission from Elsevier.

section of the silver L-shell. X-rays can thus be used to probe the chemical environment. Due to the much smaller wavelength of x-rays compared to optical radiation, they can provide higher spatial resolution in diffraction experiments. X-rays also have a much higher penetration depth and can be used to probe optically thick samples. These favorable characteristics makes an extension of nonlinear spectroscopy to the x-ray regime a promising approach. Shaul Mukamel has laid the theoretical foundation for nonlinear spectroscopy in the x-ray domain [92, 76, 93, 94].

X-ray Raman scattering (XRS) is the inelastic scattering of x-rays where the energy of the outgoing scattered radiation is different from the incoming energy. The technique is frequently used to probe elementary excitations in condensed matter systems [95–100] and to determine chemical decompositions of samples [101]. In resonant XRS

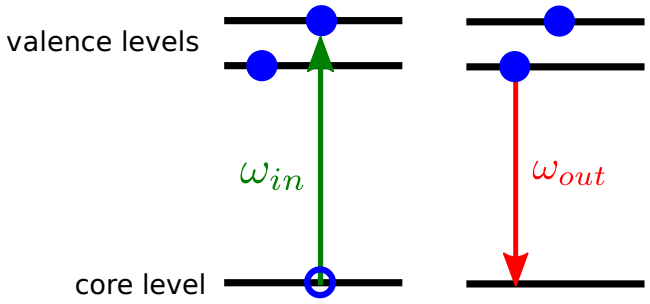

Figure 1.3.: Basic mechanism of resonant inelastic x-ray scattering. The incoming x-rays with photon energy ω_{in} resonantly excite a core electron to an unoccupied valence orbital. This intermediate state can then decay by emitting a x-ray photon with photon energy ω_{out}.

core-electrons are resonantly excited to unoccupied valence orbitals. This core-excited intermediate state can decay via Auger decay or by emitting a scattered red-shifted x-ray photon, see Fig. 1.3. The difference between the incoming photon energy and the outgoing photon energy is left in the system as an excitation. The spontaneous XRS process probes the unoccupied valence orbitals as well as the population of the occupied valence orbitals. In Raman scattering the excitation process and the emission process are coherently connected and form a single inelastic scattering event. This leads to unique characteristics that are not present in x-ray fluorescence where the process of absorption and emission are not directly linked to each other. One main feature of Raman scattering is the direct relation between the incoming and the outgoing photon energy. The outgoing energy is equal to the difference between the incoming photon

energy ω_{in} and the transition energy between final and ground-state ω_{f0}

$$\omega_{out} = \omega_{in} - \omega_{f0}\,. \tag{1.2}$$

The linear dispersion between incoming and outgoing radiation in resonant XRS was demonstrated by Eisenberger et al. in Copper in 1976 [102]. They scanned narrowband synchrotron radiation around the Copper K edge and studied the emission as a function of the incoming photon energy. For incoming energies above the K edge they observed fluorescence at a fixed emission energy. For resonant excitation below the K edge they however observed a linear dependence between the scattered photon energy and the incoming photon energy.

The Raman process can be stimulated by providing photons on the emission transition between intermediate and final state. The process is then called stimulated Raman scattering. This can be done by providing two pulses that cover the spectral region for excitation and emission respectively. Another possibility is to use a single broadband pulse that covers both transitions, called impulsive Raman scheme. In an elongated medium the scattering process can be self stimulated. This means the spontaneous Raman scattering in the beginning of the medium will stimulate the scattering process further along in the medium. The stimulation of the scattering process can increase the scattering signal by several orders of magnitude. The stimulation also confines the emission into a predominant direction with a narrow divergence, which allows to collect most of the scattering signal. In spontaneous Raman scattering on the other hand there is no predominant direction for emission and the signal is distributed in a much larger solid angle. The stimulation therefore allows to measure weak scattering signals that would not be visible without amplification.

1.4. Outline

Part I of this thesis presents the theoretical modeling of stimulated x-ray emission in neon. Chapter 2 introduces the setup to obtain stimulated x-ray emission from dense atomic gases along with the semi-classical Maxwell-Bloch model to describe these processes. In the theoretical model the electromagnetic radiation is described by a classical field and the atomic system is represented by a density matrix. The electric field and the atomic system are coupled via the polarization to obtain a self-consistent

system. The Maxwell equations are introduced and the wave equation for the emitted x-ray radiation is derived. Afterwards numerical methods to solve the time evolution of the atomic system are presented. The spontaneous emission can be modeled by adding a random source term to the polarization. The structure and properties of the spontaneous source term are derived in section 2.4.2. Another important aspect for describing stimulated x-ray emission with XFEL radiation sources are the properties of the pump radiation. The properties of self amplified spontaneous emission (SASE) radiation and how to model those stochastic pulses are presented in 2.4.3.

Chapter 3 presents a theoretical study of stimulated K-α fluorescence in neon. The chapter uncovers that the amplification by stimulated emission for a transient gain x-ray amplifier with short upper state lifetime varies from other amplifiers. It furthermore presents a comparison between the Maxwell-Bloch model and the widely used rate equation approach. The spectral line shape of the emitted radiation is studied along with the influence of the pump radiation on the amplification process. In the last part of the chapter the statistical properties and coherence of the stimulated emission are analyzed.

Chapter 4 presents a theoretical study of stimulated x-ray Raman scattering in neon for resonant excitation with an XFEL pulse. Using broadband x-ray radiation to excite neon results in an overlap of K-α fluorescence and stimulated Raman scattering making it difficult to distinguish between the two types of emission. The developed theoretical model includes both kind of emission processes. This allows to identify the unique characteristics of the x-ray Raman scattering that sets it apart from the amplified spontaneous emission. In addition the chapter presents a detailed analysis of the scattering line shape when pumping with incoherent SASE radiation.

Part II presents the results from experimental campaigns at the x-ray free electron laser LCLS. Chapter 5 presents the first experimental demonstration of stimulated resonant electronic x-ray Raman scattering and demonstrates the feasibility of stimulated x-ray Raman scattering with present day x-ray sources. The chapter introduces the methods for data analysis and presents an online monitoring software that was developed to obtain real time feedback on measured data at LCLS.

Part I.

Theoretical modeling of stimulated x-ray emission

Chapter 2

Stimulated x-ray emission from atomic gases

The following chapter introduces the theoretical basis and numerical techniques to describe stimulated x-ray emission in atoms. Atomic units are used throughout this thesis if not noted otherwise. In atomic units the reduced Planck constant $\hbar$, the electron mass m_e and the electric charge $|e|$ are all set to one $\hbar = m_e = |e| = 1$. The fine structure constant is determined by $\alpha = \frac{e^2}{\hbar c} \approx \frac{1}{137}$. Atomic units are abbreviated with [a.u.] whereas arbitrary units are abbreviated by [arb. units]. In this thesis it is assumed that the x-rays only interact with the electrons. The nuclei are too heavy ($m_n > 938\,\mathrm{MeV}$) to react to the high-frequency x-ray radiation compared to the light electrons ($m_e = 511\,\mathrm{keV}$). The photon energies considered in this work are also far below any nuclear resonances [103]. The interaction of electrons with x-rays is vastly different from the interaction with low energy radiation in the optical domain. Figure 2.1 compares the interaction of atoms with strong field optical radiation to the interaction with x-rays. In the optical domain the energy of a single photon is not sufficient to overcome the electron binding energy and to eject the electron from the atom. When the strength of the electric field from the optical radiation is comparable to the binding potential of the electron it can strongly modulate the binding potential. The modulation of the binding potential can allow the electron to tunnel through the barrier and escape the atom [104], see Figure 2.1a). In strong optical fields it is also possible to absorb multiple photons to overcome the binding energy and photo-ionize the atom as shown in Figure 2.1b). Figure 2.1c) shows the interaction of electrons with x-ray radiation which is dominated by single photon ionization [16]. The photon energy of a single x-ray photon is already sufficient to overcome the electron binding

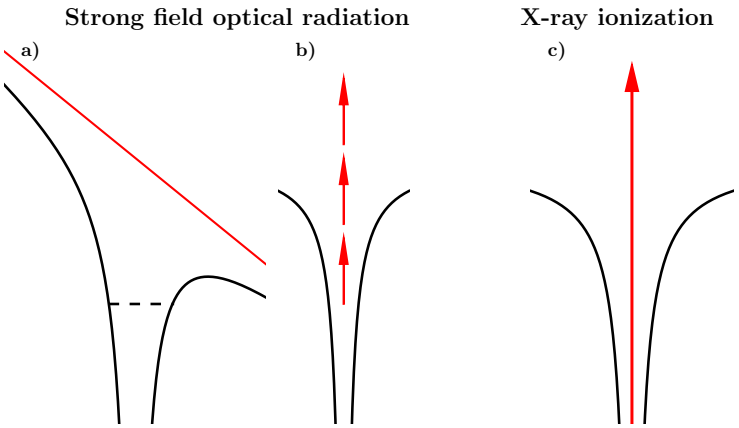

Figure 2.1.: Interaction of atoms with strong field optical radiation compared to x-ray radiation. a) depicts tunnel ionization where the black curve shows the atomic potential superimposed with the potential of the optical radiation (red line). b) shows the process of multi-photon absorption to photo-ionize a valence electron from the atoms. c) depicts single-photon ionization with a x-ray photon from a deeply bound core level.

energy and to photo-ionize atoms.

To model the x-ray matter interaction a semi-classical Maxwell-Bloch description is utilized. In this approach the emitted x-ray radiation is described by a classical electric field and the atomic system is modeled by the density matrix. The atomic system and the radiation are coupled via the polarization to allow a self consistent solution of the coupled systems. The following section describes the setup and the geometry to obtain stimulated emission from gases with XFEL pump radiation. Afterwards the atomic structure of neon and the density matrix are introduced along with the relevant excitation processes. The following section then presents the Maxwell equations to describe the evolution of the emitted radiation. The chapter ends with numerical methods to solve the x-ray matter interaction.

2.1. Setup

In the experiment [75, 1] x-ray pulses from the LCLS were focused into a 10 mm long gas cell filled with neon at pressures of 500 Torr. The XFEL focus size was around 1-2 µm, resulting in an elongated and narrow cylindrical interaction volume of x-rays

and gas. Fig. 2.2 illustrates the setup to obtain stimulated x-ray emission from neon. The neon gas is acting as a single-pass amplifying medium. The absence of normal incidence mirrors makes it unfeasible to generate multi-pass amplifiers in the x-ray domain. The density length product of gas cell length and neon gas density therefore

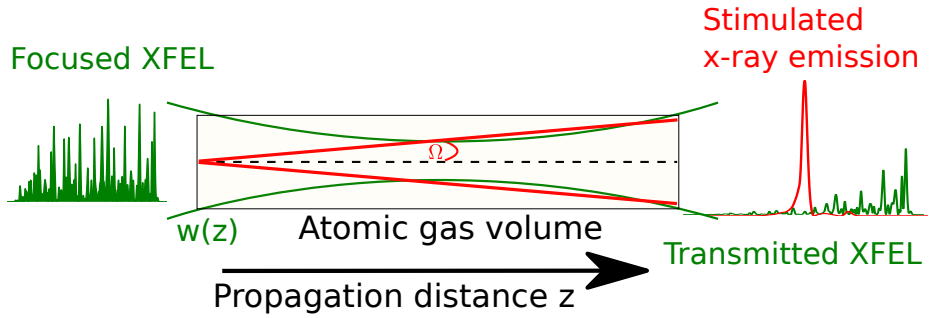

Figure 2.2.: Geometry for amplified x-ray emission in neon along a narrow cylindrical gas medium. The curved green lines marks the beam waist $w(z)$ of the XFEL pulse and the angle Ω illustrates the maximum divergence angle of the stimulated emission beam with respect to the propagation axis.

has to be sufficiently large to significantly amplify the stimulated emission along the propagation direction in a single pass. This specific geometry allows to reduce the propagation of the radiation in the theoretical modeling to a one dimensional problem to a good approximation. Neglecting the transverse dimensions works well in this case, because the length along the gas cell is more then 1000 times larger than the transverse dimension. This means that the x-rays propagate along the axis of the gas cell and the angle Ω (see fig. 2.2) with respect to the propagation distance is limited to very small values.

Despite the simplified one dimensional model it is still possible to incorporate the changing beam waist of the focused XFEL beam. When the XFEL beam is focused into the gas cell its beam waist $w(z)$ changes as a function of the propagation distance z. At the Linac Coherent Light Source the Rayleigh range for a focus size of several µm is comparable to the gas cell length of 10 mm. For a smaller focus size in the nm regime the Rayleigh range however becomes quite small and is only around 100 µm. In a one dimensional model the changing beam waist can be included by rescaling the scalar intensity of the XFEL at every step along the propagation direction with the beam waist at that position.

A one dimensional model is able to describe the variation of the pulses along the propagation distance and is also able to account for the different propagation velocities of the XFEL pulse and the emitted stimulated emission when propagating through a dense gas medium. These are the most important physical effects and make the one dimensional model a good approximation to study stimulated x-ray emission from elongated gas media. The one-dimensional model also already achieves an excellent agreement with experimental results [1]. Nevertheless an extension of the one-dimensional model to include the transverse dimensions would be useful. In the one-dimensional model it is not possible to predict spatial properties of the emitted x-ray radiation. To study the beam divergence and spatial coherence of the stimulated emission a treatment of the transverse dimensions is required. In this thesis however only the one-dimensional model is considered.

2.2. Atomic structure of neon

Neon is a noble gas with 10 electrons distributed over the closed shells 1s, 2s, 2p. The electron binding energy for the K shell (1s) is 870.2 eV, for the L_1 shell (2s) 48.5 eV and for the L_2 shell (2p) 21.7 eV. Figure 2.3 shows the photo-ionization cross section

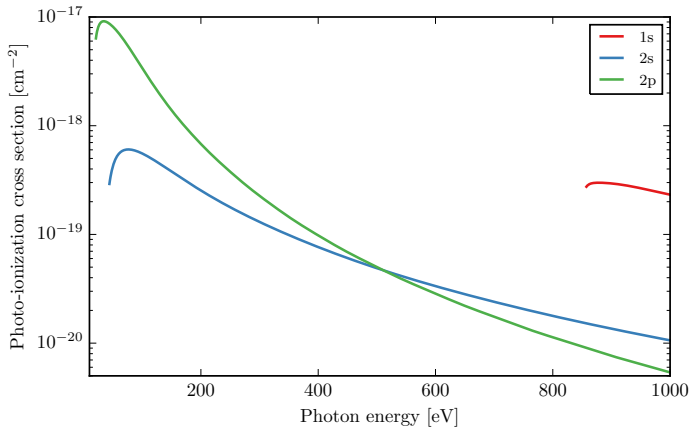

Figure 2.3.: Photo-ionization cross sections for the different electronic shells in neon as a function of the photon energy.

for the different electronic shells in neon. The plot illustrates that above the neon K-edge the 1s photo-ionization cross section is more than 10 times higher than the 2p

valence photo-ionization cross section.

Focusing an XFEL pulse with a photon energy above the neon K-edge into the neon gas thus generates a population inversion between 1s core electrons and the 2p electrons. The 1s core holes decay mostly via Auger decay with a lifetime of 2.4 femtoseconds. In the Auger decay process an outer shell electrons fills the core-hole vacancy and the excess energy is transferred to another electron which is ejected from the ion. This non-radiative Auger decay is a competing decay mechanism to the slow fluorescence decay with a lifetime of 160 femtoseconds in neon. In the fluorescence decay the core hole is also filled by a valence electron but the energy is released as a x-ray photon. This high fluorescence lifetime compared to the Auger decay means that only 1.5% of the core-excited atoms emit a spontaneous x-ray photon.

Zooming in on the absorption cross section around the neon K-edge reveals the pre-edge resonances, see Figure 2.4. These pre-edge resonances describe the transfer of

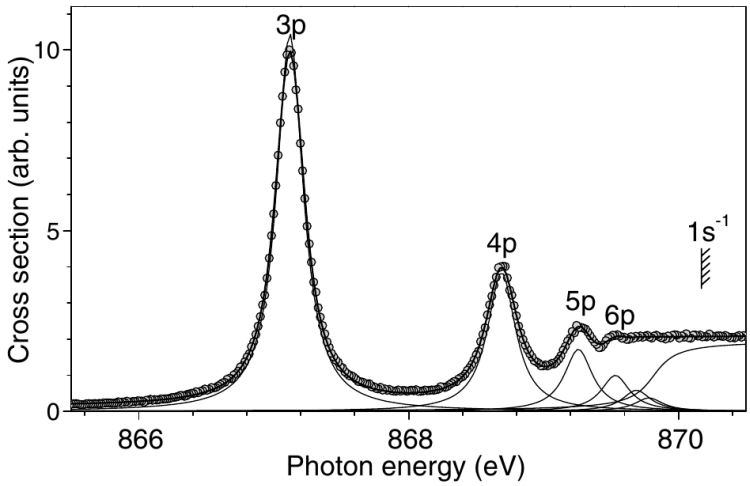

Figure 2.4.: Neon absorption cross section around the K-edge. Reprinted figure with permission from A. De Fanis et al. *Phys. Rev. Lett.* **89**, 243001 (2002) [105]. Copyright ©(2002) by the American Physical Society.

1s core-electrons to unoccupied valence orbitals that lie close to the continuum. The strongest pre-edge resonance in the 1s-3p resonance at 867.5 eV, followed by the 1s-4p resonance at 869.2 eV. The energy difference between consecutive resonances and their strength decrease as the upper levels increases and they form a so called Rydberg series.

Figure 2.5 summarizes the atomic system and its processes for resonant excitation

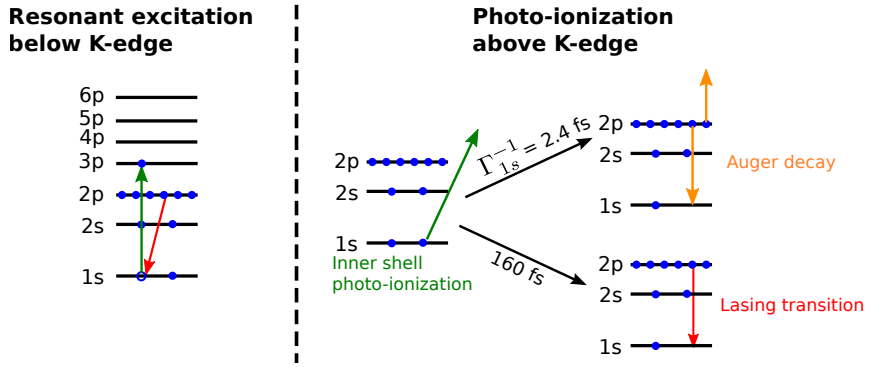

Figure 2.5.: Level system in neon for resonant excitation below the K-edge (left side) and photo-ionization above the K-edge (right side).

below the K-edge and for excitation above the neon K-edge. In the case of resonant excitation the atomic system consists of the initial groundstate neon configuration and the unoccupied valence orbitals. The model includes the unoccupied levels from the 3p to the 6p shell. Higher lying resonances are too close to the K-edge to be clearly identified as pre-edge resonances. For the case of above edge excitation the atomic system consists of the initial neon groundstate configuration and the core-excited and valence excited states in the singly charged neon ion.

The Hamiltonian of the system is given by

$$\hat{H} = \hat{H}_0 + \hat{H}_{\text{int}} \tag{2.1}$$

where $\hat{H}_0$ is the unperturbed Hamiltonian of the atomic system in a mean field approximation and $\hat{H}_{\text{int}}$ describes the interaction of the atom with the external x-ray field. The atomic system can be described by the wavefunction $|\Psi, t\rangle$ that is expanded in the groundstate $|\phi_0\rangle$ and single particle hole excitations $|\phi_i^a\rangle$

$$|\Psi, t\rangle = \alpha_0(t)\, \mathrm{e}^{-iE_0 t}\, |\phi_0\rangle + \sum_{i,a} \alpha_i^a(t)\, \mathrm{e}^{-iE_i^a t}\, |\phi_i^a\rangle\,, \tag{2.2}$$

where $\alpha_0(t)$ and $\alpha_i^a(t)$ are time-dependent expansion coefficients for the respective state. The wavefunction can be transformed from the Schrödinger picture to the interaction picture which provides a more convenient description of the problem. In the interaction picture only the time evolution due to the interaction Hamiltonian $\hat{H}_{\text{int}}$ is retained in

the wavefunction and the time evolution due to $\hat{H}_0$ is transferred to the operators.

$$|\Psi, t\rangle_I = \mathrm{e}^{i\hat{H}_0 t}\,|\Psi, t\rangle = \alpha_0(t)\,|\phi_0\rangle + \sum_{i,a} \alpha_i^a(t)\,|\phi_i^a\rangle\,, \tag{2.3}$$

The single-particle hole excitations are constructed by

$$|\phi_i^a\rangle = \frac{1}{\sqrt{2}}\left(\hat{b}_{a\uparrow}^\dagger\,\hat{b}_{i\uparrow} + \hat{b}_{a\downarrow}^\dagger\,\hat{b}_{i\downarrow}\right)|\phi_0\rangle \tag{2.4}$$

where $\hat{b}_i$ annihilates an electron from an initially occupied orbital and $\hat{b}_a^\dagger$ creates an electron in an initially unoccupied orbital. The total spin is preserved in the interaction and therefore only spin-singlet states are considered. This expansion is convenient because it allows to treat the resonant excitation and the above edge excitation with the same formalism. The excitation in the single particle hole excitation can be a resonance or a state in the continuum in the case of photo-ionization. For the description of stimulated emission the state of the photo-ionized electron in the continuum is not relevant, as the photo-electron is not observed. By using the density matrix formalism we can retain the subsystem that is relevant for modeling stimulated emission processes and discard the photo-electron [106, 1]. The reduced density matrix for the singly charged ion is given by

$$\rho_{j,k}^{1+}(t) = \sum_{c\,\in\,\mathrm{cont.}} \alpha_j^c(t)\,\alpha_k^{c\star} \tag{2.5}$$

where the sum $\sum_c$ goes over all states of the photo-electron in the continuum. This reduced density matrix describes the state of the remaining ion after photo-ionization. The time evolution for the reduced ionic density matrix is derived in chapter 3.

In the case of resonant excitation where the upper state is a discrete state the density matrix for the neutral atom is defined by

$$\rho_{j,k}^a = \alpha_j^a \alpha_k^{a\star} \tag{2.6}$$

The case of resonant excitation is discussed in chapter 4.

2.3. Maxwell equations

The emitted x-ray radiation is modeled as an electric field and its evolution can be derived from the classical Maxwell equations. The Maxwell equations [107] for the electric and magnetic field in SI units for a polarizable media without conductivity are

$$\nabla \cdot E = 0 \tag{2.7}$$

$$\nabla \cdot B = 0 \tag{2.8}$$

$$\nabla \times H = \epsilon_0 \frac{\partial E}{\partial t} + \frac{\partial P}{\partial t} \tag{2.9}$$

$$\nabla \times E = -\mu_0 \frac{\partial H}{\partial t}\,, \tag{2.10}$$

where H is the magnetic field, E is the electric field, P is the polarization of the medium, μ_0 is the magnetic permeability and ϵ_0 is the dielectric constant. In this case the contribution of free charges and electric currents to the fields is neglected and only the polarization of the medium influences the field. This model thus discards any effects from free electrons in the plasma that is generated by the XFEL pulse in the gas. This approach is justified for the low density gas media considered in this thesis. For higher density targets like clusters [108] and solid targets [109] the free electrons can rescatter the x-ray radiation.

Taking the curl of eq. 2.10 and inserting it into eq. 2.9 yields the second order wave equation for the electric field

$$\nabla^2 E - \frac{1}{c^2}\frac{\partial^2 E}{\partial t^2} = \mu_0 \frac{\partial^2 P}{\partial t^2}\,, \tag{2.11}$$

were $\nabla^2 E$ is the spatial Laplacian and describes second order spatial derivatives of the electric field E. The two first order Maxwell equations can therefore be transformed into a single second order differential equation for the electric field. A similar equivalent wave equation can be obtained for the magnetic field H.

Assuming a linear polarized wave propagating in the z direction with a wave vector k, the electric field can be decomposed into a complex envelope $\mathcal{E}$ and a fast oscillating exponent describing the propagation in forward direction

$$E(t) = \frac{1}{2}\left\{\mathcal{E}(t)\,\mathrm{e}^{i(kz-\omega t)} + \mathcal{E}^{\star}(t)\,\mathrm{e}^{-i(kz-\omega t)}\right\}\,. \tag{2.12}$$

The same decomposition can be made for the polarization P and its envelope $\mathcal{P}$.

$$P(t) = \frac{1}{2}\left\{\mathcal{P}(t)\,\mathrm{e}^{i(kz-\omega t)} + \mathcal{P}^{\star}(t)\,\mathrm{e}^{-i(kz-\omega t)}\right\}. \tag{2.13}$$

The physical electric field $E(t)$ is a real valued function whereas the envelope $\mathcal{E}$ is complex because it includes amplitude as was well as phase information. This decomposition is useful because we are only interested in the envelope of the field and not the fast oscillations of the carrier. In the x-ray regime a pulse with a photon energy of 1 keV has a carrier oscillation period of 4.1 attoseconds. Typical x-ray pulses from XFELs are at least several femtoseconds long and therefore contain several thousand optical cycles. Changes in the envelope are thus much smaller than the carrier frequency ω. This allows to perform the slowly varying envelope approximation, which neglects second order derivatives with respect to the envelope

$$\frac{\partial^2 \mathcal{E}}{\partial z^2} \ll k\frac{\partial \mathcal{E}}{\partial z}$$
$$\frac{\partial^2 \mathcal{E}}{\partial t^2} \ll \omega\frac{\partial \mathcal{E}}{\partial t}$$

Inserting the expansion for the electric field eq. 2.12 into the wave equation 2.11 and performing the slowly varying envelope approximation yields

$$\frac{\partial \mathcal{E}}{\partial z} + \frac{1}{c}\frac{\partial \mathcal{E}}{\partial t} = i\frac{\mu_o \omega^2}{2k}\mathcal{P}\,. \tag{2.14}$$

Equation 2.14 is a first order differential equation for the electric field envelope $\mathcal{E}$ describing a wave propagating in the positive z direction. Here the transverse derivatives of the electric field are neglected and only the derivative in propagation direction is considered. The elongated geometry of the gas medium (fig. 2.2) allows to only consider wave propagating along the z-direction.

Typically the field has to be propagated over long distances of several mm, which makes solving eq.2.14 directly difficult due to numerical errors in the propagation. Transforming into a frame moving along with the pulse with the retarded time ($\tau = t - \frac{z}{c}$) results in

$$\frac{\partial \mathcal{E}(\tau, z)}{\partial z} = i\frac{2\pi\omega}{c}\mathcal{P} \tag{2.15}$$

The pulse envelope is now stationary in the moving frame and is only influenced by the polarization. This equation is numerically much easier to solve than eq. 2.14 and avoids the problem of numerical dispersion [110] that occurs in pulse propagation. The numerical dispersion is an artifact from solving the differential equation on a discrete grid and results in a wavelength dependent propagation velocity for the electric field.

2.4. Numerical methods

2.4.1. Time evolution of the density matrix

The following section describes numerical methods to solve the time evolution of the density matrix introduced in section 2.2. There is a wealth of numerical approaches available to solve this problem. The time evolution of the density matrix is governed by the Liouville-von Neumann equation [111]

$$\partial_t \rho = -i[H, \rho] + Q(\rho)\,. \tag{2.16}$$

This is a first order differential equation for the density matrix ρ with two different terms on the right hand side. The first term $[H, \rho]$ is the commutator between the interaction Hamiltonian and the density matrix. This term describes the unitary time evolution of the density matrix due to the Hamiltonian H. To include other decay processes phenomenological relaxation terms are introduced by the linear operator $Q(\rho)$ [112]. This term can describe phenomena like Auger decay, photo-ionization and collisions. The density matrix ρ fulfills special properties that should be conserved during propagation. The density matrix is a Hermitian operator with $\rho = \rho^\dagger$. The diagonal elements of the density matrix describe the probability to find the system in that respective state and should therefore be in the interval [0, 1].

Eq. 2.16 is an ordinary first order differential equation and can in principle be solved by general methods for ordinary differential equations (ODE). But these general methods would not explicitly preserve the special properties of ρ and might lead to unphysical solutions. General methods are also not very efficient for this kind of problem and have a low order of convergence [113]. Common general methods for solving eq. 2.16 are Runge-Kutta methods and Crank–Nicolson schemes, but Bidégaray et al. [112] showed that these methods violate positiveness for the diagonal elements of

ρ and negative populations were observed. They instead proposed a split-step method [112, 114] to solve equation 2.16. In the split step method each term on the right hand side of the ODE is integrated separately and the partial solutions are then combined for the total solution. This approach is advantageous when the individual parts can be solved easier and more efficiently than the combined right hand side of the ODE. Solving the terms independently though introduces a splitting error. The increased accuracy of the individual solutions can however outweigh the introduced splitting error. Splitting equation 2.16 into two equations yields

$$\partial_t \rho = Q(\rho) \tag{2.17}$$

$$\partial_t \rho = -i[H, \rho] \tag{2.18}$$

Since Q is a linear operator the first equation has the solution

$$\rho(t + \Delta t) = \exp(Q\Delta t)\rho(t)\,. \tag{2.19}$$

The second part has the solution

$$\rho(t + \Delta t) \approx \exp(iH\Delta t)\,\rho(t)\,\exp(-iH\Delta t)\,. \tag{2.20}$$

This solution is exact for a time independent Hamiltonian but replacing the time dependent Hamiltonian H(t) with a constant value over the interval Δt introduces a discretization error. The total error of the solution is however typically dominated by the error in calculating the matrix exponential $\exp(iH\Delta t)$ [113]. For this solution the exponential of a Hermitian matrix has to be computed. There are many different ways to calculate matrix exponentials [115] depending on the matrix and its size. One possibility is to expand the matrix exponential in Chebychev polynomials. A disadvantage of this method is that the upper and lower bound of the spectrum of the matrix has to be known [116]. Depending on the problem it can be difficult to obtain an accurate value for these values which reduces the efficiency of this approach. Another approach which is very popular for large sparse matrices are Krylov subspace methods [117]. Here the matrix exponential is expanded in a much smaller subspace and the matrix exponential is directly calculated in the subspace. For small matrices the matrix exponential can be calculated by calculating the eigen

decomposition of the Hamiltonian $H = U\,D\,U^{-1}$, where D is a diagonal matrix with the eigenvalues and U is the matrix of eigenvectors. With this the matrix exponential becomes $\exp(iH\Delta t) = U\ \exp(iD\Delta t)\,U^{-1}$. The exponential of the diagonal matrix D is trivial to compute and is simply the exponential of the individual entries on the diagonal. Because the Hamiltonian is time dependent the eigen decomposition has to be calculated at every time step, making this method computationally expensive. The eigen decomposition scales with the matrix dimension cubed $\mathcal{O}(N^3)$ and thus only works for fairly small matrices. The maximum matrix size that is considered in this thesis is $N = 13$ and thus makes the eigen decomposition feasible. The eigen decomposition scheme is thus used for all following computations.

Now that the two terms are solved independently they have to be combined to obtain the total solution. Using a Strang splitting scheme [112] the complete solution of $\rho(t + \Delta t)$ is computed by first taking half a time step of solution 2.19, followed by a full time step of 2.20 and another half time step of solution 2.19

$$\rho(t + \Delta t) = \mathrm{e}^{Q\Delta t/2}\,\mathrm{e}^{iH\Delta t}\,\left(\mathrm{e}^{Q\Delta t/2}\,\rho(t)\right)\,\mathrm{e}^{-iH\Delta t}\,. \tag{2.21}$$

The splitting error introduced by this scheme is on the order of $\mathcal{O}(\Delta t^4)$.

2.4.2. Spontaneous emission modeling

In spontaneous emission an atom in an excited state can decay to an energetically lower state by emission of a photon. The emitted photon has a random phase and propagates in a random direction, in contrast to stimulated emission. In the x-ray regime the probability for spontaneous emission in light elements is very low and inner-shell holes decay predominantly via Auger decay.

Spontaneous emission is a quantum effect and can only be explained by quantum electrodynamics (QED) where the electromagnetic field is quantized as well. The coupling of the vacuum fluctuations of the quantized electromagnetic field to the excited state enable a radiative decay without an external electric field. The Weisskopf-Wigner theory predicts an exponential decay of the excited state due to spontaneous emission [118]. This exponential decay results in a Lorentzian line shape for the spontaneous emission.

The classical Maxwell equations thus do not include spontaneous emission. Nevertheless the spontaneous emission can be modeled with the classical Maxwell equations

by including a random source term to the polarization. In the following an appropriate random source term for spontaneous emission is derived. The term should reproduce the Lorentzian spectrum of spontaneous emission and generate the amount of spontaneous emission that corresponds to the fluorescence rate. Following the approach presented in [109] the source term can be derived from the following simplified equations for the electric field envelope E and the polarization P. Taking equation 2.14 at a fixed point in space and assuming an exponential decay for the polarization leads to

$$\frac{dE(t)}{dt} = \alpha P(t) \tag{2.22}$$

$$\frac{dP(t)}{dt} = -\beta P(t) + S(t)\,, \tag{2.23}$$

where S is the random source term, β is the decay constant of the polarization and $\alpha = i2\pi\omega$ is a proportionality constant from the Maxwell equations. This model neglects any spatial dependence of the spontaneous emission.

In this approach the spontaneous emission from the different atoms is assumed to be uncorrelated in time. The spontaneous emission is an incoherent process and the correlation function for the source term can be modeled as a delta function in time with a normalization constant F

$$< S(t_1)^{\star} S(t_2) >= F\delta(t_1 - t_2)\,, \tag{2.24}$$

where the brackets $<>$ denote the ensemble average over many realizations of the random term S. The distribution for S is assumed to be stationary and to have a zero mean $< S(t) >= 0$. The term S is a Gaussian white noise term, which means it has a flat frequency response over a broad range. This kind of mimics the continuum of modes from the vacuum fluctuations in QED.

To determine normalization constant F the rate $\frac{d|E|^2}{dt}$ due to the source term S has to be computed. Equation 2.23 can be solved and yields the following solution

$$P(t) = P(0)\mathrm{e}^{-\beta t} + \int_0^t \mathrm{e}^{-\beta(t-t')} S(t')\, dt'\,. \tag{2.25}$$

With the solution for $P(t)$ the correlation function for the polarization can be calculated

and one obtains

$$< P(t_1)^\star P(t_2) >= \frac{F}{2\beta} \mathrm{e}^{-\beta|t_1-t_2|} \,. \tag{2.26}$$

With the help of the correlation function for the polarization the rate $\frac{d|E|^2}{dt}$ can be determined from equation 2.22

$$\frac{d|E|^2}{dt} = E^\star \frac{dE}{dt} + E \frac{dE^\star}{dt} = \alpha P E^\star + \text{c.c} \tag{2.27}$$

Taking the ensemble average of eq. 2.27 results in

$$\frac{d}{dt} < |E|^2 >= \alpha < PE^* > + \text{c.c} \tag{2.28}$$

The correlation function on the right side $< PE^* >$ can be calculated with the help of the formal solution for the electric field.

$$E(t) = \alpha \int_{-\infty}^{t} P(t')dt' \tag{2.29}$$

inserting this solution into equation 2.28 yields

$$< PE^* >= \alpha \int_{-\infty}^{t} < P^*(t')P(t) > dt' = \alpha \int_{-\infty}^{t} \frac{F}{2\beta} \mathrm{e}^{-\beta|t'-t|} dt' = \alpha \frac{F}{2\beta^2} \tag{2.30}$$

This correlation function can be inserted back into equation (2.28) to obtain the final result

$$\frac{d}{dt} < |E|^2 >= \frac{|\alpha|^2 F}{\beta^2} \,. \tag{2.31}$$

The energy density W of the electric field is $W = \frac{1}{2}\epsilon_0 |E|^2 = \frac{1}{8\pi}|E|^2$ in units of energy per volume. So the time derivative of W with respect to time is the change of energy per volume per time

$$\frac{d}{dt} W = \frac{1}{8\pi} \frac{\alpha^2}{\beta^2} F \,, \tag{2.32}$$

This quantity describes the emitted power due to spontaneous emission from the source term S. This relation can be set equal to the spontaneous emission energy rate per

volume

$$n_b \gamma_r \hbar\omega \tag{2.33}$$

where n_b is the density of atoms in the core-excited state, γ_r is the Einstein A coefficient for spontaneous emission (inverse of the radiative lifetime), $\hbar\omega$ is the photon energy of the emitted photon. Setting that equal to the right side of (2.32) and solving for F yields

$$F = \frac{2 n_b \gamma_r \hbar \beta^2}{\pi\omega} \tag{2.34}$$

With this normalization constant and the correlation function 2.24 the source term is completely determined. In the numerical simulations the values for S are drawn from a Gaussian distribution $\mathcal{N}(0, \sqrt{F})$ with mean zero and standard deviation $\sqrt{F}$.

2.4.3. Generation of self-amplified spontaneous emission pulses

The following section introduces the approach used to generate the self-amplified spontaneous emission (SASE) pulses generated from XFELs. The XFEL SASE radiation can be approximated as a noise like radiation source with Gaussian random statistics [35, 36, 119]. In the SASE operation mode the x-ray radiation is generated from shot noise in the electron beam that is then amplified in the undulator stage [120], see section 1.1. This initial shot noise in the electron beam can be modeled by a Gaussian random process. In the linear gain regime the amplification does not alter the noise characteristics and the XFEL SASE pulses obey Gaussian statistics [36]. In the deep non-linear gain regime this assumption is not strictly valid anymore. However recent measurements at FLASH in Hamburg demonstrated that to a good approximation FELs can be considered as a Gaussian random process [119].

The SASE pulses can be characterized by the distribution of the ensemble averaged pulse parameters. The SASE pulses show large shot-to-shot fluctuations due to their stochastic nature. Figures 2.6 a), b) depict a single SASE pulse with 7 eV bandwidth and 40 fs pulse duration. The SASE pulse shows a spiky structure in the time and frequency domain. The shape of the SASE pulses is determined by the average spectrum and the average pulse duration T. All other pulse parameters can be derived from these two parameters. An important property of the SASE pulses is the temporal

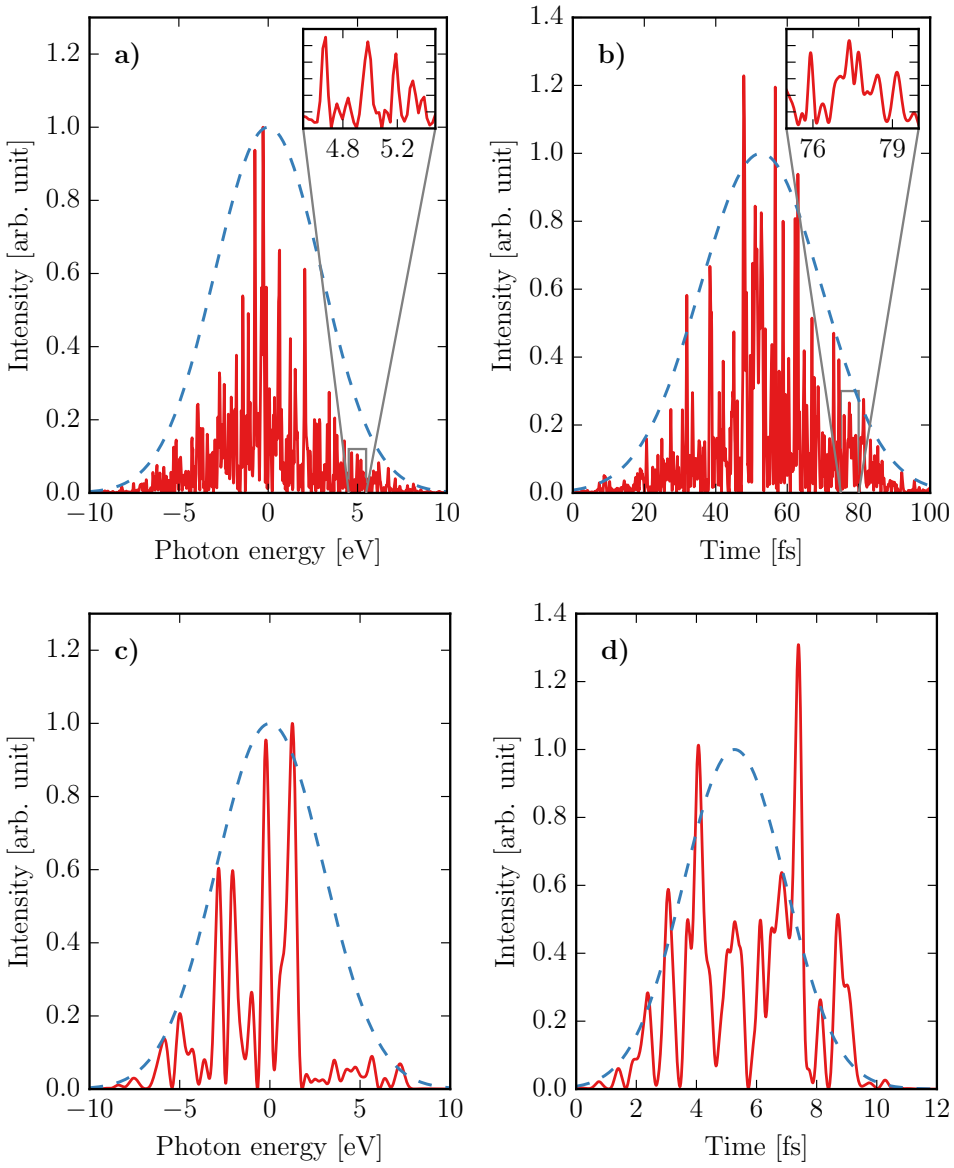

Figure 2.6.: Comparison of two simulated SASE pulses with 7 eV spectral bandwidth and a pulse duration of 40 fs for the pulse on the top and 4 fs for the one at the bottom. a), c) show the two SASE pulses in the frequency domain and b), d) in the time domain. The blue dotted curves mark the average envelope of the SASE pulses in the spectral and time domain respectively.

coherence. The temporal coherence time T_{coh} describes the average duration of a SASE spike in the time domain. A spike is a short intensity peak over which the phase of the electric field is constant. The temporal coherence is inverse proportional to the spectral bandwidth

$$T_{coh} = \frac{\sqrt{\pi}}{\Delta\omega}\,. \tag{2.35}$$

Due to the large bandwidth of SASE XFELs $\frac{\Delta\omega}{\omega} \approx 1\%$ the temporal coherence time is very low. For a typical bandwidth in the soft x-ray regime of $\Delta\omega = 7$eV this corresponds to a coherence time of only 0.17 fs.

Similarly the spectral coherence ω_{coh} describes the average width of a SASE spike in the frequency domain. The spectral coherence is inversely proportional to the pulse duration [35, 121]

$$\omega_{coh} = \frac{1}{T}\,. \tag{2.36}$$

The effect of the pulse duration can be seen in fig. 2.6, which compares two SASE pulses with different pulse duration. The long pulse in fig. 2.6a) clearly consists of many narrow spectral spikes compared to the short pulse in fig. 2.6c). The duration of the intensity spikes in the time domain in fig. 2.6 though is the same for both pulses since they have the same spectral bandwidth. For a typical SASE pulse duration of 40 fs this corresponds to a spectral coherence of 0.1 eV. In section 4.4 it will be shown that the spectral coherence determines plays an important role in Raman scattering with incoherent SASE radiation.

The SASE pulses are generated as chaotic radiation according to the scheme outlined in [122, 20]. The SASE pulses are generated in the frequency domain by the complex Fourier coefficients A_k, which determine the spectral shape. With the help of the inverse Fourier transform the coefficients A_k are transformed into the time domain and multiplied with the temporal envelope $\mathcal{E}_{\text{envelope}}(t)$ to produce the final electric field.

$$E_{SASE}(t) = \mathcal{E}_{\text{envelope}}(t) \sum_k A_k \mathrm{e}^{i\omega t} \tag{2.37}$$

The Fourier coefficients are determined from the underlying power spectrum $\sigma^2(\omega_k)$ of the radiation. The power spectrum for the radiation can be any symmetric function and

common choices are Lorentzian and Gaussian functions. To model the SASE radiation a Gaussian power spectrum was chosen. The complex coefficients A_k are generated by multiplying the square root of the desired power spectrum by two independent Gaussian random numbers X, Y with mean zero and standard deviation one.

$$A_k = (X + iY)\sigma(\omega_k) \qquad X, Y \sim \mathcal{N}(0, 1) \tag{2.38}$$

Gaussian random numbers are chosen to model the Gaussian statistics of the initial shot noise in the SASE pulses. After the inverse Fourier transform the pulse is multiplied with a temporal envelope to obtain the desired temporal pulse shape. In the following a Gaussian temporal envelope was chosen, but depending of the specific parameters of the FEL facility and machine dependent behavior other pulse shapes are also possible. Other pulse shapes include flat rectangular profiles and horn shaped profiles that have the maximum intensity at the beginning and the end of the pulse.

Chapter 3

Photoionization pumped inner-shell atomic x-ray laser in neon

This chapter presents an in-depth theoretical study of amplified spontaneous x-ray emission in neon. In the following the XFEL pump pulse is assumed to be far above the neon K edge (870.2 eV) to neglect resonant excitation of the pre-edge resonances. The case of resonant excitation will be treated in chapter 4. The temporal and spectral characteristics of the emitted x-ray radiation differ considerably for the two different types of excitation. When the XFEL is tuned above the K edge it mostly ionizes inner-shell electrons and generates short-lived core-excited states. The interaction of x-ray radiation with matter is strongest for the inner-shell electrons and the interaction gets weaker for the more outer electron shells. This is in contrast to optical radiation that mainly interacts with valence electrons. Due to the strong interaction of x-rays with inner-shell electrons, a sizable population inversion between inner-shell electrons and outer valence electrons can be generated by photo-ionization with a powerful x-ray pump pulse. This transient population inversion decays quickly due to the short lifetime of the core-excited state. The core-excited states decay mostly via Auger decay where another electron is ejected from the ion. The core-excited ion also has a low probability of 1.5% to undergo a fluorescence decay where a spontaneous photon is emitted in a random direction with a random phase and polarization. If a spontaneous photon is emitted in forward direction, see figure 2.2, it can drive an avalanche of stimulated emission processes. This results in an exponential amplification of the initial fluorescence photons and generates a highly directional intense x-ray beam.

Amplified spontaneous x-ray emission has previously been studied in the rate equation approximation [63–65, 75, 123]. Hopf et al. [124, 125] applied a fully quantum

mechanical description for both matter and the electromagnetic field to study amplified spontaneous emission. An advantage of the complete quantum mechanical description is that the process of spontaneous emission is inherently included in the model. The resulting operator equations were solved numerically in the linear gain regime. They also assumed that the population inversion travels with the speed of light and the absorption was not explicitly taken into account.

In this thesis the semi-classical Maxwell-Bloch approach introduced in chapter 2 is used to simulate the amplification of spontaneous emission in neon. In contrast to the rate equation approach the emitted x-ray radiation is treated on the basis of the electric field. This allows to also determine the emission spectrum from the time dependent electric field. The Maxwell-Bloch approach is a non-perturbative approach and allows to study the saturation of stimulated emission at high intensities. In non-linear optics it is common to expand the polarization in a power series of the electric field [126, 127, 76]

$$P(t) = \chi^{(1)}E(t) + \chi^{(2)}E^2(t) + \chi^{(3)}E^3(t)\,, \tag{3.1}$$

where $\chi^{(n)}$ describes the nth-order non-linear susceptibility that contains the response of the medium to the applied electric field. The expansion only converges if the field intensity is not too high and the field is not resonant with the atomic transition. The Maxwell-Bloch approach is widely used to investigate a wide variety of systems, including x-ray lasing in solid targets [109], rotational and vibrational multilevel systems in the UV regime [128], plasma based x-ray amplifiers [129, 130] and the amplification of high-harmic-generation in plasmas within a 3D model [131].

3.1. Model

The level scheme of neon with the necessary levels to model amplified x-ray fluorescence is shown in Fig. 3.1. Initially all atoms are assumed to be in the ground state and can be photo-ionized by the XFEL radiation. In neon the 1s photo-ionization cross section is 10 times bigger than the valence photo-ionization cross section. The inner-shell photo-ionization of neutral neon yields Ne^{1+} with a hole in the 1s shell $|1s\rangle = |1s^1 2s^2 2p^6\rangle$. This core excited state can decay via Auger decay with the rate $\Gamma_{1s} = 1/2.4\,\mathrm{fs}^{-1} \mathrel{\widehat{=}} 0.27\mathrm{eV}$ to produce Ne^{2+}. The decay is only treated as a loss channel for the core excited state and the Ne^{2+} is not explicitly considered as it is not relevant

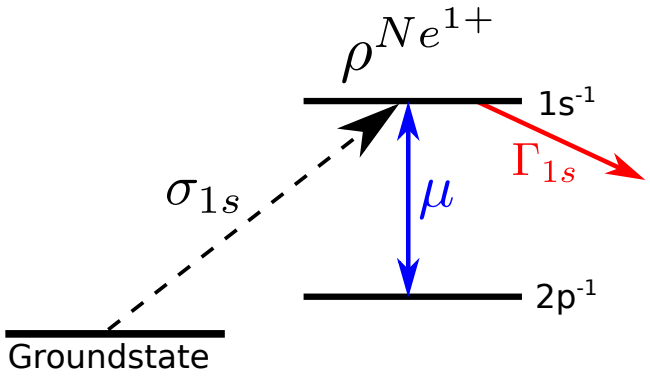

Figure 3.1.: Relevant transitions and couplings in neon for modeling amplified K-α fluorescence.

for the lasing process. Alternatively the core-excited state can decay by emitting a spontaneous photon and relax to the ionic ground state with a hole in the 2p shell $|2p\rangle = |1s^2 2s^2 2p^5\rangle$. The $|1s\rangle$ and the $|2p\rangle$ state are coupled by the electronic dipole moment $\mu = \langle 1s|\hat{z}\,|2p\rangle = 6.8 \times 10^{-2}$ a.u.

The pumping radiation is modeled as a time-dependent photon flux. The XFEL pump pulse gets strongly attenuated when propagating through the neon gas medium and the pump flux J_p evolves according to

$$\frac{\partial J_p(\tau, z)}{\partial z} = -\rho_0(\tau, z) n \left(\sigma_{1s} + \sigma_v\right) J_p(\tau, z)\,, \tag{3.2}$$

where n is the particle density of neon atoms, ρ_0 is the ground-state occupation and $\sigma_{1s} = 1.06 \times 10^{-2}$ a.u. and $\sigma_v = \sigma_{2s} + \sigma_{2p}$ denote the 1s and valence photo-ionization cross section respectively. The values for the valence ionization cross sections are: $\sigma_{2s} = 5.1 \times 10^{-4}$ a.u. and $\sigma_{2p} = 3 \times 10^{-4}$ a.u.. The values for the cross sections are calculated by an atomic structure code [132] at a photon energy of 880 eV. The cross sections as a function of photon energy are depicted in Figure 2.3. The model of the pump pulse evolution does not include absorption from higher charge states of neon and thus underestimates the pump pulse absorption.

The atomic system is described by the density matrix and the formalism was introduced in section 2.2. To derive the time evolution of the density matrix, the wave function of the atomic system is expanded in the groundstate $|\phi_0\rangle$ and single-particle

hole excitation $|\phi_i^a\rangle$. In the interaction picture the expansion is given by

$$|\Psi, t\rangle_I = \alpha_0(t)\,|\phi_0\rangle + \sum_{i,a} \alpha_i^a(t)\,|\phi_i^a\rangle\,, \tag{3.3}$$

To determine the time evolution of the atomic system the expansion coefficients $\alpha_0(t)$ and $\alpha_i^a(t)$ have to be determined. The time-dependent Schrödinger equation determines the evolution of the wavefunction

$$i\frac{\partial}{\partial t}\,|\Psi, t\rangle_I = \hat{H}_I\,|\Psi, t\rangle_I \tag{3.4}$$

where H_I is the time-dependent perturbation in the interaction picture. The interaction Hamiltonian H_{int} in the dipole approximation in the Schrödinger picture is given by

$$\hat{H}_{\text{int}} = -\hat{z}\,E(t)\,. \tag{3.5}$$

In the dipole approximation the x-ray field is assumed to be constant over the size of the atom. This approximation requires that the wavelength of the radiation is large compared to the size of the atom. For photon energies below 1 keV (1 keV photon energy corresponds to a wavelength of 1.2 nm, which is much larger than the size of the neon atom which is 38 pm) this requirement is fulfilled. The Hamiltonian $\hat{H_{\text{int}}}$ is transformed to the interaction picture by the transformation

$$\hat{H}_I = \mathrm{e}^{i\hat{H}_0 t}\,\hat{H}_{\text{int}}\,\mathrm{e}^{-i\hat{H}_0 t} \tag{3.6}$$

Inserting the expansion of the wavefunction into the Schrödinger equation one obtains the following equations for the expansion coefficients

$$\dot{\alpha}_0 = -i\sum_{i,a} \alpha_i^a \langle\phi_0|\hat{H}_I\,|\phi_i^a\rangle \tag{3.7}$$

$$\dot{\alpha}_i^a = -\,i\alpha_0\langle\phi_i^a|\hat{H}_I\,|\phi_0\rangle - i\alpha_j^a\langle\phi_i^a|\hat{H}_I\,|\phi_j^a\rangle \tag{3.8}$$

Replacing the electric field in the interaction Hamiltonian with its expansion into a

slowly varying envelope $\mathcal{E}(t)$ from equation 2.12 yields for the groundstate coefficient

$$\dot{\alpha}_0 = \frac{i}{2}(\mathcal{E}(t)\,\mathrm{e}^{-i\omega t} + \mathcal{E}^\star(t)\,\mathrm{e}^{i\omega t}) \sum_{i,a} \alpha_i^a \langle\phi_0\,|\hat{z}\,|\phi_i^a\rangle \mathrm{e}^{-i\omega_{ai}} \tag{3.9}$$

where $\omega_{ai} = \omega_a - \omega_i$. In case the frequency ω of the electric field is close to the transition frequency ω_{ai}, the rotating wave approximation can be applied. This means that the term with $\mathcal{E}^\star$ and the exponent $i(\omega - \omega_{ai})t$ is kept while the other term with $\mathcal{E}$ and the fast oscillating exponent $-i(\omega + \omega_{ai})t$ is neglected. The same reasoning can be applied for the equation of the expansion coefficient α_i^a. The time evolution of the expansion coefficients in the rotating wave approximation is determined by

$$\dot{\alpha}_0 = \frac{i}{2}\mathcal{E}^\star(t) \sum_{i,a} \alpha_i^a \langle\phi_0\,|\hat{z}\,|\phi_i^a\rangle\, \mathrm{e}^{i(\omega-\omega_{ai})t} \tag{3.10}$$

$$\begin{aligned}\dot{\alpha}_{1s}^a &= \frac{i}{2}\alpha_0\,\langle\phi_{1s}^a\,|\hat{z}\,|\phi_0\rangle\,\mathcal{E}(t)\,\mathrm{e}^{i(\omega_{a1s}-\omega)t} \\ &+ \frac{i}{2}\alpha_{2p}^a\langle\phi_{1s}^a\,|\hat{z}\,|\phi_{2p}^a\rangle\,\mathcal{E}(t)\,\mathrm{e}^{i(\omega_{2p1s}-\omega)t} - \frac{\Gamma_{1s}}{2}\alpha_{1s}^a\end{aligned} \tag{3.11}$$

$$\dot{\alpha}_{2p}^a = \frac{i}{2}\alpha_0\langle\phi_{2p}^a\,|\hat{z}\,|\phi_0\rangle\,\mathcal{E}(t)\,\mathrm{e}^{i(\omega_{a2p}-\omega)t} + \frac{i}{2}\alpha_{1s}^a\langle\phi_{2p}^a\,|\hat{z}\,|\phi_{1s}^a\rangle\,\mathcal{E}^\star(t)\,\mathrm{e}^{i(\omega-\omega_{2p1s})t} \tag{3.12}$$

The coupling matrix elements $\langle\phi_0\,|\hat{z}\,|\phi_i^a\rangle$ and $\langle\phi_{1s}^a\,|\hat{z}\,|\phi_{2p}^a\rangle$ can be expressed in terms of one-particle dipole matrix elements [133]

$$\langle\phi_0\,|\hat{z}\,|\phi_i^a\rangle = \sqrt{2}\,z_{ia} \tag{3.13}$$

$$\langle\phi_{1s}^a\,|\hat{z}\,|\phi_{2p}^a\rangle = z_{2p1s} \tag{3.14}$$

where $z_{pq} = \langle\varphi_q\,|\hat{z}\,|\varphi_p\rangle$ is the dipole matrix matrix element between one-particle orbitals with $\hat{H}_0\,|\varphi_p\rangle = \epsilon_p\,|\varphi_p\rangle$.

With the help of the expansion coefficients it is now possible to determine the reduced ionic density matrix for the singly charged neon ion from equation 2.5

$$\rho_{j,k}(t) = \sum_{c\,\in\,cont.} \alpha_j^c(t)\,\alpha_k^{c\star}(t) \tag{3.15}$$

where the sum is over the state c of the ejected photo-electron as it is not observed and its degrees of freedom can be removed by tracing over the photo-electron states. The reduced ionic density matrix elements describe the occupation of the core-excited

intermediate state ρ_{1s1s}, the occupation of the ionic ground state ρ_{2p2p} and the coherence between the two states ρ_{2p1s}.

$$\begin{aligned}
\frac{\partial \rho_{1s1s}(\tau, z)}{\partial \tau} &= -\Gamma_{1s}\rho_{1s1s} + \sigma_{1s} J_p \rho_0 - \mu \,\mathrm{Im}(\mathcal{E}\rho_{2p1s}) \\
\frac{\partial \rho_{2p2p}(\tau, z)}{\partial \tau} &= \sigma_{2p} J_p \rho_0 + \mu \,\mathrm{Im}(\mathcal{E}\rho_{2p1s}) \\
\frac{\partial \rho_{2p1s}(\tau, z)}{\partial \tau} &= -\frac{\Gamma_{1s}}{2}\rho_{2p1s} + i(\rho_{1s1s} - \rho_{2p2p})\frac{\mu \mathcal{E}^\star}{2} + S\,.
\end{aligned} \tag{3.16}$$

Here S is a phenomenological random source term to model spontaneous emission that acts as a seed for the amplification process. The term is necessary since the electric field is treated classically and therefore does not include spontaneous emission. The source term was derived in section 2.4.2. The groundstate population is determined by

$$\frac{\partial \rho_0(\tau, z)}{\partial \tau} = -(\sigma_{1s} + \sigma_v) J_p(\tau, z)\rho_0(\tau, z)\,. \tag{3.17}$$

The emitted x-ray radiation is treated as a complex electric field and its envelope evolves according to eq. 2.15. The electric field and the atomic system are coupled via the polarization

$$\mathcal{P} = 2n\mu\rho_{1s2p}\,. \tag{3.18}$$

The ionic density matrix ρ along with the XFEL pump radiation J_p and the emitted x-ray radiation are solved self-consistently and propagated through space to describe the amplification of spontaneous emission. The atomic system is solved by the split step method described in section 2.4.1 with integration steps $\Delta t = 0.01\,\mathrm{fs}$ and $\Delta z = c\,\Delta t$ for all numerical simulations in this thesis. In the moving frame the evolution of the pulses is determined by a differential equation with only a first order spatial derivative. In a stationary frame on the other hand, the pulses are propagating at the speed of light and the evolution is determined by 2.14, which includes a spatial and a temporal derivative. This couples space and time together and introduces a stability condition for the space and time step for the numerical propagation. This stability condition is called Courant–Friedrichs–Lewy (CFL) condition and implies that $\frac{c\Delta t}{\Delta z} < 1$ to ensure stability of the numerical solution.

3.1.1. Gain

Stimulated emission transfers energy from the medium to the radiation, resulting in an exponential amplification of the radiation. The increase in radiation power when passing through the medium is called gain. The gain $g(z,t)$ is defined as the spatial derivative of the logarithm of the intensity

$$g(z,t) = \frac{d}{dz} \ln\left(|\mathcal{E}(z,t)|^2\right) = \frac{d|\mathcal{E}(z,t)|^2/dz}{|\mathcal{E}(z,t)|^2} \,. \tag{3.19}$$

Using equation 2.15 to calculate the derivative yields

$$\frac{\partial|\mathcal{E}(z,t)|^2}{\partial z} = i\frac{2\pi\omega}{c}\mathcal{E}^{\star}(z,t)\mathcal{P}(z,t) + c.c \tag{3.20}$$

Inserting the polarization $\mathcal{P}$ from eq. 3.18 together with the formal integration of the coherence in eq. 3.16, one obtains the following equation for the gain

$$g(z,t) = 2\,\mathrm{Re}\left\{\frac{2\pi n\mu^2\omega}{c}\frac{1}{\mathcal{E}(z,t)}\int_0^t \mathrm{e}^{-\frac{\Gamma_{1s}}{2}(t-t')}\mathcal{E}(z,t')\left(\rho_{1s1s}(z,t') - \rho_{2p2p}(z,t')\right)dt'\right\} . \tag{3.21}$$

The gain is proportional to the population inversion between the upper and the lower lasing state $\rho_{1s1s} - \rho_{2p2p}$. If this population inversion is positive, the gain is also positive and the radiation gets amplified by stimulated emission. If the population inversion is negative on the other hand, the gain is also negative and the radiation gets absorbed. In the so called linear gain region the gain $g(z)$ is constant and does not change with propagation through the medium. From equation 3.19 follows that a constant gain leads to an exponential amplification of the emitted x-ray intensity.

3.2. Gaussian pump pulse

In this section the atomic x-ray laser is pumped with a coherent and transform limited x-ray source. Stable and temporally coherent x-ray radiation can be generated by seeded XFEL sources [44–46] and so called self-seeded XFELs [47, 48, 134]. For the XFEL pump pulse the following parameters were assumed: 2 $\times 10^{12}$ photons per pulse, 40 fs pulse duration (FWHM of the intensity) and 7 eV spectral bandwidth (FWHM).

The focal radius of the XFEL pulse is assumed to be constant over the propagation distance with a value of 2 µm. The gas density for the neon medium is 1.6 $\times 10^{19}\,\mathrm{cm}^{-3}$. The gas cell with the amplification medium has a total length of 15 mm. These pulse parameters are typical parameters for current XFEL sources and correspond to the pulse parameters from recent experiments [75].

3.2.1. Amplified stimulated emission

Fig. 3.2a) displays how the amplified stimulated emission and the XFEL pump pulse evolve with propagation through the gas medium. It shows the number of photons in the XFEL pump pulse and the emitted x-ray radiation as a function of propagation distance. The atomic x-ray laser (XRL) starts from initial spontaneous emission which then gets amplified by stimulated emission by several orders of magnitude.

Fig. 3.3a) displays the time evolution of the population for the upper and lower lasing state along with the XRL intensity in the linear gain regime. The XFEL pump pulse is centered around 50 fs and it is populating the upper lasing state ρ_{1s1s} via 1s photo-ionization. The ρ_{1s1s} population reaches its maximum of 7% at 50 fs and the core-excited state population then quickly decays via Auger decay. The population of the final lasing state ρ_{2p2p} is almost zero due to the small photo-ionization cross section for 2p electrons (see fig. 2.3) and the low intensity of the emitted x-ray radiation. In the stimulated emission process the population of the excited state in transferred to the lower state and the radiation is amplified. In the linear gain regime the population transfer to the lower lasing state by stimulated emission is insignificant. The small population of the final state keeps the population inversion ρ_{1s1s} - ρ_{2p2p} independent of the emitted x-ray intensity and ensures a constant gain.

The linear gain region for the amplified stimulated emission extends to around 5 mm of propagation distance in Fig. 3.2a). At this propagation distance the amplification by stimulated emission is no longer exponential and the slope of the curve is flattening out. The strong reduction of the gain at this propagation distance can have two different reasons. The first possibility is that the pump pulse is not intense enough anymore to induce a population inversion in the medium. The pump pulse is getting absorbed when propagating through the medium and its intensity decreases. The other possible reason is that the gain is saturated and further amplification is strongly reduced.

In saturation the emitted x-ray intensity effectively populates the final lasing state by

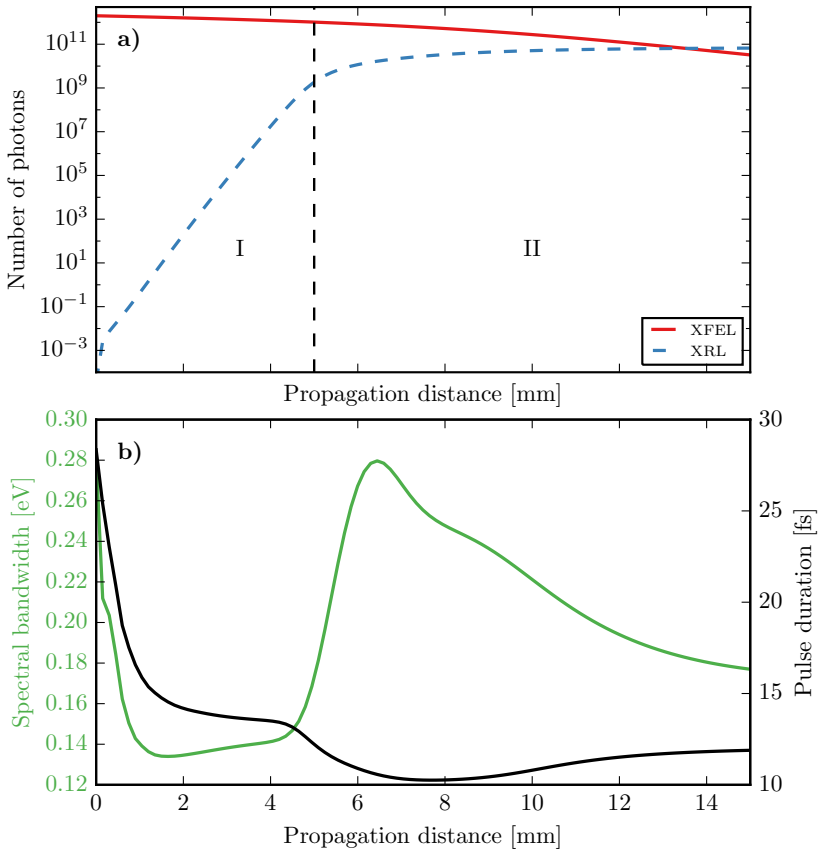

Figure 3.2.: Evolution of the amplified spontaneous x-ray emission in neon for a Gaussian XFEL pump pulse. a) shows the number of photons in the XFEL pump pulse (red line) and the emitted XRL pulse (blue dotted line). The black dotted line separates the linear gain regime from the saturated gain regime. b) depicts the development of the spectral bandwidth (FWHM, green line) and the pulse duration (FWHM, black line) as a function of propagation distance along the gas cell.

stimulated emission and the population inversion is reduced and can even be inverted. Fig. 3.3b) show the populations at the onset of saturation at a propagation distance of 5 mm. Here the emitted x-ray intensity strongly drives down the population from the upper to the lower state. There is a small bend in the upper state population and the depopulation by stimulated emission is faster than the Auger decay. The population of the lower lasing level even exceeds the upper state population at 72 femtoseconds. This means the population inversion is negative and the radiation is no longer amplified by stimulated emission but rather gets absorbed.

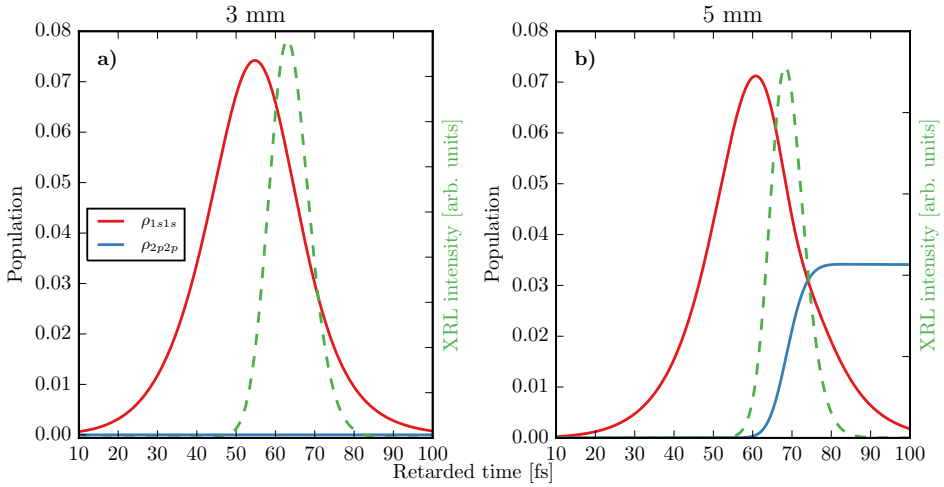

Figure 3.3.: Level populations and XRL intensity as a function of retarded time after 3 mm of propagation a) and 5 mm of propagation b).

When an atomic transition is driven by a strong resonant field, Rabi flopping occurs. Rabi flopping is a coherent oscillation of the population between the two levels. In a two level system without damping and a resonant field, the populations $C_{1s}(t)$ and $C_{2p}(t)$ in the rotating wave approximation evolve according to [135]

$$\dot{C}_{1s}(t) = \frac{i}{2}\mathcal{R}C_{2p}(t) \tag{3.22}$$

$$\dot{C}_{2p}(t) = \frac{i}{2}\mathcal{R}^{\star}C_{1s}(t)\,, \tag{3.23}$$

where $\mathcal{R} = \mu\mathcal{E}$ is the Rabi frequency. Solving these coupled equations with the initial conditions $C_{1s}(0) = 1$ and $C_{2p}(0) = 0$ for a completely inverted medium yields

$$C_{1s}(t) = (1 + \cos(|\mathcal{R}|t))/2 \tag{3.24}$$

$$C_{2p}(t) = (1 - \cos(|\mathcal{R}|t))/2 \tag{3.25}$$

$$\tag{3.26}$$

This solution shows that the population is oscillating between the two levels with the Rabi frequency $|\mathcal{R}|$. Fig. 3.4 depicts the gain as a function of propagation distance along with the maximum Rabi frequency $\mathcal{R}_{max} = \arg\max_t \mathcal{R}(t)$. In the beginning of

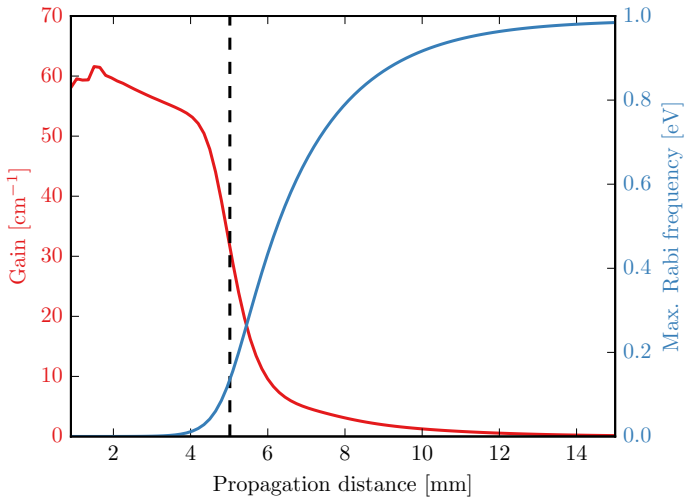

Figure 3.4.: Gain and maximum Rabi frequency as a function of propagation distance. Black dotted line at 5 mm propagation distance marks the saturation of the gain where the maximum Rabi frequency $\mathcal{R}_{max}$ reaches $\frac{1}{2}\Gamma_{1s}$.

the medium the gain is fairly constant and only decreases slightly with propagation. At around 4 mm of propagation distance the gain starts to drop quickly and reaches half its initial value at 5 mm propagation distance (black dotted line). Equations 3.24 shows that the population transfer from one state to the other state takes half a Rabi cycle $|\mathcal{R}|$. The gain saturation therefore occurs when the maximum Rabi frequency (shown in fig. 3.4) is equal to half the Auger lifetime of the upper state

$$\mathcal{R}_{max} = \frac{1}{2}\Gamma_{1s} \tag{3.27}$$

This means that the depopulation of the upper state by the resonant field is equal to the Auger decay rate of the upper state. An increase of the Rabi frequency results in an accelerated decay of the population inversion that further decreases the gain. This shows that the gain is indeed saturated and the decrease in gain is not a result of pump-pulse absorption.

In the saturated gain region the gain is strongly reduced and the XRL pulse reaches 6.6 $\times 10^{10}$ photons after 15 mm of propagation in fig. 3.2a). The number of spontaneous photons in forward direction into the solid angle Ω (see Fig. 2.2), can be estimated by assuming that every atom in the interaction volume gets ionized and emits a spontaneous

photon with the probability $\frac{\Gamma_{1s}}{\gamma_r}$. This estimate yields 2×10^3 spontaneously emitted photons and results in an amplification by stimulated emission by a factor of 3×10^7.

Fig. 3.2b) depicts the spectral bandwidth and the pulse duration as a function of propagation distance. The XRL pulse has an initial bandwidth of 0.27 eV, corresponding to the natural lifetime of the core-excited state. As the amplification sets in, the spectral bandwidth quickly drops to around 0.14 eV. For most of the exponential amplification region (linear gain regime) the spectral bandwidth then stays almost constant. The pulse duration shows a similar behavior in the linear gain regime. The initial XRL pulse duration is around 30 fs, which corresponds to the duration of the population inversion in the beginning of the medium. The initial emitted x-ray pulse is not transform limited, because it is seeded from incoherent spontaneous emission. With propagation and amplification the XRL pulse duration quickly decreases and stays almost constant at the transform-limited pulse duration. In saturation the accelerated decay of the upper state population results in a broadening of the spectral bandwidth and a further decrease of the pulse duration. The amplification behavior of the transient x-ray laser is quite different from the usual spectral gain narrowing in amplified spontaneous emission lasers [136, 137]. For the transient x-ray laser gain narrowing is only observed in the initial amplification stage, followed by a long amplification period with nearly constant spectral bandwidth and pulse duration.

The evolution of the normalized XRL spectrum with propagation through the medium along with spectra at three different points in the medium are shown in Fig. 3.5. The spectra are averaged over 200 runs with different initial seeds for the random number generator. This averaging is especially important for the spectra in the beginning of the medium, where the spectrum is determined by the characteristics of spontaneous emission. The exponential decay of the core-excited state in spontaneous emission results in a Lorentzian line shape. This line shape is reproduced with the Maxwell-Bloch model and shows that the random source term is a good description of spontaneous emission in this semi-classical framework. With propagation and amplification the spectrum becomes narrower and loses the Lorentzian tails. When saturation sets in the spectrum quickly broadens and reaches its maximum bandwidth.

Fig. 3.6a) illustrates how the temporal pulse shape evolves with propagation. In the linear gain region, at 3 mm propagation distance, the pulse displays an asymmetric pulse shape with a width of 15 fs. The asymmetry comes from the fact that the left

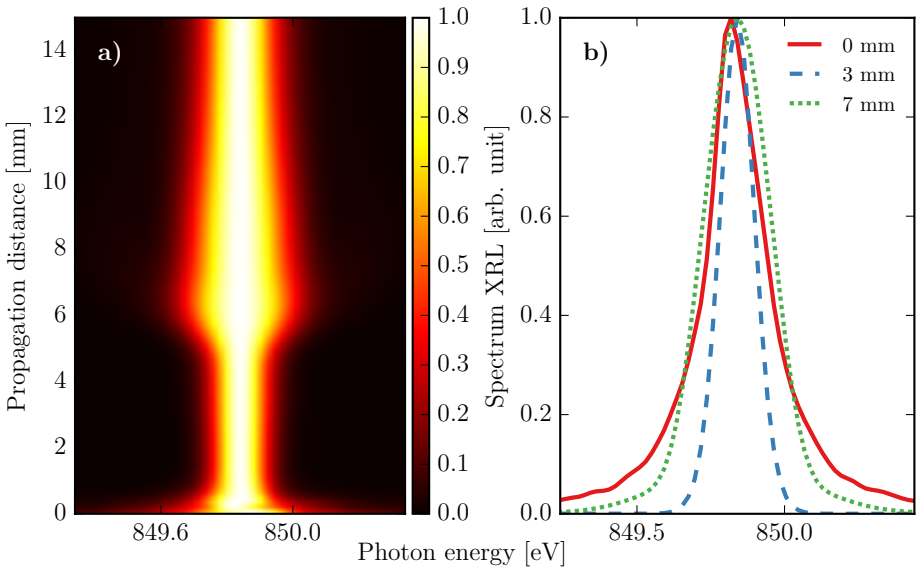

Figure 3.5.: a) Evolution of the normalized XRL spectra as a function of propagation distance. b) Normalized XRL spectra at three different points in the medium with a bandwidth (FWHM) of 0.27 eV, 0.14 eV and 0.28 eV respectively.

edge of the pulse is determined by the rise of the core-excited state population by photo-ionization, whereas the right edge is determined by the Auger decay of the upper state. The pulse duration of the XRL pulse has its minimum in the saturated gain regime after 7 mm of propagation. The populations for the upper and lower lasing state show coherent oscillations with a single Rabi cycle at a propagation distance of 7 mm in Fig. 3.6b). The maximum Rabi frequency is 0.53 eV, corresponding to an oscillation period of 7.8 femtoseconds. The Rabi flopping leads to a second subsequent peak in the population inversion, which yields a positive gain and generates a second peak in the XRL temporal pulse. This smaller second peak can be seen in Fig. 3.6a) at 15 mm of propagation.

3.2.2. Absorption of the pump pulse

Figure 3.2a) illustrates the evolution of the XFEL pump pulse as it is propagating through the gas medium. The XFEL pump pulse is getting absorbed in the neon medium and its evolution is determined by equation 3.2. For a weak x-ray flux, where the groundstate population is varying very little, the solution of equation 3.2 describes

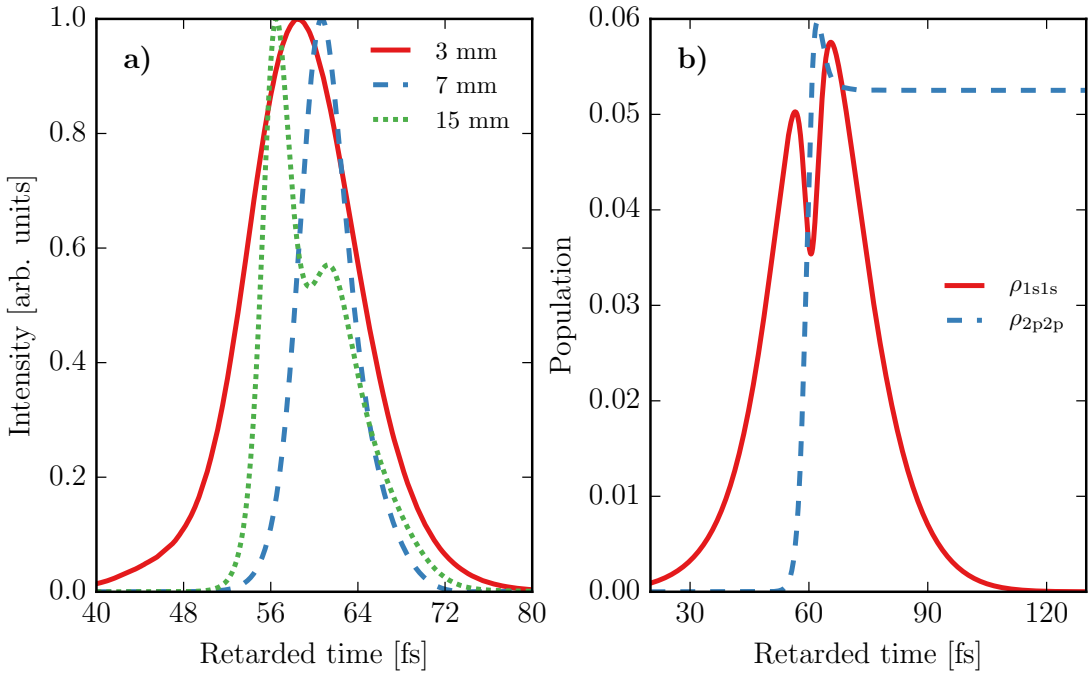

Figure 3.6.: a) Normalized XRL temporal pulse profiles at three different points in the medium. b) Populations for the core-excited state ρ_{1s1s} and the final state ρ_{2p2p} after 7 mm of propagation.

an exponential decrease of the pump flux J_p

$$J_p(z) = J_p(0)\,\mathrm{e}^{-(\sigma_{1s}+\sigma_v)\,n\,z}\,. \tag{3.28}$$

This relationship for the attenuation of the x-ray flux is called Lambert–Beer law. Figure 3.2a) however illustrates that the attenuation of the XFEL pump is not exponential and the Lambert–Beer law is not valid for this high-intensity x-ray flux.

Figure 3.7 shows the population of the groundstate in neutral neon along with the XFEL pump intensity. In the beginning of the medium the XFEL pump intensity is so high that every single neon atom already gets ionized by the leading edge of the pump pulse. This strong depopulation of the ground states leads to absorption bleaching [138–141]. This means that the gas medium becomes transparent for the remaining x-ray radiation if all the atoms have already been ionized. The effect of absorption bleaching leads to a reduced attenuation of the XFEL pump pulse. With propagation the intensity of the XFEL pump pulse decreases and towards the end of the medium its

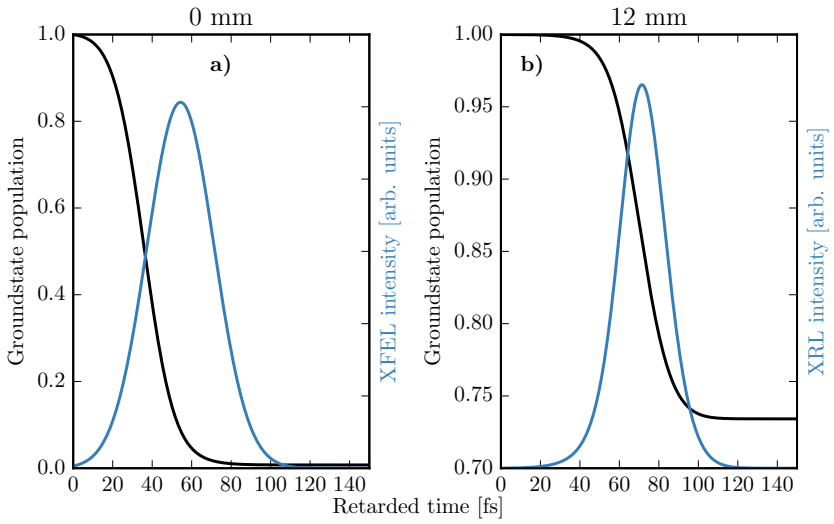

Figure 3.7.: Groundstate population of neutral neon (black line) and intensity of the XFEL pump pulse (blue line) in the beginning of the medium a) and after 12 mm of propagation b).

intensity is not sufficient anymore to induce absorption bleaching. Figure 3.7b) shows that at 12 mm of propagation distance the groundstate population remains at 75 % after the interaction with the XFEL pump pulse. The total transmission of the pump pulse after passing through the gas medium amounts to 2%. Figure 3.8 illustrates that absorption bleaching becomes quite significant at high intensities. The figure shows the transmission of the XFEL pulse after propagating through the gas medium for different incoming pulse energies. Although the incoming pulse energy only varies by a factor of five, the transmission changes by more than two orders of magnitude. The absorption bleaching makes the transmission highly non-linear and strongly dependent on the incoming pulse energy.

3.2.3. Gain guiding

This section studies the amplification process in more detail and investigates the influence of the pump pulse absorption on the atomic x-ray laser. Fig. 3.9 depicts the normalized XRL temporal pulse shape, the population inversion and the temporal shape of the XFEL pump pulse as a function of propagation distance. The propagation of the XFEL pump pulse through the optically dense medium, shown in Fig. 3.9c),

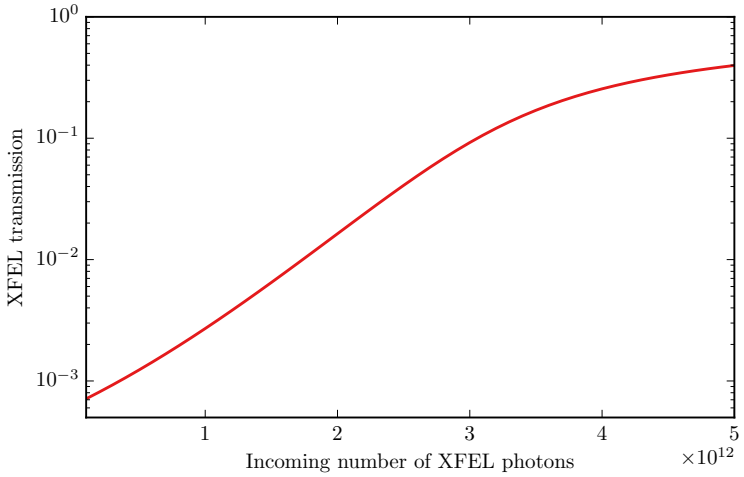

Figure 3.8.: Transmission of the XFEL pulse through the gas medium as a function of the incoming pulse energy.

results in two important effects for a transient gain x-ray amplifier: Due to bleaching and strong absorption the temporal shape of the XFEL pump pulse changes with propagation. The leading edge of the pump pulse is more strongly attenuated due to the ground-state bleaching. This leads to a steepening of the leading edge in the pump pulse and more importantly the pulse maximum is shifted towards later times in the frame of the propagating pulse. This shift in time of the pump pulse is also imprinted in the temporal profile of the population inversion. This means that the peak of the pump pulse and the population inversion travel with a velocity smaller than the speed of light, as can be seen in Fig. 3.9b) and c).

Another important aspect for the evolution of the gain is the group velocity of the emitted XRL radiation. For a pulse propagating on a high-gain resonant transition the group velocity can be significantly smaller than the speed of light [142]. This reduced group velocity can lead to a velocity mismatch (slippage) between the population inversion and the propagating XRL radiation. This slippage results in a drastic reduction of the gain for transient x-ray laser schemes [143, 144]. In the following it will be shown that the absorption of the pump pulse along with the reduced group velocity of the emitted radiation will lead to a gain-guiding effect. The combination of the two effects ensure that the population inversion and the amplified x-ray pulse overlap in time throughout the exponential gain region. In the retarded time frame vertical

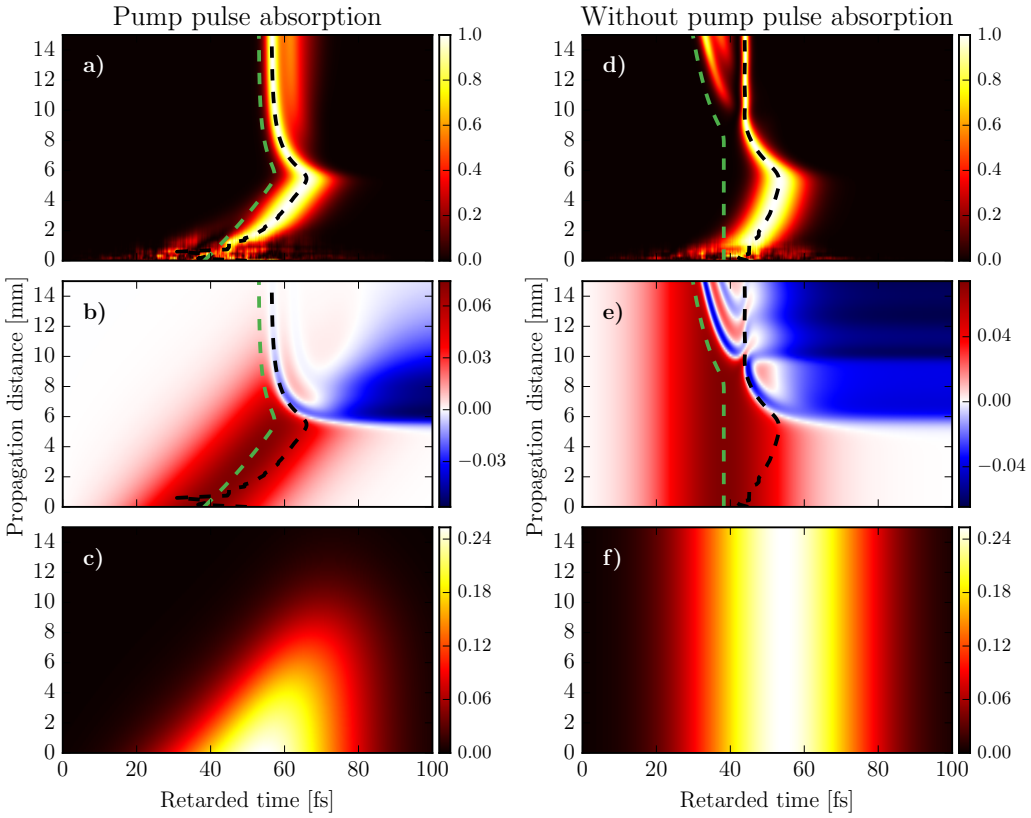

Figure 3.9.: Evolution of the normalized XRL temporal profile in a), d), the population inversion in b), e) and the XFEL pump pulse in c), f) as a function of propagation distance. The figures on the left side include pump pulse absorption, while the ones on the right are without pump pulse absorption. The black dotted lines follow the maximum of the XRL pulse intensity and the green lines follow the maximum of the population inversion. In the retarded frame the XFEL pulse was initially centered at 50 fs.

lines move at the speed of light, while lines moving to the right propagate at a lower velocity. Fig. 3.9a), b) and c) show that the emitted XRL radiation, the population inversion and the XFEL pump pulse propagate with a group velocity of 0.998 times the speed of light. They all show a clear temporal overlap in the exponential gain region for propagation distances smaller than 7 mm. The maximum of the XRL pulse (black dotted line) and the maximum of the population inversion (green dotted line) however do not perfectly overlap. The maximum of the XRL intensity is trailing behind the maximum of the population inversion, because the build up of the macroscopic

polarization from the population inversion takes some time. This delay comes from the integration over the exponential in the equation for the gain (eq. 3.21) and is proportional to Γ_{1s}^{-1}. When the amplification of the XRL is saturating at 5 mm of propagation distance, the gain drops down and the XRL pulse is propagating with the speed of light through the rest of the medium. The maximum of the XRL pulse is shifting slightly to the left due to the absorption from the negative population inversion at later times. In the gain-guiding mechanism the absorption of the pump pulse thus modifies the propagation velocity of the population inversion to nearly match the group velocity of the XRL pulse to obtain a good temporal overlap between the two quantities.

The absorption of the XFEL pump pulse is essential for maintaining a high gain amplification. To emphasize the importance of the gain-guiding mechanism the amplification process without pump pulse absorption is shown in Fig. 3.9 d), e), f). In absence of pump pulse absorption a large temporal delay between population inversion and XRL intensity can be seen in Fig. 3.9 d), e). This large delay leads to a considerable reduction of the gain. The gain before saturation is even less than in the case with pump pulse absorption, despite the larger pump power in the case with no absorption. In saturation the typical temporal and spatial ringing pattern of the saturated pulse propagation are observed. Neglecting the pump pulse absorption basically yields a gain-swept amplifier, where the population inversion is created almost instantaneously and travels with the speed of light. This gain swept x-ray amplifier has been previously studied in [145, 146]. The absence of a gain-guiding mechanism in the gain-swept amplifier together with the fast Auger decay of the core-excited state and the finite amplifier bandwidth lead to a reduced gain.

3.3. Comparison with rate equations

Most of the previous theoretical studies of transient x-ray lasers schemes were based on a rate equation approach [63–65, 75, 123]. In the rate equation approach only the occupations of the lasing levels are modeled and the coherence between the levels is not included. This means that coherent effects like Rabi flopping can not be treated with a rate equation approach. The emitted x-ray radiation is treated as a time-dependent intensity and the amplification is determined by the population inversion and the stimulated emission cross section. Treating the emitted radiation as an intensity

compared to the electric field in the Maxwell-Bloch approach therefore comes with a loss of spectral information. The rate equation approach also does not include effects like the gain-dependent group velocity, which proved to be important for the gain guiding mechanism discussed in section 3.2.3. In the following a comparison between the rate equation approach and the Maxwell-Bloch approach will be made to test the validity of the rate equation approach for a transient gain x-ray amplifier.

The time evolution of the populations in the rate equation approach can be derived from the density matrix equations. To obtain the rate equations for the populations the coherence term on the right hand in equations 3.16 has to be eliminated. The formal solution for the coherence gives

$$\rho_{2p1s} = i\frac{\mu}{2}\int_0^t \mathrm{e}^{-\frac{\Gamma_{1s}}{2}(t-t')}\mathcal{E}^{\star}(z,t')\left(\rho_{1s1s}(z,t') - \rho_{2p2p}(z,t')\right)dt' \,. \tag{3.29}$$

The integration can be carried out by assuming that the decay of the coherence is much faster than variations in the population inversion and the field envelope. This means that the population inversion and the field are approximately constant over the integration period and can be pulled out of the integral. Performing the integration over the remaining exponential yields

$$\rho_{2p1s} = i\frac{\mu}{\Gamma_{1s}}\mathcal{E}^{\star}\left(\rho_{1s1s} - \rho_{2p2p}\right). \tag{3.30}$$

This approximation for the integral works well if there are additional decay processes for the coherence that do not affect the population inversion. An example for such a process are collisions between the atoms that destroy the coherence but do not affect the populations. For the neon gas density considered in this work the collision rate is negligible compared to the Auger lifetime of the core-holes. The decay of the population inversion with rate Γ_{1s} is therefore faster than the decoherence rate $\frac{\Gamma_{1s}}{2}$. This means that the rate equation approach might not be well suited to describe transient lasing schemes with a short lifetime of the population inversion.

Inserting the approximation for the coherence from equation 3.30 into 3.16 to obtain

the time evolution of the populations yields

$$\frac{\partial \rho_{1s1s}}{\partial t} = -\Gamma_{1s}\rho_{1s1s} + \sigma_{1s}J_p\rho_0 - \frac{\mu^2}{\Gamma_{1s}}|\mathcal{E}|^2(\rho_{1s1s} - \rho_{2p2p}) \tag{3.31}$$

$$\frac{\partial \rho_{2p2p}}{\partial t} = \sigma_{2p}J_p\rho_0 + \frac{\mu^2}{\Gamma_{1s}}|\mathcal{E}|^2(\rho_{1s1s} - \rho_{2p2p})\,. \tag{3.32}$$

These are the so called rate equations for the population of the upper lasing state ρ_{1s1s} and the lower lasing state ρ_{2p2p}. The time evolution of the ground state is the same as in the Maxwell-Bloch approach and determined by equation 3.17.

The evolution of the emitted XRL flux in the rate equation approximation can be derived from the wave equation for the electric field envelop in equation 2.14

$$\frac{\partial(\mathcal{E}\mathcal{E}^\star)}{\partial z} + \frac{1}{u}\frac{\partial(\mathcal{E}\mathcal{E}^\star)}{\partial \tau} = \mathcal{E}^\star\left(\frac{\partial \mathcal{E}}{\partial z} + \frac{1}{u}\frac{\partial \mathcal{E}}{\partial \tau}\right) + c.c. \tag{3.33}$$

where u is the propagation velocity of the XRL pulse in the moving frame. The term in the bracket on the right hand side can be substituted with equation 2.14 and yields

$$\frac{\partial|\mathcal{E}|^2}{\partial z} + \frac{1}{u}\frac{\partial|\mathcal{E}|^2}{\partial \tau} = i\frac{2\pi\omega}{c}\mathcal{E}^\star\mathcal{P} + c.c. \tag{3.34}$$

where the polarization is defined by equation 3.18. Substituting the coherence in the polarization with the coherence in the rate equation approximation from equation 3.30 results in

$$\frac{\partial|\mathcal{E}|^2}{\partial z} + \frac{1}{u}\frac{\partial|\mathcal{E}|^2}{\partial \tau} = \frac{8\pi\omega\mu^2 n}{c\Gamma_{1s}}(\rho_{1s1s} - \rho_{2p2p})|\mathcal{E}|^2 \tag{3.35}$$

The evolution of the XRL photon flux $J = \frac{c}{8\pi\omega}|\mathcal{E}|^2$ is thus determined by

$$\frac{\partial J}{\partial z} + \frac{1}{u}\frac{\partial J}{\partial \tau} = gJ + \rho_{1s1s}A_{1s\to 2p}\,n\,\frac{\Omega}{4\pi} \tag{3.36}$$

where the last term on the right was added to include the flux due to spontaneous emission. $A_{1s\to 2p} = \frac{4}{3}\frac{\omega^3}{c^3}\mu^2 = \frac{1}{\tau_{sp}}$ is the Einstein coefficient for spontaneous emission and is equal to the inverse of the spontaneous emission lifetime τ_{sp}, n is the particle density and Ω (see Fig. 2.2) is the solid angle in forward direction in which the emission can be stimulated. The gain g that determines the amplification by stimulated emission

is defined by

$$g = \frac{8\pi\omega\mu^2 n}{c\Gamma_{1s}}(\rho_{1s1s} - \rho_{2p2p}) \tag{3.37}$$

In the comoving frame of the pulse with $\tau = t - \frac{z}{c}$ the propagation velocity u of the pulse is given by $\frac{1}{u} = \frac{1}{v_g} - \frac{1}{c}$, where v_g is the group velocity of the pulse. In most rate equation approaches [75, 65] the group velocity v_g is taken to be constant and equal to the speed of light c. This means the time derivative vanishes like in equation 2.15. Equation 3.36 however allows for an ad-hoc improvement to explicitly introduce the gain dependent group velocity for the emitted XRL radiation [123]. The gain dependent group velocity can be estimated by [142]

$$v_g = \frac{c}{(1 + c\, g(z,t)/\Gamma_{1s})^{-1}} \tag{3.38}$$

This analytic expression was derived from the frequency dependent index of refraction for a homogeneously broadened medium in the linear gain regime. The velocity u in the moving frame is thus

$$u^{-1} = v_g^{-1} - c^{-1} = g(z,t)/\Gamma_{1s} \tag{3.39}$$

The rate equation approach with the explicit group velocity will be referred to as modified rate equation approach in the following. The XFEL pump flux J_p is getting absorbed in the medium and its evolution is determined by equation 3.2.

Equations 3.31 and 3.32 for the occupations are solved by a 4th order Runge-Kutta integrator. The propagation of the emitted XRL radiation is more challenging, because of the space and time-dependent velocity $u(z,t)$ in the modified rate equation approach. Finite difference approaches proved to be unstable for numerically solving equation 3.36. A method that provides a numerical stable solution for the XRL flux is a pseudo spectral second order Adams-Bashforth-Moulton method [147]. In this approach the time derivative is calculated in the frequency domain with the Fourier transform $\mathcal{F}$ and transformed back to the time domain by the inverse Fourier transform $\mathcal{F}^{-1}$

$$\frac{\partial J}{\partial t} = \mathcal{F}^{-1}\left[i\omega\, \mathcal{F}\left[J(z,t)\right]\right] \tag{3.40}$$

The Fourier transforms have to be calculated at every space step, but this can be done efficiently with the help of the fast Fourier transform (FFT).

The second order Adams-Bashforth-Moulton is a predictor-corrector method [147]. The method consists of two separate steps and combines an explicit method to predict the solution with an implicit method to correct the initial solution. In an explicit method the solution only depends on previous values and the solution can be directly calculated. In an implicit method on the other hand the solution of $I_{XRL}(z+\Delta z,t)$ depends on the derivative at $z+\Delta z$. This makes it impossible to directly calculate $I_{XRL}(z+\Delta z,t)$ and the equation has to be solved by an iterative process or a predictor corrector approach. Although implicit methods are more difficult to solve they can provide more stable results than explicit methods. This is especially useful for stiff differential equations where explicit methods require impractical small time steps for convergence. Expressing eq. 3.36 as

$$\frac{\partial J}{\partial z} = -\frac{1}{u}\frac{\partial J}{\partial \tau} + gJ + \rho_{1s1s}A_{1s\to 2p}\,n\,\frac{\Omega}{4\pi} = f(z) \tag{3.41}$$

to collect all the terms on the right hand side as $f(z)$ the predictor step is defined by

$$J^{(P)}(z+\Delta z) = J(z) + \frac{3}{2}\Delta z\, f(z) - \frac{1}{2}\Delta z\, f(z-\Delta z)\,. \tag{3.42}$$

This temporary result is used to calculate the derivative $f(z+\Delta z)$ that is required in the corrector step to obtain the solution for the next space point

$$J(z+\Delta z) = J(z) + \frac{1}{12}\Delta z\,\left(5\,f(z+\Delta z, J^{(P)}(z+\Delta z)) + 8f(z) - f(z-\Delta z)\right)\,.$$

This scheme allows a stable propagation of the emitted x-ray intensity with the gain dependent group velocity with a time step size $\Delta t = 0.01\,\mathrm{fs}$ and a space step size $\Delta z = c\Delta t$.

For the comparison between the Maxwell-Bloch model and the rate equation approach two different regimes of the pump pulse duration with respect to the Auger life time will be considered. In one case the pump pulse duration (40 fs) will be much longer than the Auger life time and in the other case the pump pulse duration (10 fs) will be on the order of the Auger life time. The results of the comparison between the rate equation approach and the Maxwell-Bloch approach are summarized in Fig. 3.10 for

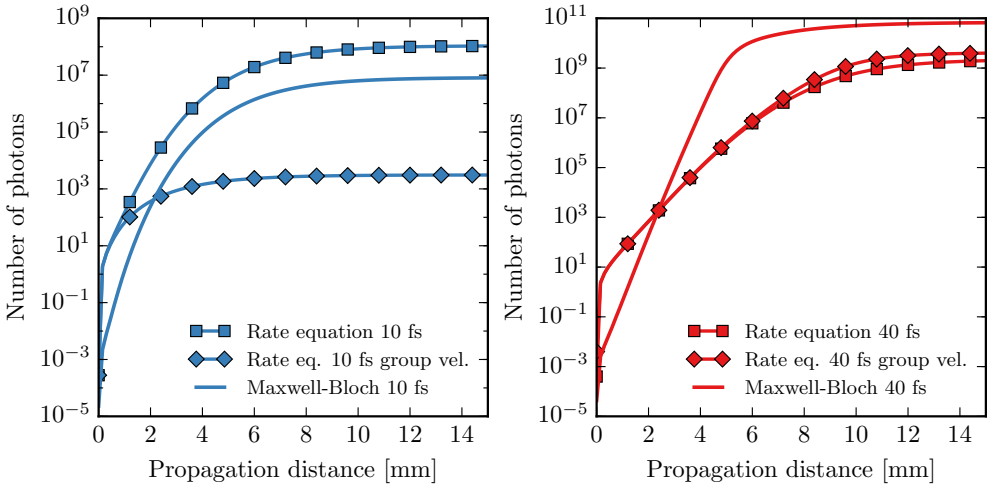

Figure 3.10.: Comparison between the rate equation approach, the modified rate equation approach and the Maxwell-Bloch approach. Comparison is made for two different Gaussian pump pulses with 10 fs and 40 fs pulse duration and 5 $\times 10^{11}$ and 2×10^{12} photons respectively.

the two different pump pulse durations. The figure displays the number of photons as a function of propagation distance for the different approaches. For a 10 fs pump pule duration the rate equation model is overestimating the number of XRL photons by an order of magnitude compared to the Maxwell-Bloch approach. For a short pump pulse the population inversion is propagating with a group velocity close to the speed of light, as can be seen in Fig. 3.11b). In the rate equation approach the XRL also propagates with the speed of light, because the gain-dependent group velocity is not included. This means that the population inversion and the XRL intensity have a very good temporal overlap in the rate equation approach. In the Maxwell-Bloch equation the XRL pulse propagates at a slower group velocity, introducing a slippage with the respect to the population inversion. This leads to an overestimation of the gain for the rate equation approach for short pump pulse durations.

In the case of a pump pulse duration much longer than the Auger life time the situation is reversed. In this case the population inversion propagates at a group velocity significantly slower than the speed of light, see Fig. 3.12c). In the rate equation approach this leads to a big slippage between XRL and population inversion, whereas for the Maxwell-Bloch approach the gain-dependent group velocity ensures a good overlap. As a result the rate equation approach underestimates the gain by almost two

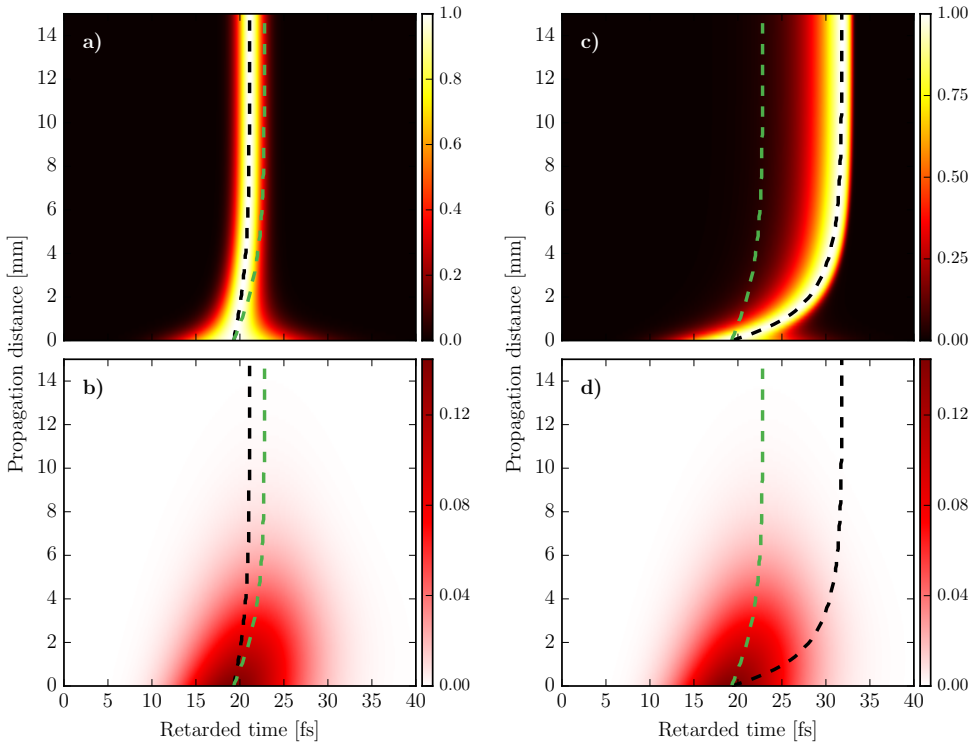

Figure 3.11.: Comparison between the rate equation approach (left) and the modified rate equations with the gain dependent group velocity (right) for a 10 fs Gaussian pump pulse with 5 $\times 10^{11}$ photons. a), c) show the normalized XRL intensity and b), d) depict the population inversion as a function of retarded time and propagation distance. The black dotted line follows the maximum of the XRL intensity while the green dotted line follows the maximum of the population inversion.

orders of magnitude for a 40 fs pump pulse.

The modified rate equation approach with the explicitly included gain-dependent group velocity does not really improve the estimation of the gain for the rate equation approach as can be seen Fig. 3.10. The gain dependent group velocity in the rate equation approach consistently overestimates the slowdown of the group velocity when compared to the Maxwell-Bloch approach. The group velocity in equation 3.38 from [142] only shows qualitative agreement with the one obtained from the Maxwell-Bloch approach. The main problem with the gain dependent group velocity v_g is, that it was derived for a homogeneously broadened line with a fixed bandwidth. Fig. 3.2

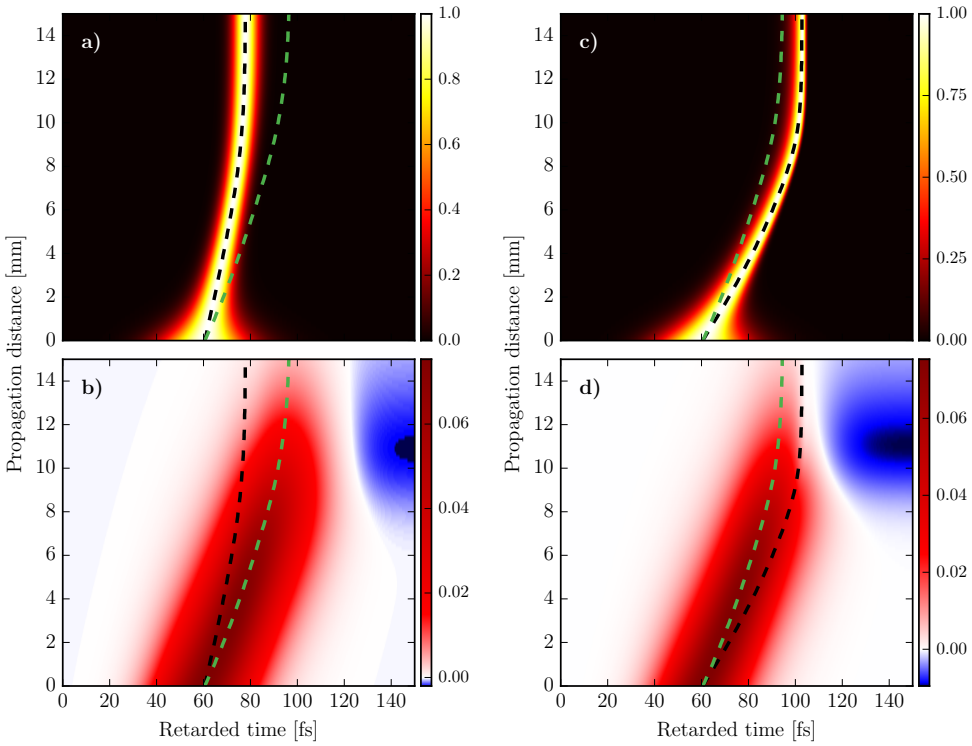

Figure 3.12.: Comparison between the rate equation approach (left) and the modified rate equations with the gain dependent group velocity (right) for a 40 fs Gaussian pump pulse with 2 $\times 10^{12}$ photons. a), c) show the normalized XRL intensity and b), d) depict the population inversion as a function of retarded time and propagation distance. The black dotted line follows the maximum of the XRL intensity while the green dotted line follows the maximum of the population inversion.

though showed that the bandwidth of the emission line changes quite dramatically with propagation. It is not possible to model the dynamic bandwidth with the rate equation approach in a self consistent way. Ad-hoc fixes of adding the gain-dependent group velocity therefore does not improve the overall quality of the rate equation approach. An inherent deficiency of the rate equation approach is the disregard of spectral changes that occur during the propagation and amplification along with the gain dependent group velocity of the amplified radiation. A quantitative modeling of the transient photo-ionization x-ray laser therefore requires a Maxwell-Bloch approach.

3.4. SASE pump pulse

In the following the properties of the emitted x-ray radiation are studied when pumping the amplification process with incoherent SASE radiation [28, 35]. Most x-ray free electron lasers currently produce SASE radiation, which is seeded from noise in the electron bunch. The stochastic nature of the SASE pulses leads to large shot-to-shot fluctuations, a low temporal coherence and a large spectral bandwidth of up to 1% in the soft x-ray regime [35, 121]. The SASE pulses are modeled with a Gaussian power spectrum with a bandwidth of 7 eV (FWHM) and a Gaussian temporal envelope with a pulse duration of 40 fs. The SASE pulses are generated by the method described in section 2.4.3 with 2×10^{12} photons per pulse with a constant focal radius of 2 µm. These values reflect the experimental conditions from recent experiments at the LCLS [1, 75].

In the following the amplification process is studied for two different SASE pump pulses. Due to the stochastic nature individual SASE pulses can vary greatly from another and the individual SASE pulse shape might affect the properties of the emitted x-ray radiation. The two initial SASE pulses before entering the medium are depicted in Fig. 3.13a), b). The two SASE pulses show no dominating temporal spikes or any other distinct feature that sets them apart. Despite the similarity of the two SASE pump pulses, they generate XRL pulses with different characteristics. The temporal pulse shape of the emitted XRL radiation at the end of the gain medium for the different SASE pump pulses is shown in Fig. 3.13 c), d). The left XRL pulse shows a distinct main intensity spike, whereas the right XRL pulse is made up of multiple individual temporal spikes with lower intensity. The different XRL pulse shapes are also reflected in the XRL spectra. Fig. 3.13 e), f) show the XRL spectra at two different points in the gain medium. To test if the XRL pulses are transform limited the actual spectrum (Fourier transform of the complex envelope) are compared with test spectra of the absolute values of the electric field envelope, thus neglecting phase information and assuming a constant phase.

$$I_{test}(\omega) = \left| \int |\mathcal{E}(t)| \, \mathrm{e}^{-i\omega t} dt \right|^2 \tag{3.43}$$

If the actual spectra and the test spectra are equivalent, this means that the XRL pulses have a constant, well defined phase and are transform limited. In the exponential gain

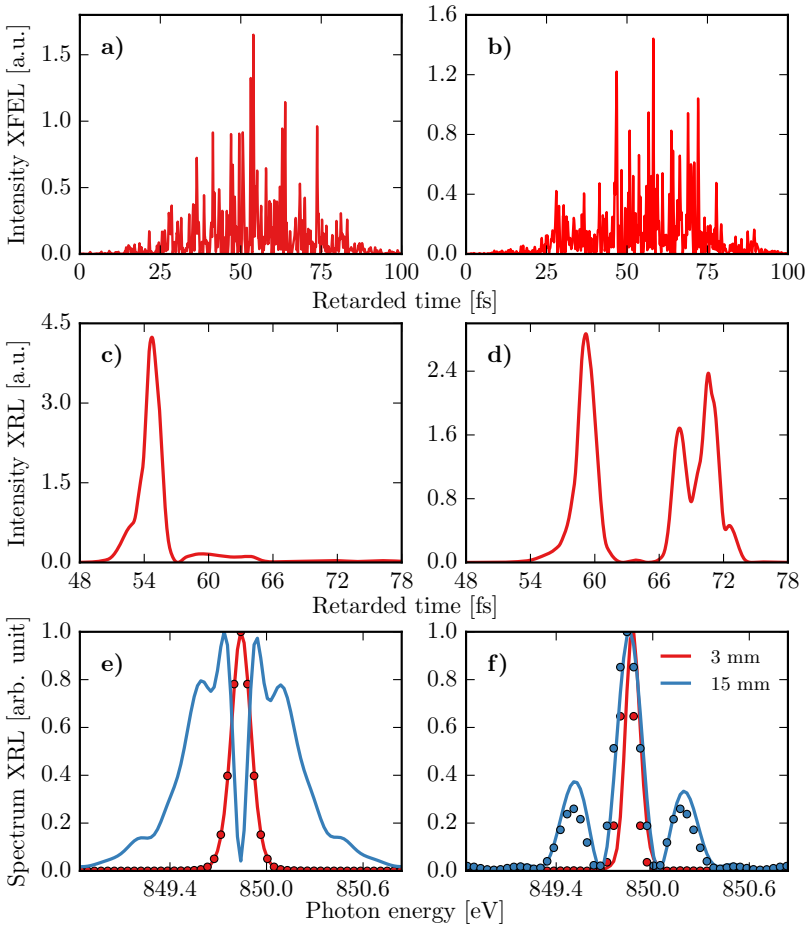

Figure 3.13.: Comparison of the emitted radiation for two different SASE pump pulses. The top row shows the initial temporal structure of the SASE pump pulses. The middle row shows the temporal profile of the emitted XRL radiation at the end of the medium. The bottom shows the XRL spectrum along with the test spectra (points) at two different points in the amplifying medium.

region at 3 mm propagation distance the test spectra (dots) coincide with the actual spectra (solid lines) for both XRL pulses. This confirms the build-up of transform limited XRL pulses, despite pumping the amplification process with incoherent radiation with low temporal coherence. At the end of the medium at 15 mm propagation distance the XRL pulse on the left is no longer transform limited. The high XRL intensity leads to spectral broadening and the Rabi flopping results in a varying phase of the XRL electric field. Due to the lower intensity of the multi-spike XRL pulse on the right, the

saturation effects are less pronounced and the pulse is still almost transform limited at the end of the medium.

To better illustrate the amplification process for the two different SASE pulses the XRL pulse properties are depicted as a function of propagation distance in Fig. 3.14. The temporal XRL pulse profile as a function of propagation distance in Fig.

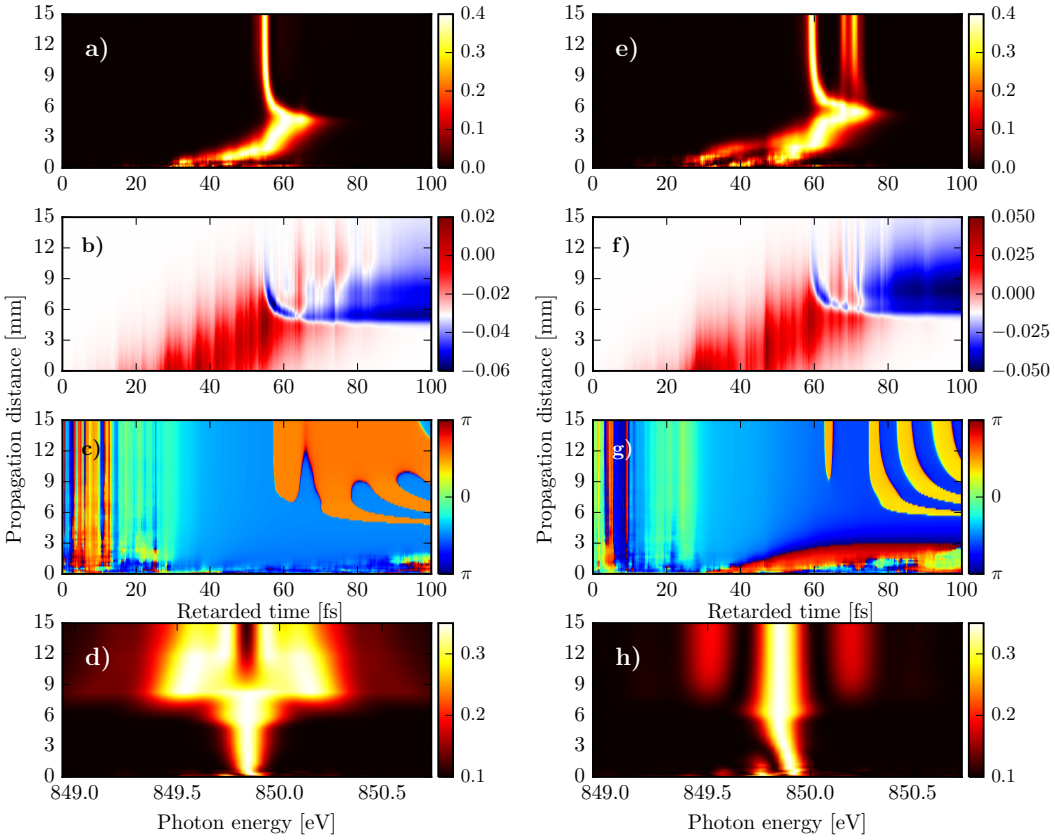

Figure 3.14.: a), e) Evolution of the normalized XRL intensity, b), f) the population inversion, c), g) spectral phase of the XRL radiation and d), h) XRL spectrum for the two different SASE pump pulses from Fig. 3.13.

3.14a), e) show that both SASE pulses initially generate XRL pulses with similar pulse characteristics and a single temporal spike. Only in the saturation regime after 6 mm of propagation, the XRL pulses are strongly reshaped by saturation broadening and Rabi oscillations [148, 149]. These reshaping effects are dependent on the XRL peak intensity, which itself depends on the SASE pump pulse shape. At the onset of

saturation at 6 mm propagation distance the XRL pulse in Fig. 3.14e) gets split into multiple spikes. The initial single-peak XRL pulse with 15 fs pulse duration strongly populates the final lasing state and the population inversion becomes negative at 6 mm propagation distance at 60 fs retarded time in Fig. 3.14g). The negative population inversion leads to a negative gain and absorption of the XRL pulse. The spacing between the first XRL peak and the second XRL peak is 8 fs, which corresponds to half the maximum Rabi oscillation period at 6 mm propagation distance. Despite their similar initial pulse shape, the XRL pulse on the left hand side in Fig. 3.14a) maintains a single peak shape even in the saturated regime.

The Rabi oscillations lead to a π-phase shift between the driving radiation and the emitted radiation [150]. This phase shift can be seen as a ringing pattern in the phase of the XRL pulses in saturation in Fig. 3.14 c), g). Consecutive peaks in this ringing pattern are phase-shifted by π. For the left pulse with the strong peak intensity the ringing pattern in the phase is washed-out in the deep saturation regime after around 9 mm of propagation. There is still a sizable population inversion after the main peak for propagation distances bigger than 9 mm in Fig. 3.14b). The positive population inversion leads to further amplification by stimulated emission. The emitted radiation acquires the phase of the driving field and the phase tends towards a constant phase, rather than the ringing pattern from the Rabi flopping. This effect does not play a role for the pulse of the right hand side in Fig. 3.14f), because the population inversion after the main peaks is mostly negative. This means there is no further stimulated emission and the ringing pattern of the phase in Fig. 3.14g) is maintained even in the deep saturation regime. In summary the XRL pulses generated by incoherent SASE radiation are transform limited until saturation and get strongly reshaped in the saturation regime leading to large shot-to-shot fluctuations in the XRL pulse characteristics.

To study the shot-to-shot fluctuations of the XRL pulses the distribution of the number of temporal peaks per pulse and the arrival time of the main peak are shown in Fig. 3.15. The distribution reveals that most of the XRL pulses have a multi-peak structure and consist of two or three temporal spikes. The arrival time of the main peak shows a broad distribution with a width of 15 fs and is centered around the peak of the XFEL pump pulse.

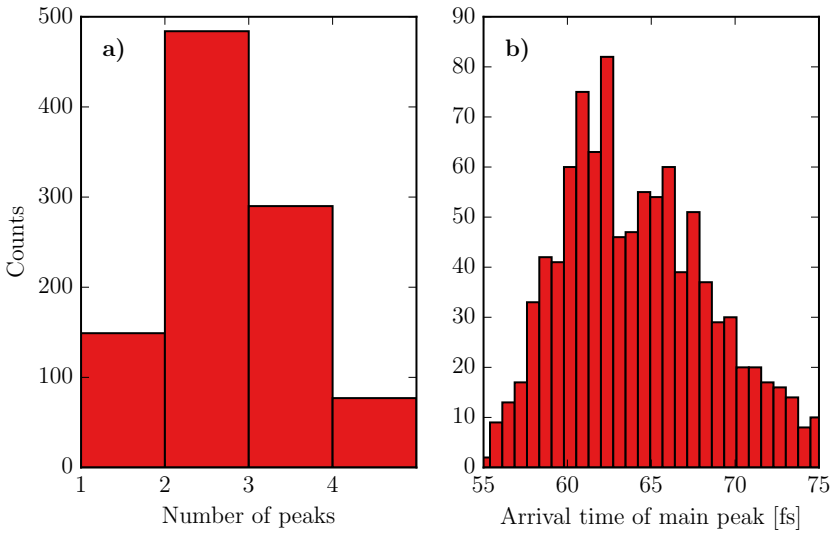

Figure 3.15.: a) Distribution of the number of temporal peaks in the XRL. b) Arrival time of the main XRL peak at the end of the medium. The incoming FEL pulse is centered around 65 fs and the SASE ensemble consists of 2000 shots.

3.4.1. Temporal coherence of the stimulated emission

Another interesting quantity to study is the temporal coherence of the XRL pulses. The XFEL SASE pump pulses have a very low temporal coherence with a typical coherence time of only 0.17 fs for a bandwidth of 7 eV (see eq. 2.35). The previous analysis of the amplified spontaneous emission from incoherent SASE radiation already suggests that the temporal coherence of the emitted radiation should be much larger than for the SASE pulses.

The normalized first order temporal correlation function for the electric field is defined by [151]

$$g^{(1)}(t_1, t_2) = \frac{< E(t_1)\, E^{\star}(t_2) >}{\sqrt{< |E(t_1)|^2 >< |E(t_2)|^2 >}}\,, \tag{3.44}$$

where the brackets $< >$ denote the ensemble average. The generated XRL pulses are non-stationary, meaning that quantities like the mean and the standard deviation are time dependent. In the stationary case the ensemble average can be replaced with a time average. This means that for stationary fields the correlation function $g^{(1)}$ only depends on the difference between the two times $\tau = t_1 - t_2$. In the case of

non-stationary fields the correlation function $g^{(1)}$ though explicitly dependents on t_1 and t_2.

There is no general definition for the coherence time for non-stationary fields. The following paragraph extends the interpretation of correlation function to the non-stationary case. Fig. 3.16a) shows the absolute value of the first order correlation

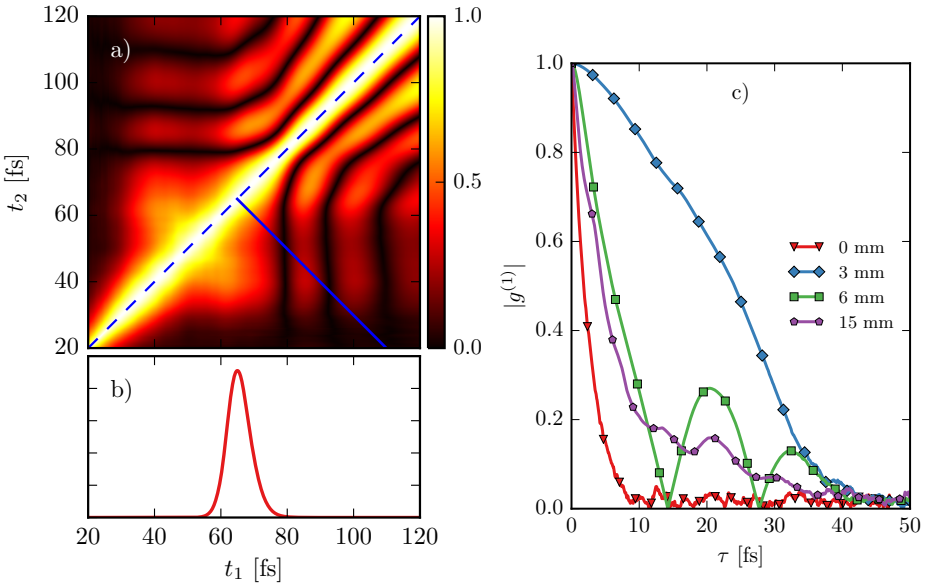

Figure 3.16.: a) Absolute value of the first order correlation function $|g^{(1)}|$ along with the average XRL intensity b) after 6 mm of propagation. c) Value of $|g^{(1)}|$ along the blue line that defines a function of $\tau = t_1 - t_2$ and starts at the maximum of the average intensity. The values for the other propagation distances are taken from the correlation function at their respective propagation distance.

function $|g^{(1)}(t_1, t_2)|$ obtained from an ensemble of 2000 shots after 6 mm of propagation through the gas medium. The plot makes it evident that the correlation explicitly depends on t_1 and t_2 as lines parallel to the main diagonal (blue dotted line) are not constant functions. An approach is to evaluate the coherence $g^{(1)}(t_1, t_2)$ along paths that are perpendicular to the main diagonal where $t_1 = t_2$. These functions then dependent on the difference between the two time arguments τ and can be interpreted like the function $g^{(1)}(\tau)$ in the stationary case. With this approach the reference point along the main diagonal is not yet fixed. A convenient reference point along the main diagonal is the point with the maximum intensity. The blue line in Fig.

3.16a) illustrates the path along which the correlation function $g^{(1)}(t_1, t_2)$ is evaluated to obtain $g^{(1)}(\tau)$. This way one obtains the coherence time for the most intense part of the pulse, which is the most relevant part in most cases. One way to define the coherence time for an arbitrary coherence function, is given by the integral over the square of the absolute value of the correlation function [36].

$$\tau_c = \int_{-\infty}^{\infty} |g^{(1)}(\tau)|^2 d\tau \tag{3.45}$$

The function $|g^{(1)}(\tau)|$ is depicted at four different propagation distances in Fig. 3.16c). In the beginning of the medium the emitted radiation only consists of spontaneous emission and $|g^{(1)}(\tau)|$ shows a fast exponential decay with a lifetime corresponding to the Auger lifetime Γ_{1s}

$$g^{(1)}(\tau) = \mathrm{e}^{-|\tau|\,\Gamma_{1s}}\,. \tag{3.46}$$

The spontaneous emission has a random phase and the radiation is thus incoherent.

In the linear gain regime at 3 mm propagation distance $g^{(1)}(\tau)$ is characterized by a Gaussian decay with a width of 25 fs. The amplified spontaneous emission has a well defined phase and the XRL pulses are coherent. Fig. 3.17 shows the coherence time τ_c along with the number of photons as a function of propagation distance. The coherence time is steadily increasing in the linear gain regime until it quickly drops in saturation.

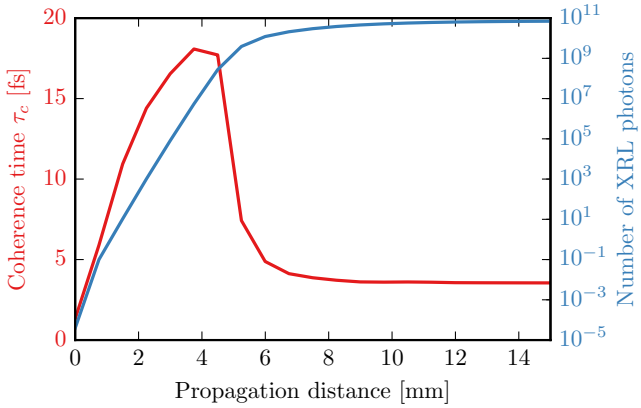

Figure 3.17.: Coherence time τ_c and average number of XRL photons as a function of propagation distance.

At the onset of saturation at 6 mm propagation distance the correlation function changes significantly. The correlation functions functions now displays a fast initial decay with two additional peaks at later delays. The additional peaks in the correlation function come from the multiple temporal peaks in the emitted intensity, see Fig. 3.13d). The multiple intensity peaks are a result of Rabi flopping in the saturation regime and the additional peaks in the correlation function confirm that the intensity peaks are indeed phase correlated. At 13 mm propagation distance these additional peaks in the correlation function $g^{(1)}(\tau)$ disappear again because the phase correlation between the peaks in the emitted intensity is lost by propagation, see Fig. 3.14c).

Chapter 4

Stimulated resonant inelastic x-ray Raman scattering

X-ray Raman scattering is a photon-in/photon-out technique, where the incoming photon is inelastically scattered off the sample and the energy of the emitted photon is detected. X-ray Raman scattering can be used to probe elementary excitations in matter [96, 152, 153] as well as electronic structure [154, 155]. The cross section for x-ray Raman scattering is however much smaller than in the visible domain and poses a challenge to detect enough scattered photons. To overcome the problem of the low scattering cross section, the scattering process can be stimulated to enhance the scattering by several orders of magnitude.

To stimulate the scattering process and to obtain an exponential amplification of the scattered photons the XFEL pulses are focused into an elongated gas target. The stimulated scattering process can either be initiated from the spectral tail of the SASE pulse or a couple of spontaneous scattering events in the beginning of the medium. These initial photons can stimulate the scattering process along the medium, which results in a strong exponential amplification of the scattered photons in forward direction, see Fig. 2.2. After passing through the gas medium the XFEL pulse is strongly attenuated and a strong pulse at lower photon energy is generated.

The process of stimulated Raman scattering has been theoretically studied in the XUV regime [156, 126, 127] with a perturbative expansion of the non-linear polarization. Stimulated Raman scattering has also been studied with a Maxwell-Bloch approach for valence excitations in argon [157] and in lithium and helium [158].

The goal of this thesis was to develop a time domain approach to treat stimulated x-ray Raman scattering as well as amplified spontaneous emission from photo-ionization

in the same theoretical framework. It is necessary to treat resonant excitation and ionization in the same framework, because the pre-edge resonances in neon are only 3 eV below the K edge, see Fig. 2.4. The strongest pre-edge resonance 1s-3p is at 867.5 eV whereas the K edge is at 870.2 eV. The bandwidth of typical XFEL pulses in the soft x-ray regime is around 7 eV, resulting in an overlap of resonant excitation and ionization.

4.1. Kramers–Heisenberg equation

The following section derives the cross section for x-ray scattering. The interaction of a single electron with an electromagnetic field can be described by the minimal coupling Hamiltonian

$$\hat{H}_{\mathrm{int}} = -\frac{\alpha}{2}\left(\hat{\boldsymbol{p}}\cdot\hat{\boldsymbol{A}} + \hat{\boldsymbol{A}}\cdot\hat{\boldsymbol{p}}\right) + \frac{\alpha^2}{2}\hat{\boldsymbol{A}}^2 \tag{4.1}$$

where $\hat{\boldsymbol{p}}$ is the electron momentum and $\hat{\boldsymbol{A}}$ is the vector potential. The vector potential is connected to the electric field $\boldsymbol{E}$ via

$$\boldsymbol{E} = \boldsymbol{\nabla}\phi - \alpha\frac{\partial \boldsymbol{A}}{\partial t} \tag{4.2}$$

where ϕ is the scalar potential. The vector potential can be expanded in modes

$$\hat{\boldsymbol{A}}(\boldsymbol{r}) = \sum_{\boldsymbol{k},\lambda}\sqrt{\frac{2\pi}{V\omega_{\boldsymbol{k}}\alpha^2}}\left\{\hat{a}_{\boldsymbol{k},\lambda}\,\boldsymbol{\epsilon}_{\boldsymbol{k},\lambda}\,\mathrm{e}^{i\boldsymbol{k}\cdot\boldsymbol{r}} + \hat{a}^{\dagger}_{\boldsymbol{k},\lambda}\,\boldsymbol{\epsilon}^{\star}{}_{\boldsymbol{k},\lambda}\,\mathrm{e}^{-i\boldsymbol{k}\cdot\boldsymbol{r}}\right\} \tag{4.3}$$

where the modes are characterized by the wavevector $\boldsymbol{k}$ and the polarization vector $\boldsymbol{\epsilon}_{\boldsymbol{k},\lambda}$ ($\lambda = 1, 2$), $\hat{a}_{\boldsymbol{k},\lambda}$ is the annihilation operator and $\hat{a}^{\dagger}_{\boldsymbol{k},\lambda}$ is the creation operator for the respective mode.

The minimal coupling Hamiltonian can be split into two different parts. The first part $\hat{H}_1$ contains interactions which are second order in $\hat{\boldsymbol{A}}$

$$\hat{H}_1 = \frac{\alpha^2}{2}\hat{\boldsymbol{A}}^2\,. \tag{4.4}$$

Whereas $\hat{H}_2$ contains interactions which are fist order in $\hat{\boldsymbol{A}}$. In the Coulomb gauge

$\boldsymbol{\nabla} \cdot \boldsymbol{A} = 0$ the Hamiltonian $\hat{H}_2$ can be expressed as

$$\hat{H}_2 = -\alpha \hat{\boldsymbol{A}} \cdot \hat{\boldsymbol{p}} \,. \tag{4.5}$$

The scattering cross section can be derived from Fermi's golden rule. In the scattering process the incoming photon is absorbed and a scattered photon is emitted. The state vector of the system can be represented as a product of the electronic state and the radiation field, expressed as Fock states. The initial state $|I\rangle = |i\rangle\,|\omega_i\rangle$ is composed of the initial electric state $|i\rangle$ and the incoming radiation field $|\omega_i\rangle$. The final state $|F\rangle = |f\rangle\,|\omega_f\rangle$ consists of the final electronic state $|i\rangle$ and the radiation field in the state $|\omega_f\rangle$, where the incoming photon has been absorbed and a scattered photon is emitted.

This process requires two interactions with the vector potential $\boldsymbol{A}$. In lowest order perturbation theory this means that the $\boldsymbol{A}^2$ term in $\hat{H}_1$ contributes in first order and $\boldsymbol{p}\cdot\boldsymbol{A}$ term in $\hat{H}_2$ contributes in second order. The transition probability from the initial state $|I\rangle$ to the final state $|F\rangle$ in second order perturbation theory is given by [159]

$$\Gamma_{FI} = \left| \langle F|H_1|I\rangle + \sum_M \frac{\langle F|H_2|M\rangle\langle M|H_2|I\rangle}{E_I - E_M} \right|^2 2\pi\delta(E_F - E_I) \tag{4.6}$$

where $|M\rangle$ is the core-excited intermediate state. There are two different possibilities for the intermediate state. The first possibility is that, in the intermediate state the incoming photon ω_i has been annihilated and the intermediate state $|m_1\rangle = |m\rangle\,|0\rangle$ consists of only the electric intermediate state $|m\rangle$. The other possibility is that the scattered photon is emitted first and the intermediate consists of $|m_2\rangle = |m\rangle\,|\omega_f\rangle$.

The double differential cross section for x-ray scattering up to second order perturbation theory is determined by

$$\begin{aligned}\frac{d^2\sigma}{d\omega_f\, d\Omega} = \alpha^4 \frac{\omega_f}{\omega_i} \Bigg| & \boldsymbol{\epsilon_i}\cdot\boldsymbol{\epsilon_f^*}\langle f|\mathrm{e}^{i(\boldsymbol{k_i}-\boldsymbol{k_f})\cdot\boldsymbol{r}}|i\rangle \\ & + \sum_{m_1} \frac{\langle f|\boldsymbol{p}\cdot\boldsymbol{\epsilon_f^\star}\,\mathrm{e}^{-i\boldsymbol{k_f}\cdot\boldsymbol{r}}|m_1\rangle\langle m_1|\boldsymbol{p}\cdot\boldsymbol{\epsilon_i}\,\mathrm{e}^{i\boldsymbol{k_i}\cdot\boldsymbol{r}}|i\rangle}{E_i - E_{m_1} + \omega_i - i\Gamma_m/2} \\ & + \sum_{m_2} \frac{\langle f|\boldsymbol{p}\cdot\boldsymbol{\epsilon_i}\,\mathrm{e}^{i\boldsymbol{k_i}\cdot\boldsymbol{r}}|m_2\rangle\langle m_2|\boldsymbol{p}\cdot\boldsymbol{\epsilon_f^\star}\,\mathrm{e}^{-i\boldsymbol{k_f}\cdot\boldsymbol{r}}|i\rangle}{E_i - E_{m_2} - \omega_f} \Bigg|^2 \delta(E_f + \omega_f - E_i - \omega_i)\end{aligned} \tag{4.7}$$

The scattering cross section consists of three different contributions. The first term in the scattering cross section describes Thomson scattering by the $\boldsymbol{A}^2$ term of the interaction Hamiltonian. The other two terms in the cross section are a result of the $\boldsymbol{p} \cdot \boldsymbol{A}$ term in second order. The second term describes resonant Raman scattering, where the incoming photon is annihilated and afterwards the scattered photon is created. In this scattering contribution the term $i\Gamma_m/2$ was added to the denominator to account for the lifetime of the intermediate core-excited state. Whereas the last term describes the Raman scattering process in reversed order. Here the scattered photon ω_f is emitted first and then the incoming photon ω_i is annihilated. If the incoming radiation ω_1 is close to the resonance energy $E_i - E_m$ the scattering contribution from the second term dominates and the other scattering contributions can be neglected. The Raman scattering cross section is hence

$$\frac{d^2\sigma}{d\omega_f\, d\Omega} = \alpha^4 \frac{\omega_f}{\omega_i} \left| \sum_{m_1} \frac{\langle f \,|\boldsymbol{p} \cdot \boldsymbol{\epsilon}_{\boldsymbol{f}}^{\star}\, \mathrm{e}^{-i\boldsymbol{k_f}\cdot\boldsymbol{r}}\, | m_1 \rangle \langle m_1 \,|\boldsymbol{p} \cdot \boldsymbol{\epsilon_i}\, \mathrm{e}^{i\boldsymbol{k_i}\cdot\boldsymbol{r}}\, | i \rangle}{E_i - E_{m_1} + \omega_i - i\Gamma_m/2} \right|^2 \delta(E_f + \omega_f - E_i - \omega_i) \tag{4.8}$$

In the theoretical description of the Raman scattering mechanism the absorption and emission process have to be combined into a single inelastic scattering event. From the energy conservation in the δ-function in the Raman cross section (eq. 4.8) one obtains a relation between the incoming photon energy ω_i and the outgoing photon energy ω_f. The outgoing photon energy is equal to the difference between the incoming photon energy and the energy difference between final state E_f and initial state E_i [160]

$$\omega_f = \omega_i - (E_f - E_i)\,. \tag{4.9}$$

4.2. Theoretical approach

This section presents a model to describe the excitation of neon around the K edge with an XFEL pulse. Using a broadband x-ray pulse tuned around the K edge leads to resonant excitation of electrons as well as photo-ionization. Fig. 4.1 shows the level scheme with the corresponding couplings. The part of the XFEL spectrum above the

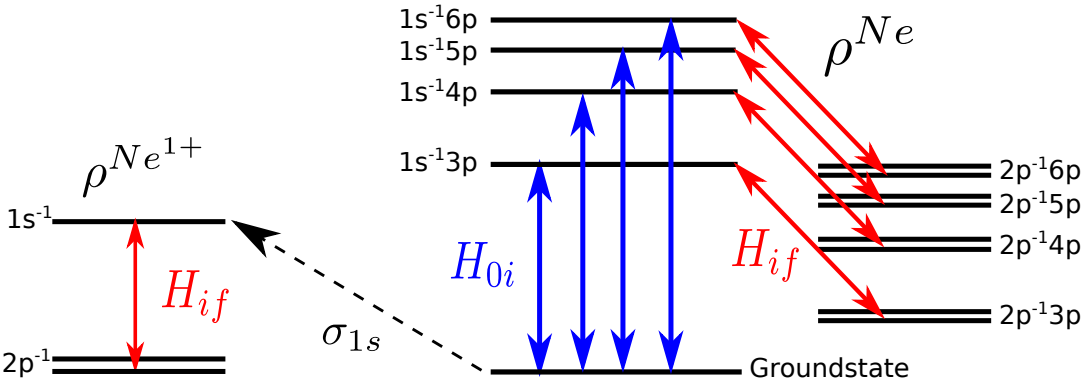

Figure 4.1.: Level scheme of neon for excitation around the K edge. The black dotted line denotes photo-ionization of core-electrons, yielding singly charged neon Ne^{1+}. The blue arrows H_{0i} represent the resonant coupling of the XFEL pump pulse to the core-excited inter-mediate states. The red arrows H_{if} represent the coupling of the core-excited intermediate states to the corresponding final state doublets. This leads to stimulated fluorescence in the case of Ne^{1+} and to stimulated Raman scattering for the neutral neon.

K edge can photo-ionize inner-shell 1s electrons with the cross section σ_{1s}, yielding singly charged neon ions. The core-excited state $1s^{-1}$ in Ne^{1+} can decay via Auger decay and is coupled to the final state doublet $2p^{-1}\ ^2P_{1/2}$, $2p^{-1}\ ^2P_{3/2}$. The part of the XFEL spectrum below the K edge can resonantly excite 1s electrons to the unoccupied orbitals 3p, 4p, 5p, 6p. These core-excited states can again decay via Auger decay and are coupled to the corresponding valence-excited final state doublet $2p^{-1}$ $np^1\ ^1D_2$, $2p^{-1}$ $np^1\ ^1S_0$. The final states consist of a hole in the 2p shell along with a spectator electron in the corresponding shell n=$\{3p-6p\}$.

To simulate the scattering process a generalized one-dimensional Maxwell-Liouville–von Neumann approach was developed. The approach allows to self-consistently solve for the amplification of the inelastically scattered radiation and to also include the amplified fluorescence from the ionic system. The atomic and ionic system are treated quantum mechanically by separate density matrices, introduced in section 2.2 and the emitted radiation is treated by a classical electric field. Due to the elongated geometry (see Fig. 2.2) of the gas medium only the z-axis along the propagation direction is considered and transverse dimensions are neglected. The broadband XFEL radiation still has a

considerable number of photons around 849 eV when tuned to the neon K edge. A Gaussian XFEL pulse with a bandwidth of 7 eV (FWHM) has around 10^4 photons at 849 eV and the XFEL pulse therefore also seeds the amplification process. Since the XFEL radiation is typically linearly polarized, the scattered radiation is assumed to have the same linear polarization as the XFEL.

To include the absorption of the XFEL from resonant excitation as well as photo-ionization, the step-like behavior of the 1s photo-ionization cross section around the K edge has to be considered. This means that only the spectral part of the XFEL pulse above the neon K edge can photo-ionize 1s electrons. Since the Maxwell-Liouville–von Neumann approach propagates the solution in real time and space the spectral information is not accessible during the simulation. This is in contrast to frequency domain techniques [92] where the non-linear response of the medium is obtained from a perturbative solution in the frequency domain. In the time domain however it is not straightforward to model the frequency dependence of the absorption cross section around the K edge. A convenient solution to this problem is to split the initial SASE pulse into a part below the K edge and a part above the K edge. These two parts are assumed to be independent and do not directly interact with each other. These two parts can be treated separately and make it feasible to account for resonant excitation as well as photo-ionization in a time domain approach.

The part of the initial SASE pulse above the K edge is treated by the time-dependent flux $J_p(\tau, z)$, where $\tau = t - \frac{z}{c}$ is the retarded time in the frame moving along with the pump pulse, see section 2.3. The evolution of the flux is governed by

$$\frac{\partial J_p(\tau, z)}{\partial z} = -n\,\sigma_{\text{tot}}\,\rho_{0,0}(\tau, z)\,J_p(\tau, z)\,, \tag{4.10}$$

where n denotes the neon particle density, σ_{tot} is total photo-ionization cross section and $\rho_{0,0}(\tau, z)$ is the groundstate population. It is sufficient to treat the spectral part of the XFEL pulse above the K edge as an intensity flux, rather than a complex electric field. This spectral part of the XFEL is responsible for photo-ionization. The photo-ionization cross section above the K edge is assumed to be constant.

The part of the initial SASE pulse below the K edge and the inelastic scattered radiation are treated by a classical electric field. The same slowly varying envelop approximation as in section 2.3 is employed and the field is determined by equation 2.15. This description does not allow to take spontaneous Raman scattering into account.

The amplification of spontaneous Raman scattering requires operator equations for the field to properly account for the spontaneous scattering [161]. This thesis only considers the amplification of the SASE spectral tail by stimulated Raman scattering.

To derive the master equations for the time evolution of the atomic system including photo-ionization and resonant excitation one starts from an appropriate expansion of the wave function. The atomic system was introduced in section 2.2 and the derivation follows a pattern similar to the one in section 3.1 for deriving the equations in the case of x-ray lasing. The wave function of the system can be well described by the configuration interaction approach. In this approach the wave function in the interaction picture $|\Psi, t\rangle_I$ is expanded in the groundstate $|\phi_0\rangle$ and single particle hole excitations $|\phi_i^a{}_J\rangle$

$$|\Psi, t\rangle_I = \alpha_0(t)\,|\phi_0\rangle + \sum_{i,a,J} \alpha_i^a{}_J(t)\,|\phi_i^a{}_J\rangle \tag{4.11}$$

with time dependent expansion coefficients $\alpha_0(t)$ and $\alpha_i^a{}_J(t)$. The configuration interaction expansion in principle includes higher order terms with double excitations, triple excitations and so on. With the single particle hole excitations we can already represent all relevant levels in this atomic system and therefore neglect the higher order terms in the expansion. The single particle hole excitations $|\phi_i^a{}_J\rangle$ are generated from the ground state by exciting an electron from an initially occupied orbital i to an unoccupied orbital a, yielding a state with total angular momentum J:

$$|\phi_i^a{}_J\rangle = \frac{1}{\sqrt{2}}\left(\hat{b}^\dagger_{a\uparrow}\,\hat{b}_{i\uparrow} + \hat{b}^\dagger_{a\downarrow}\,\hat{b}_{i\downarrow}\right)|\phi_0\rangle \tag{4.12}$$

Where $\hat{b}_i$ is the annihilation operator and removes an electron from orbital i and $\hat{b}^\dagger_a$ is the creation operator to generate an electron in the orbital a. Only spin-singlet states are considered as the total spin is conserved in the interaction. The intermediate core-excited states I^{np} have a hole in the 1s shell, an excitation in the np shell and a fixed total angular momentum of one. The final states F^{np}_J have a hole in the 2p shell with an excitation in the np shell with total angular momentum J

$$\begin{aligned} I^{np} &= {}^{np}_{1s}1 \\ F^{np}_J &= {}^{np}_{2p}J\,. \end{aligned}$$

The interaction Hamiltonian H_{int} in the dipole approximation in the Schrödinger

picture is

$$\hat{H}_{\text{int}} = -\hat{z}E(t)\,, \tag{4.13}$$

which can be transformed to the interaction picture with the unitary transformation

$$\hat{H}_I = \mathrm{e}^{i\hat{H}_0 t}\,\hat{H}_{\text{int}}\,\mathrm{e}^{-i\hat{H}_0 t}\,. \tag{4.14}$$

To derive an equation for the expansion coefficients $\alpha_0(t)$ and $\alpha_{i^a J}(t)$ the expansion of the wavefunction 4.11 is inserted into the time dependent Schrödinger equation

$$i\frac{\partial}{\partial t}\,|\Psi,t\rangle_I = H_I\,|\Psi,t\rangle_I \tag{4.15}$$

The electric field $E(t)$ in the interaction Hamiltonian $\hat{H}_{\text{int}}$ is expanded into a slowly varying envelope $\mathcal{E}$, see equation 2.12. Performing the rotating wave approximation which neglects fast oscillating terms in the Hamiltonian yields the following expression for the coefficients

$$\dot{\alpha}_0 = \frac{i}{2}\mathcal{E}^\star(t)\sum_n \alpha_{I^{np}}\,\langle\phi_0|\hat{z}\,|\phi_{I^{np}}\rangle\,\mathrm{e}^{i(\omega-\omega_{I^{np}})t} \tag{4.16}$$

$$\begin{aligned}\dot{\alpha}_{I^{np}} &= \frac{i}{2}\alpha_0\langle\phi_{I^{np}}|\hat{z}\,|\phi_0\rangle\,\mathcal{E}(t)\,\mathrm{e}^{i(\omega_{I^{np}}-\omega)t} \\ &+ \frac{i}{2}\alpha_{F_J^{np}}\langle\phi_{I^{np}}|\hat{z}\,|\phi_{F_J^{np}}\rangle\,\mathcal{E}(t)\,\mathrm{e}^{i(\omega_{I^{np}}-\omega_{F_J^{np}}-\omega)t} - \frac{\Gamma}{2}\,\alpha_{I^{np}}\end{aligned} \tag{4.17}$$

$$\dot{\alpha}_{F_J^{np}} = \frac{i}{2}\alpha_{I^{np}}\langle\phi_{F_J^{np}}|\hat{z}\,|\phi_{I^{np}}\rangle\,\mathcal{E}^\star(t)\,\mathrm{e}^{i(\omega-\omega_{I^{np}}+\omega_{F_J^{np}})t} \tag{4.18}$$

where the Auger decay Γ for the core-excited states was introduced phenomenologically [20]. Collecting terms, the coupling between the groundstate and the core-excited states and between the core-excited states and the final states are expressed as

$$R_{0,I^{np}} = \frac{1}{2}\,\langle\phi_0|\hat{z}\,|\phi_{I^{np}}\rangle\,\mathcal{E}^\star(t)\,\mathrm{e}^{i(\omega-\omega_{I^{np}})t} \tag{4.19}$$

$$R_{I^{np},F_J^{np}} = \frac{1}{2}\,\langle\phi_{I^{np}}|\hat{z}\,|\phi_{F_J^{np}}\rangle\,\mathcal{E}(t)\,\mathrm{e}^{i(\omega_{I^{np}}-\omega_{F_J^{np}}-\omega)t} \tag{4.20}$$

From the expansion coefficients the density matrix elements can be computed. The density matrix for the singly charged ion Ne^{1+} is a reduced ionic density matrix. In the case of photo-ionization the outgoing photo electron is not observed and its state

is not relevant for stimulated x-ray emission from the ion. To obtain a reduced density matrix for the ion a trace over the continuum states can be performed, following an open quantum system approach [106]

$$\rho^{1+}_{j J,k J'}(t) = \sum_{c \in cont.} \alpha^{c}_{j J}(t) \alpha^{\star}_{c \atop k J'}(t) \tag{4.21}$$

The density matrix for the neutral atom is defined by

$$\rho_{{a \atop j} J,{a' \atop k} J'}(t) = \alpha_{{a \atop j} J}(t) \alpha^{\star}_{{a' \atop k} J'}(t) \ . \tag{4.22}$$

where the excitation a and $a^{'}$ are discrete states in the neutral neon atom. The density matrix of the neural atom contains the neon groundstate $\rho_{0,0}$, the population of the intermediate states $\rho_{I^{np},I^{np}}$ and the final states $\rho_{F^{np}_J,F^{np}_J}$. These density matrix also includes the coherences between the intermediate states and the groundstate $\rho_{I^{np},0}$, between the intermediate states and the final states ρ_{I^{np},F^{mp}_J}, between the intermediate states $\rho_{I^{np},I^{mp}}$ and between the final states $\rho_{F^{np}_J,F^{mp}_{J'}}$.

The evolution of the ground state is determined by

$$\dot{\rho}_{0,0} = \dot{\alpha}_0 \alpha^{\star}_0 + \alpha_0 \dot{\alpha}^{\star}_0 = -\left[\sigma_{1s} J_p + \sigma_v (J + J_p)\right] \rho_{00} - 2\,\mathrm{Im} \sum_I R_{0,I^{np}}\, \rho_{I^{np},0} \tag{4.23}$$

where the depopulation of the groundstate due to ionization was added. The pump flux above the K edge J_p can photo-ionize 1s electrons and the sum of J_p and the flux below the edge J can photo-ionize valence electrons with the cross section σ_v. The population of the intermediate and final states of the density matrix for the neutral atom (diagonal elements of the matrix) evolve according to

$$\dot{\rho}_{I^{np},I^{np}} = -\Gamma \rho_{I^{np},I^{np}} - 2\,\mathrm{Im} \left(R_{I^{np},0}\, \rho_{0,I^{np}} + \sum_F R_{I^{np},F^{np}_J}\, \rho_{F^{np}_J,I^{np}} \right) \tag{4.24}$$

$$\dot{\rho}_{F^{np}_J,F^{np}_J} = -2\,\mathrm{Im}\, R_{F^{np}_J,I^{np}}\, \rho_{I^{np},F^{np}_J} \tag{4.25}$$

The evolution of the coherences (off-diagonal matrix elements) between the intermediate states and the final states and between the intermediate states and the final states in

the neutral atom are determined by

$$\begin{aligned}
\dot{\rho}_{I^{np},0} &= -\frac{1}{2}(\Gamma+\sigma_{1s}J_p)\rho_{I^{np},0} + iR_{I^{np},0}\rho_{0,0} + i\sum_F R_{I^{np},F_J^{np}}\rho_{F_J^{np},0} - i\sum_I R_{I^{np},0}\,\rho_{I^{np},I^{np}} \\
\dot{\rho}_{I^{np},F_J^{mp}} &= -\frac{\Gamma}{2}\rho_{I^{np},F_J^{mp}} + iR_{I^{np},0}\rho_{0,F_J^{mp}} + i\sum_F R_{I_J^{np},F_J^{np}}\rho_{F_J^{np},F_{J'}^{mp}} - iR_{I^{mp},F_J^{mp}}\,\rho_{I^{np},I^{mp}}
\end{aligned}$$

The coherences between the intermediate states and the coherence between the final states are determined by

$$\begin{aligned}
\dot{\rho}_{I^{np},I^{mp}} &= -\Gamma\rho_{I^{np},I^{mp}} + iR_{I^{np},0}\rho_{0,I^{mp}} + i\sum_F R_{I^{np},F_J^{np}}\,\rho_{F_J^{np},I^{mp}} \\
&- iR_{0,I_J^{mp}}\,\rho_{I^{np},0} - i\sum_F R_{F_J^{mp},I^{mp}}\,\rho_{I^{np},F_J^{mp}} \\
\dot{\rho}_{F_J^{np},F_{J'}^{mp}} &= iR_{F_J^{np},I^{np}}\rho_{I^{np},F_{J'}^{mp}} - iR_{I^{mp},F_{J'}^{mp}}\,\rho_{F_J^{np},I^{mp}} \qquad \text{for } n\neq m
\end{aligned}$$

The reduced density matrix for the singly charged ion ρ^{1+} is composed of the core-ionized intermediate state $|i\rangle = 1s^{-1}$ with a hole in the 1s shell and the final state doublet $|f\rangle = 2p^{-1}\,J$ with a hole in the 2p shell and a total angular momentum of $J = 1/2,\ 3/2$. The populations and coherences of the reduced density matrix for the singly charged ion evolve according to

$$\begin{aligned}
\dot{\rho}_{ii}^{1+} &= \sigma_{1s}J_p\rho_{00} - \Gamma\rho_{ii}^{1+} - 2\,\mathrm{Im}\sum_f R_{if}\rho_{fi}^{1+} \\
\dot{\rho}_{ff}^{1+} &= \sigma_{2p}\left[J+J_p\right]\rho_{00} + 2\,\mathrm{Im}R_{if}\rho_{fi}^{1+} \\
\dot{\rho}_{if}^{1+} &= -\frac{\Gamma}{2}\rho_{if}^{1+} + i\sum_{f'} R_{if'}\rho_{f'f}^{1+} - iR_{if}\rho_{ii}^{1+}
\end{aligned} \tag{4.26}$$

Table 4.1 gives an overview over all the relevant transitions and their corresponding transition energies along with the transition dipole moment.

With these equations the time evolution of the atomic system is determined. The atomic system is coupled to the Maxwell equations via the polarization $P(t)$. The polarization is proportional to the density n times the expectation value of the dipole operator $\hat{z}$. The expectation value of the dipole operator is given by the trace of $\hat{\rho}$

	Transition	Energy [eV]	Transition dipole [a.u.]
Excitation			
Ne	$\|0\rangle \rightarrow 1s^{-1}3p\,^1P_1$	867.5	7.7×10^{-3}
	$\|0\rangle \rightarrow 1s^{-1}4p\,^1P_1$	869.2	4.4×10^{-3}
	$\|0\rangle \rightarrow 1s^{-1}5p\,^1P_1$	869.8	3.0×10^{-3}
	$\|0\rangle \rightarrow 1s^{-1}6p\,^1P_1$	870.0	2.2×10^{-3}
	K-edge	870.2	
Emission			
Ne	$1s^{-1}3p\,^1P_1 \rightarrow 2p^{-1}3p\,^1S_0$	849.3	4.8×10^{-2}
	$1s^{-1}3p\,^1P_1 \rightarrow 2p^{-1}3p\,^1D_2$	849.7	4.0×10^{-2}
	$1s^{-1}4p\,^1P_1 \rightarrow 2p^{-1}4p\,^1S_0$	849.6	4.5×10^{-2}
	$1s^{-1}4p\,^1P_1 \rightarrow 2p^{-1}4p\,^1D_2$	849.7	4.2×10^{-2}
	$1s^{-1}5p\,^1P_1 \rightarrow 2p^{-1}5p\,^1S_0$	849.7	3.8×10^{-2}
	$1s^{-1}5p\,^1P_1 \rightarrow 2p^{-1}5p\,^1D_2$	849.7	4.1×10^{-2}
	$1s^{-1}6p\,^1P_1 \rightarrow 2p^{-1}6p\,^1S_0$	849.7	3.3×10^{-2}
	$1s^{-1}6p\,^1P_1 \rightarrow 2p^{-1}6p\,^1D_2$	849.7	4.0×10^{-2}
Ne^{1+}	$1s^{-1}\,^2S_{1/2} \rightarrow 2p^{-1}\,^2P_{1/2}$	849.8	4.8×10^{-2}
	$1s^{-1}\,^2S_{1/2} \rightarrow 2p^{-1}\,^2P_{3/2}$	849.8	6.8×10^{-2}

Table 4.1.: Transition energies and dipole moments, calculated with the Cowan code [132].

times $\hat{z}$.

$$P(t) = n < \hat{z} > = n\,\mathrm{Tr}(\rho\,\hat{z}) \tag{4.27}$$

Since the density matrix is computed in the interaction picture is has to be transformed back into the Schrödinger picture.

$$\rho_S = \mathrm{e}^{-i\hat{H}_0 t}\,\rho\,\mathrm{e}^{i\hat{H}_0 t} \tag{4.28}$$

Calculating the polarization with the density matrix in the Schrödinger picture results in

$$\begin{aligned} P(t) = n\{ &\sum_I z_{0,I^{np}}\,\rho_{0,I^{np}}\,\mathrm{e}^{i\omega_{I^{np}}t} + \sum_{I,F} z_{I^{np},F_J^{np}}\,\rho_{I^{np},F_J^{np}}\,\mathrm{e}^{i(\omega_{F_J^{np}}-\omega_{I^{np}})t} + \\ &\sum_I z_{I^{np},0}\,\rho_{I^{np},0}\,\mathrm{e}^{-i\omega_{I^{np}}t} + \sum_{I,F} z_{F_J^{np},I^{np}}\,\rho_{F_J^{np},I^{np}}\,\mathrm{e}^{-i(\omega_{F_J^{np}}-\omega_{I^{np}})t}\,\} \end{aligned} \tag{4.29}$$

This equation for the polarization can be compared to the expansion of the polarization

to obtain an equation for the envelope $\mathcal{P}$, see eq. 2.13

$$P(t) = \frac{1}{2}\left\{\mathcal{P}(t)\,\mathrm{e}^{i(kz-\omega t)} + \mathcal{P}^{\star}(t)\,\mathrm{e}^{-i(kz-\omega t)}\right\} \tag{4.30}$$

To obtain an equation for the envelope $\mathcal{P}(t)$ equation 4.30 is multiplied with $\mathrm{e}^{-i(kz-\omega t)}$ and compared to equation 4.29. Performing the rotating wave approximation to neglect the fast oscillating exponents yields the final expression for the polarization

$$\mathcal{P}(t) = 2\,n\left(\sum_{I}\mu_{I^{np},0}\,\rho_{I^{np},0}\,\mathrm{e}^{i(\omega-\omega_{I^{np}})t} + \sum_{I,F}\mu_{I^{np},F_J^{np}}\rho_{I^{np},F_J^{np}}\,\mathrm{e}^{i(\omega-\omega_{I^{np}}+\omega_{F_J^{np}})t}\right)$$

The same calculation can be performed to calculate the polarization for the density matrix of the neon ion ρ^{1+}

$$\mathcal{P}^{1+}(t) = 2\,n\sum_{f} z_{if}\rho_{if}^{1+}\mathrm{e}^{i(\omega-\omega_{if})t} \tag{4.31}$$

The polarization of the complete system is the sum of $\mathcal{P}(t)$ and $\mathcal{P}^{1+}(t)$.

The density matrix for the atomic and ionic system are solved by the split step method described in section 2.4.1 and are self consistently coupled to the electric field in eq. 2.15 via the polarization. The time step Δt was chosen to be 0.01 fs and the space step Δz was set to $c\,\Delta t$ for all simulations. Convergence was checked by further decreasing the time step, which did not change the numerical solution.

The presented framework is used to study the evolution of stimulated inelastic Raman scattering in neon with XFEL excitation around the K edge. In the following the broadband XFEL is assumed to have a bandwidth of 7 eV (FWHM) with a pulse duration of 40 fs and a focal radius of 2 µm. Fig. 4.6 shows the stimulation of x-ray Raman scattering in neon for a single SASE pulse with a central photon energy of 866 eV. The incoming broadband XFEL pulse has a total of 1.5×10^{12} photons with initially 6×10^{5} photons in the emission region between 847-851 eV. After passing through a 15 mm long elongated neon gas target the spectrum is strongly altered and shows several absorption dips and emission peaks. The number of photons in the emission region around 847-851 eV got exponentially amplified by 4 orders of magnitude to yield 6.4×10^{9} photons. The absorption of the resonances leads to strong absorption dips in the spectrum in the energy region below 870 eV. The broad emission peak to

the left of 849 eV is degenerate four-wave mixing [162]. Four-wave mixing is a third order non-linear effect which generates a new emission frequency ω_m which is twice the emission frequency of the stimulated Raman scattering at 849 eV minus the frequency of the SASE pulse.

$$\omega_m = 2\,\omega_{\text{Raman}} - \omega_{\text{SASE}}$$

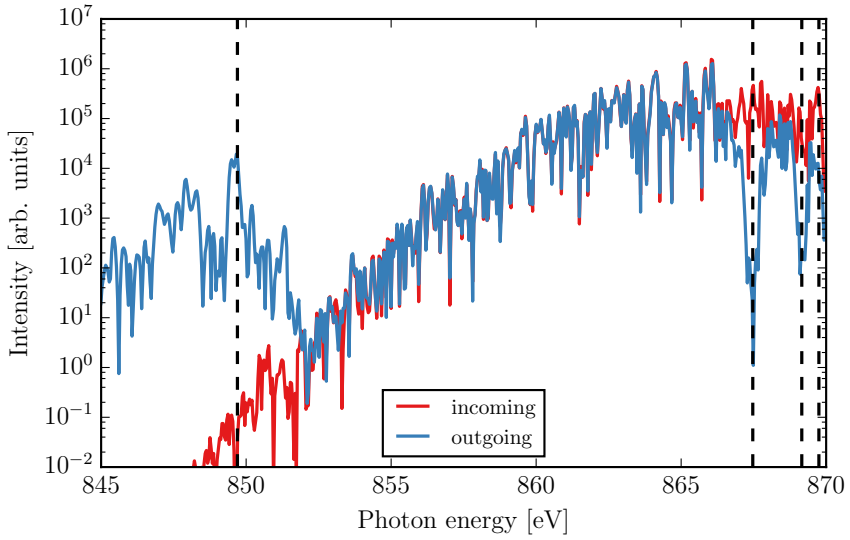

Figure 4.2.: Incoming and outgoing spectrum for a single SASE pulse with 866 eV central photon energy propagating through a 15 mm long neon gas target. Black dotted line on the left hand side marks the emission energy and the lines between 867 eV and 870 eV mark the excitation resonances.

4.3. Stimulated Raman scattering lineshape

When the bandwidth of the incoming radiation is smaller than the life-time width of the intermediate state x-ray Raman scattering displays a linear dispersion between the incoming radiation ω_{in} and the outgoing radiation ω_{out} [102, 163, 1]. The energy of

the outgoing radiation is thus determined by

$$\omega_{out} = \omega_{in} - \omega_{f0} \tag{4.32}$$

where ω_{f0} is the energy difference between the final state and the ground state. This relation implies that if the incoming radiation does not exactly match the resonance energy between ground and intermediate state ω_{i0} and is slightly detuned by Ω, the outgoing radiation is detuned from the intermediate to final state transition by the same value Ω, see Fig. 4.3. This effect was named "anomalous" dispersion because the frequency of the outgoing radiation follows the detuning of the incoming radiation. This relationship is only valid for a narrowband radiation source with a bandwidth which is less than the core-excited state lifetime.

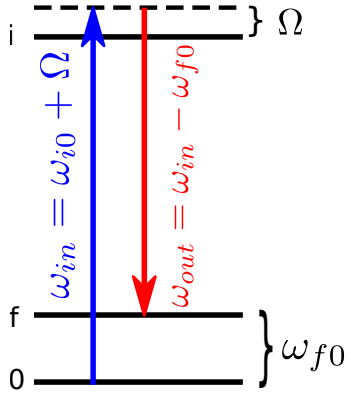

Figure 4.3.: Raman scattering for an incoming pulse $\omega_{in} = \omega i0 + \Omega$ slightly detuned from the resonance by Ω. The emission is detuned by the same value of Ω and the emission frequency is $\omega_{out} = \omega_{in} - \omega_{f0}$.

If the scattering process however is driven by a spiky and broadband SASE radiation source the situation is more complex. Due to the low spectral coherence of SASE radiation, it is possible to view the SASE spectrum as a sum of randomly phased and independent narrowband frequency components. This assumption makes it possible to use the linear dispersion relation for x-ray Raman scattering for a radiation source with an overall bandwidth which is much broader than the life-time width of the intermediate state. Each spectral spike in the incoming spectrum has a specific detuning from the resonance and the scattering process follows the anomalous linear dispersion. For a single SASE pulse and several resonances this yields a complex emission spectrum

with multiple frequency components. The spectral distribution and shape of the SASE pulse changes from shot to shot, resulting in different detunings from the resonances and hence different emission spectra. The process of x-ray Raman scattering with a

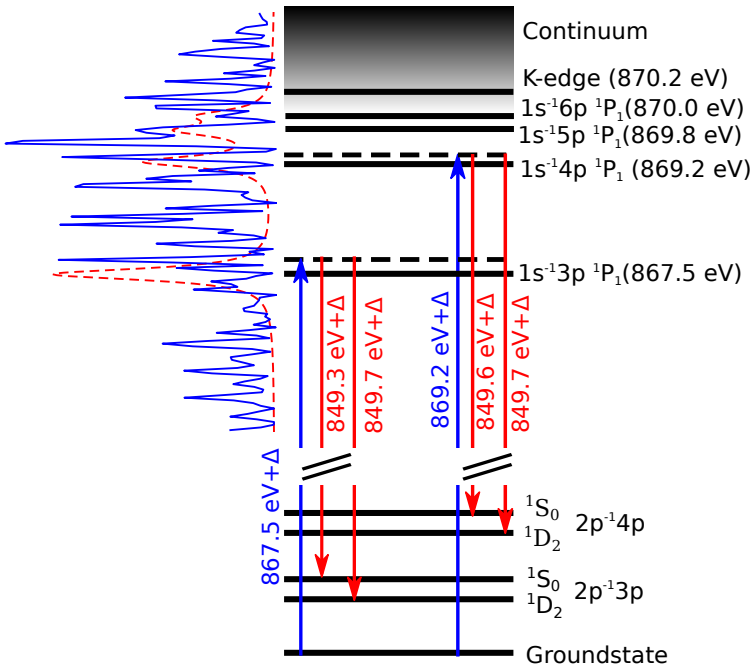

Figure 4.4.: Level scheme of neon for resonant x-ray Raman scattering. The SASE pulse (blue solid line) overlaps with the Rydberg series of the resonances below the neon K edge. The Lorentzian absorption profiles of the resonances are marked by the red dashed line. The strongest spectral spike close to those resonances is driving the scattering process.

broadband incoherence source is summarized in Fig. 4.4.

In the following this description of the scattering process is used to analyze the emission line shape for stimulated x-ray Raman scattering. The stimulated x-ray Raman scattering for the same pulse as in Fig. 4.2 is studied in more detail in Fig. 4.6. The figure depicts the temporal profile of the scattered radiation and the SASE pulse at the end of the medium along with their respective spectra. Since the incoming and the scattered radiation are contained in the single electric field envelope $\mathcal{E}(t)$, the two components have to be separated to represent their individual temporal profiles. The incoming and the scattered radiation can be separated in the frequency domain. To obtain a representation of the radiation in the frequency domain while retaining time

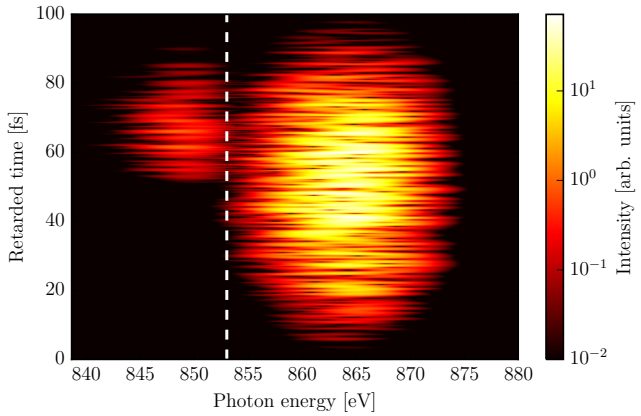

Figure 4.5.: Short-time Fourier transform of the electric field with a window function of 0.25 fs (FWHM). White dotted line separates the Raman scattered radiation from the SASE pump pulse.

domain information the short-time Fourier transform (STFT) is used. In the standard Fourier transform the time information is completely lost when transforming to the frequency domain. To maintain time information the electric field is multiplied with a window function w before transforming to the frequency domain

$$\mathcal{E}(\omega,\tau) = \int_{-\infty}^{\infty} w(t-\tau)\,\mathcal{E}(t)\,\mathrm{e}^{-i\omega t}dt\,. \tag{4.33}$$

The window function cuts out only a small part of the field in the time domain and is moved through the complete duration of the field to obtain the time information. A Gaussian was chosen for the window function with a duration 0.25 fs. There is a trade-off between time and frequency resolution. A long window function leads to a good frequency resolution but has a bad time resolution and the other way around for short window functions. The duration of the window function was set to the smallest value at which the incoming and scattered radiation can still be separated in the frequency domain to maintain a good time resolution. Fig 4.5 shows the short-time Fourier transform $\mathcal{E}(\omega,\tau)$ at the end of the medium. The scattered pulse and the SASE radiation can be clearly separated in the frequency domain. The temporal profile of both pulses in Fig. 4.6 is generated by integrating over the respective spectral region in Fig. 4.5.

The spectrum of the emitted radiation in Fig. 4.6c) shows three distinct peaks A,

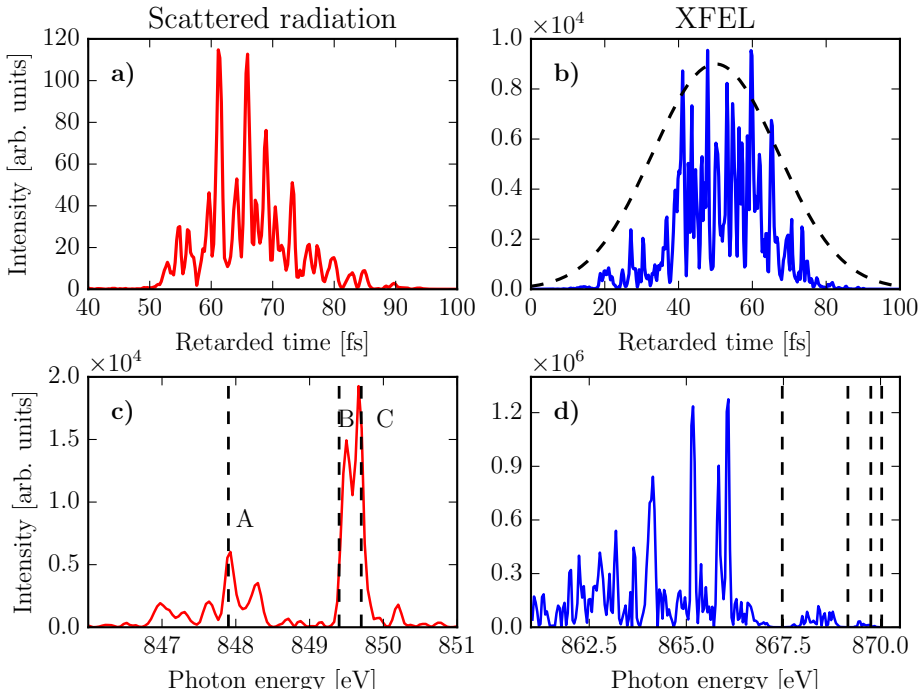

Figure 4.6.: Temporal profile of the scattered radiation a) and the SASE pulse b) at the end of the medium. Spectrum of the scattered radiation c) and the SASE pulse d). Dotted line in c) mark the emission peaks A at frequency $\omega_{1s^{-1}3p\to 2p^{-1}3p} - \Omega$ with a detuning of 1.4 eV, the transition B at $\omega_{1s^{-1}3p\to 2p^{-1}3p}$ and the transition C at $\omega_{1s^{-1}5p\to 2p^{-1}5p}$.

B, C with some additional spiky background. To understand this emission pattern it is helpful to look at an effective excitation cross section for the specific SASE pulse to see what scattering channels are accessible. The excitation cross section is defined as the product of the XFEL spectrum with the Lorentzian absorption profiles of the excitation resonances weighted with the dipole moment.

$$\sigma_{\text{excitation}}(\omega) = I_{\text{XFEL}}(\omega) * \sum_{i=3p}^{6p} z_{0i} \frac{\Gamma^2}{\Gamma^2 + (\omega - \omega_{i0})^2} \tag{4.34}$$

where z_{0i} is the dipole moment between the groundstate and the core-excited state i. The excitation cross section as a function of propagation distance is shown in Fig. 4.7a). From this plot it is possible to determine the leading spectral spikes in the scattering process and their detuning from the closest resonance. Fig. 4.7a) indicates that in the

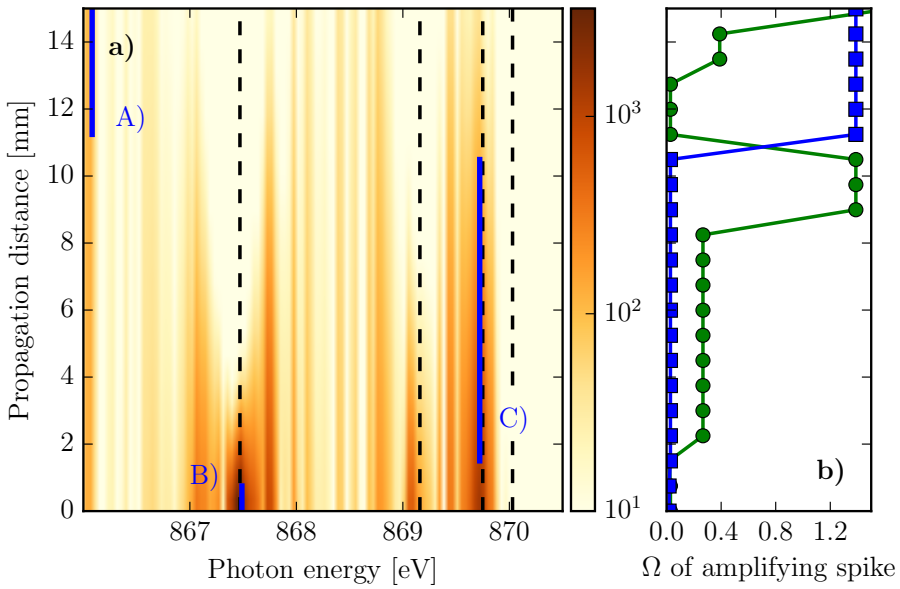

Figure 4.7.: a) Effective excitation cross section for the single SASE pulse from Fig. 4.2. The excitation cross section is determined by the SASE spectrum multiplied with the Lorentzian absorption profiles of the resonances weighted with the transition dipole moment. Black dotted lines mark the resonances and the blue line shows the position of the strongest scattering channel as a function of propagation distance. b) Detuning Ω of the strongest (blue) and second strongest (green) amplifying spike.

beginning of the medium two strong spectral spikes close to the 1s-3p and the 1s-5p resonance dominate the scattering process. The spikes have a respective detuning Ω of 20 meV and 28 meV and generated the two peaks B and C in the emission spectrum in Fig. 4.6a). These emission peaks are shifted by the same detuning from the emission transition. The peak B is detuned to higher energies while the peak C is detuned to lower energies for both the excitation and the emission. While propagating through the gas medium these two driving spectral spikes get absorbed and after around 11 mm of propagation the strongest spike is now A) at 866 eV. This spectral spike is detuned by 1.4 eV to the left of the 1s-3p resonance. This spectral spike generated the third peak A) in the emission spectrum in Fig. 4.6a) with the same detuning Ω of 1.4 eV from the $1s^{-1}3p \rightarrow 2p^{-1}3p$ transition. Fig. 4.7b) shows the detuning of the two strongest spikes driving the scattering process as a function of propagation distance. The detuning of the second strongest spike (green) has a value of 0.3 eV for propagation distances

between 2 mm and 8 mm and explains the peak in the emission to the right of peak A) in Fig. 4.6a). With this careful analysis of the incoming spectrum all the peaks in the emission spectrum can be identified.

The SASE pulses along with absorption and propagation lead to a rich structure in the emission spectrum of the scattered radiation. Multiple spikes with different individual detuning can contribute to the scattering process when propagating through the medium. The Raman scattering process is typically driven by around 5-10 spectral SASE spikes. Even tough each spectral spike from the SASE pulse itself can be considered coherent, the spectral spikes have a random phase with respect to each other. Driving the scattering process with multiple spikes with different phase results in Raman scattered pulses that are not transform limited. This is in contrast to the amplified spontaneous emission which are transform limited despite the incoherent pumping.

A broadband XFEL around the neon K edge can photo-ionize 1s electrons and also resonantly excite 1s electron to the unoccupied orbitals below the edge. This leads to stimulated K-α fluorescence and stimulated x-ray Raman scattering and it is important to differentiate between their emission line shapes. Fig. 4.8a) shows the ensemble averaged emission spectra for a scan of the central incoming XFEL photon energy around the K edge. The XFEL pump pulses consist of 2×10^{12} incoming photons in a 40 fs pulse duration (FWHM). The stimulated Raman scattering for incoming photons energies below the K edge (870.2 eV) has a much broader emission structure compared to the stimulated fluorescence for above edge excitation. The emission structure is around 2 eV wide and shows an additional emission structure at lower photon energies. This emission structure is stimulated Raman scattering with detuned resonant excitation. Due to the strong amplification the emission is saturated and partly reabsorbed around the $1s^{-1}3p\,^1P_1 \rightarrow 2p^{-1}3p\,^1S_0$ transition at 849.3 eV, see table 4.1. This makes it look like there are two separate emission peaks for excitations below 868 eV. Single shot emission spectra in Fig. 4.8c) reveal the great variation in line shape for resonant excitation. The emission line shows a stochastic shift in its main emission frequency from shot to shot. The individual spikes in the emission spectrum have a bandwidth of around 0.1 eV, corresponding to the spectral coherence of the SASE pulses. The shifts in the emission frequency reflect the stochastic nature of the SASE XFEL pulses and are the main feature to distinguish between x-ray Raman

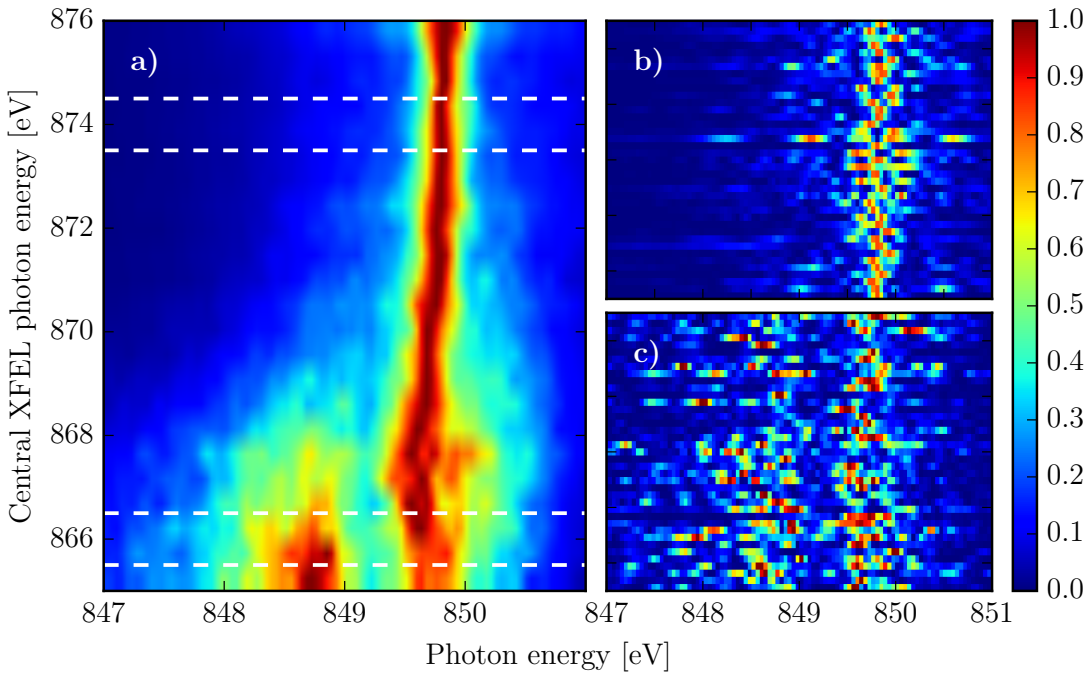

Figure 4.8.: a) Ensemble averaged emission spectra as a function of the incoming XFEL photon energy. The ensemble for each photon energy consists of 120 single shots. Each row in the figure is normalized by its maximum value. b) normalized single shot emission spectra with central XFEL energies between the white dotted line on the left (873.5 eV to 874.5 eV) and c) with incoming XFEL photon energies between 865.5 eV and 866.5 eV.

scattering and stimulated fluorescence. The single shot emission spectra for stimulated fluorescence in Fig. 4.8b) show a much more stable and reproducible emission pattern and the central emission frequency does not change from shot to shot. There is a variation in the emission linewidth that results from saturation broadening that differs from shot to shot.

4.4. Emission strength as a function of incoming photon energy

Fig. 4.9 shows the amplification of the scattering signal by stimulated x-ray Raman scattering along a 15 mm long gas medium. The figure displays the number of photons in the scattered field and the number of photons in the XFEL pulse below the K edge

as a function of propagation distance for two SASE ensembles with central photon energies of 866 eV and 867 eV. The SASE pulses for both ensembles consist of 1.5×10^{12} photons with a flat focus focus of radius 2 µm. The part of the XFEL pump pulse

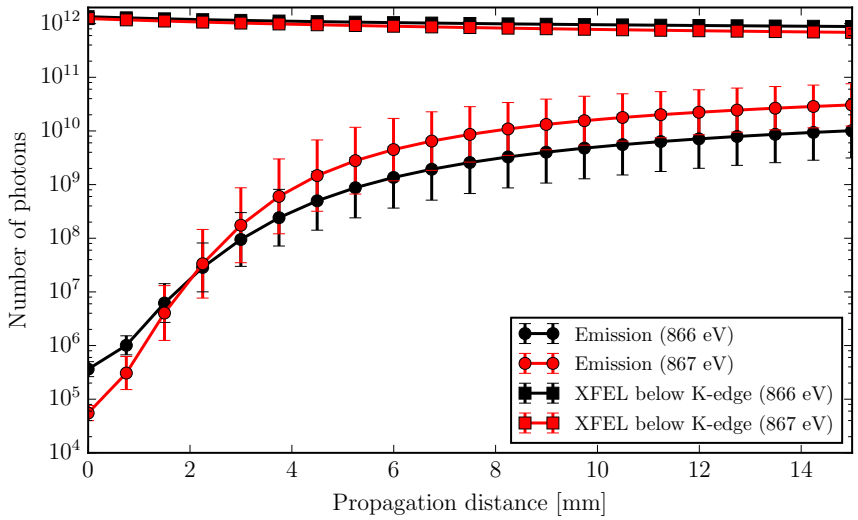

Figure 4.9.: Number of photons in the scattered and the XFEL pulse as a function of propagation distance for two SASE ensembles with different central photon energies of 866 eV (black lines) and 867 eV (red lines). Error bars show the standard deviation.

below the K edge gets only slightly attenuated by propagating through the medium. The narrow excitation resonances together with the fact that most the XFEL intensity is below the K edge for these central photon energies leads to a high transmission of the XFEL of around 50%. The spectral tail of the initial XFEL pulse provides on average 3×10^5 photons in the region between 847 eV and 852 eV for the SASE ensemble with 866 eV and 5×10^4 photons for the two SASE ensembles with 867 eV central energy. These initial photons seed the stimulation of x-ray Raman scattering in the forward direction. The spectral tail of the XFEL provides orders of magnitude more photons than the spontaneously scattered photons which yield approximately 100 photons in the entire interaction volume. The ensemble with the lower central photon energy provides more initial seed photons since it is closer to the emission transition around 849 eV. The gain for the Raman transition though is higher for the 867 eV ensemble because it has more intensity at the excitation resonances between 867 eV and the K edge. After going through an exponential gain region the amplification levels off

and the gain curve for the Raman scattered pulse flattens out after around 5 mm of propagation.

4.5. High resolution stimulated Raman scattering by covariance analysis

To obtain high resolution stimulated Raman scattering data from stochastic broadband SASE XFEL sources does not seem feasible. The scattered radiation has a multi-peak emission spectra with up to 2 eV bandwidth and a stochastic shift of the central emission frequency from shot to shot. In the following though it will be demonstrated that by statistical analysis a high spectral resolution of the scattering process can be achieved from a large ensemble of single-shot measurements.

Ideally a stimulated x-ray Raman experiment would be performed with a two color x-ray source with reproducible and stable pulses and a narrow spectral bandwidth. The one x-ray color would excite specific resonances and the other color would seed the emission on the intermediate to final state transition. Unfortunately there is currently no x-ray source that can produce narrowband two color x-ray pulses with the necessary intensity for stimulated x-ray Raman experiments.

In traditional resonant x-ray Raman spectroscopy a narrowband radiation source is scanned across the resonances to obtain high spectral resolution [100, 164]. The resolution in this case is limited by the bandwidth of the incoming radiation and the detector. X-ray Raman spectroscopy experiments are typically performed at Synchrotron radiation sources with a monochromator to limit the bandwidth of the incoming radiation. In the medium to hard x-ray region Si, Ge or diamond cystals are used to achieve an energy resolution of ≈ 1 eV or better. A challenge with traditional x-ray Raman spectroscopy based on spontaneous Raman scattering is to detect enough scattered photons, especially for dilute samples. In case of spontaneous scattering the photons are emitted in random directions in a solid angle of 4π. The detectors can typically only cover a very small solid angle, so most of the emitted photons cannot be detected. The great advantage of stimulated x-ray Raman scattering is that the radiation is emitted in forward direction with a very small divergence. So on top of the enhancement due to the stimulation it is also possible to detect all the scattered radiation in a very small solid angle. This advantage makes it worthwhile to consider

stimulated x-ray Raman scattering for spectroscopy experiments.

For stochastic SASE pulses with a bandwidth that is much larger than the typical width of core-excited resonances it is not possible to scan the individual resonances. The spectrum of the SASE pulse consists of many individual coherent spikes with an average width that is typically smaller than the resonance width. Since each spectrally narrow, coherent spike can drive the scattering process, the scanning of the resonances is performed by the broad bandwidth of the radiation. The challenge is to extract the scattering information from each spectral spike in the SASE pulse. Since the scattering information from every spike is accumulated in a single emission spectrum it is not possible to extract this information for a single-shot spectrum. It is however possible to extract high resolution information from a large ensemble of single-shot emission spectra by statistical analysis. The spiky structure of the SASE pulse is actually exploited in this case to obtain a resolution beyond the average bandwidth that is limited by the spectral coherence of the SASE source.

With the help of covariance analysis [165–167] it is possible to reveal the relationship between excitation photon energy and the emission photon energy. The result resembles high-resolution scattering data with a coherent narrowband x-ray source. This technique enables high resolution stimulated Raman scattering with SASE pulses and is demonstrated in the following for an ensemble of 6000 simulated single-shot spectra. The covariance in the outgoing spectrum between two photon energies ω_1 and ω_2 is defined by

$$\mathrm{Cov}(\omega_1, \omega_2) = < I(\omega_1)\, I(\omega_2) > - < I(\omega_1) >< I(\omega_2) >, \tag{4.35}$$

where the brackets <> denote the ensemble average. The covariance is a measure for the strength of the correlation between the two frequencies ω_1 and ω_2. The covariance is a useful quantity to detect the correlation between incoming frequency and the emission frequency in stimulated x-ray Raman scattering. It is important to note that the covariance can be calculated solely from the outgoing spectrum at the end of the medium. This is important for the practicability of the method, since in the experiment typically only the outgoing spectrum is measured and the initial incoming spectrum is unknown. Fig. 4.10 shows the calculated 2D covariance map, where the ω_1 axis can be interpreted as emission frequency and the ω_2 axis as excitation energy. The incoming XFEL photon energy was set to 867 eV with a pulse duration of 40 fs,

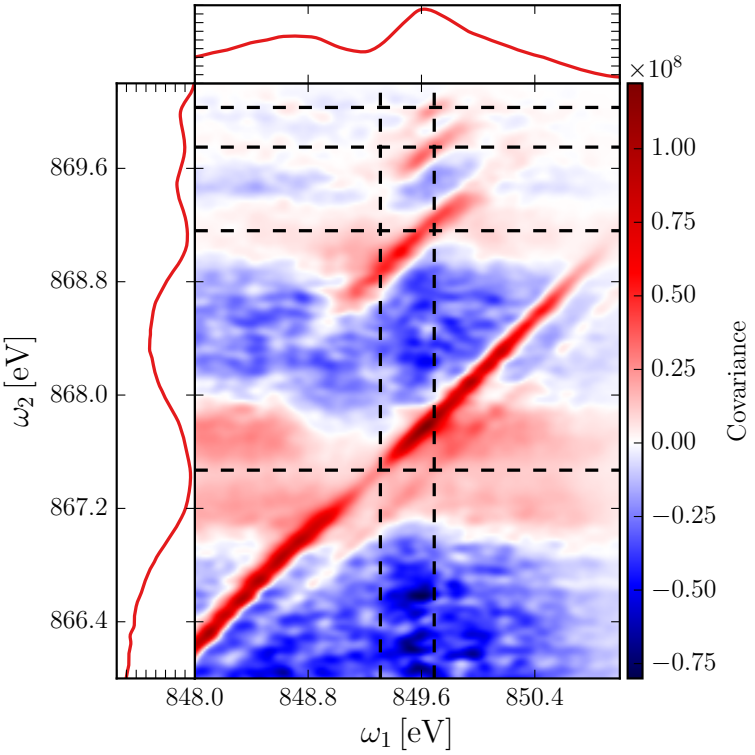

Figure 4.10.: Covariance map for an ensemble of 6000 single shots after 10 mm of propagation through the neon medium. The horizontal dashed lines mark the excitation resonances and the vertical lines mark the two strongest emission lines. The insets show the ensemble averaged intensity for the respective photon energy region.

resulting in a spectral coherence of 0.1 eV. The pulse duration determines the spectral coherence of the SASE pulses (average width of a spike in the SASE spectrum), see equation 2.36. The covariance map clearly shows the "anomalous" linear dispersion of the resonant scattering process. The scattering channels from the different excitation resonances 1s-{3p-6p} can easily be distinguished. For the 1s-3p resonance it is even possible to resolve the final state doublet $2p^{-1}3p\,{}^1S_0$ and $2p^{-1}3p\,{}^1D_2$ to obtain two separate emission lines. For the higher lying resonances the spacing of the final state doublet is smaller than the spectral resolution of 0.1 eV that is given by the spectral coherence, resulting in a single emission line. Due to the proximity of the central XFEL photon energy (867 eV) to the 1s-3p resonance (867.5 eV) this scattering channel is stronger than the channels with different intermediate state. The width of the

scattering pattern in the covariance maps are ≈ 0.1 eV, corresponding to the SASE XFEL spectral coherence.

The resolution of the scattering process with a stochastic and incoherent radiation source is thus determined by the spectral coherence of the source instead of the overall spectral source bandwidth. By increasing the SASE pulse duration the spectral coherence can be further decreased to yield an increase in spectral resolution. To

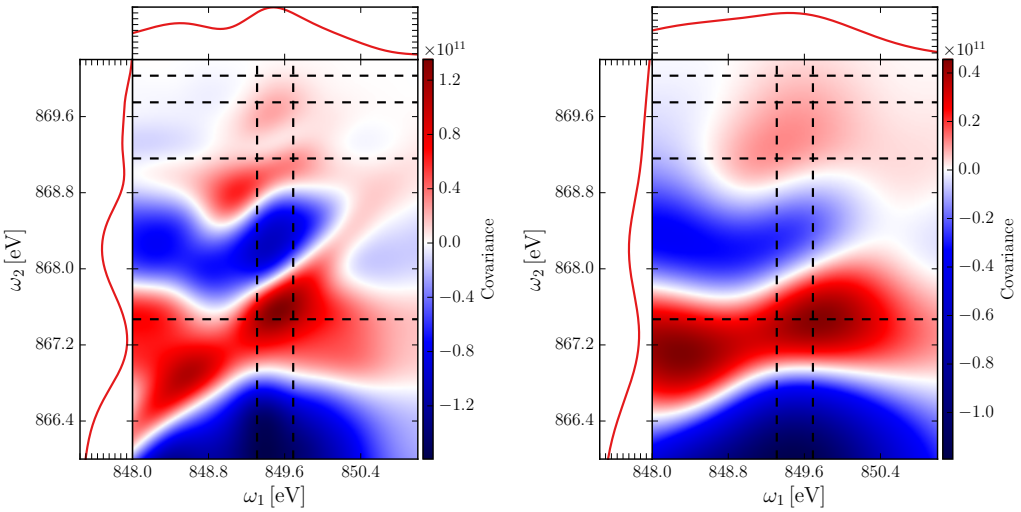

Figure 4.11.: Same covariance map as in Fig. 4.10 but the spectra were convoluted with a Gaussian function of 0.4 eV (FWHM) for the left figure and 1 eV (FWHM) for the right figure.

account for the limited resolution of the spectrometer in an experiment, the covariance map for the same ensemble is depicted in Fig. 4.11 where the single-shot spectra have been convoluted by a Gaussian function. In the covariance map on the left, where a Gaussian with 0.4 eV FWHM was used, the scattering features are washed out quite a bit. It is still possible to resolve the 1s-3p and the 1s-4p resonance but the higher lying resonances overlap and cannot the separated anymore. For the right covariance map, convoluted with a 1 eV FWHM Gaussian, the spectral resolution decreases even further. Only the 1s-3p resonance is clearly visible while all other resonances overlap and result in a single broad feature.

These covariance maps only work for a well defined average central XFEL photon energy. For a realistic SASE source there is also a stochastic shift of the central emission photon energy from shot to shot. If this jittering of the central frequency is taken into

account the anomalous dispersion features in the covariance map vanish, see Fig. 4.12. A possible approach to retain the spectral resolution despite the shift of the central

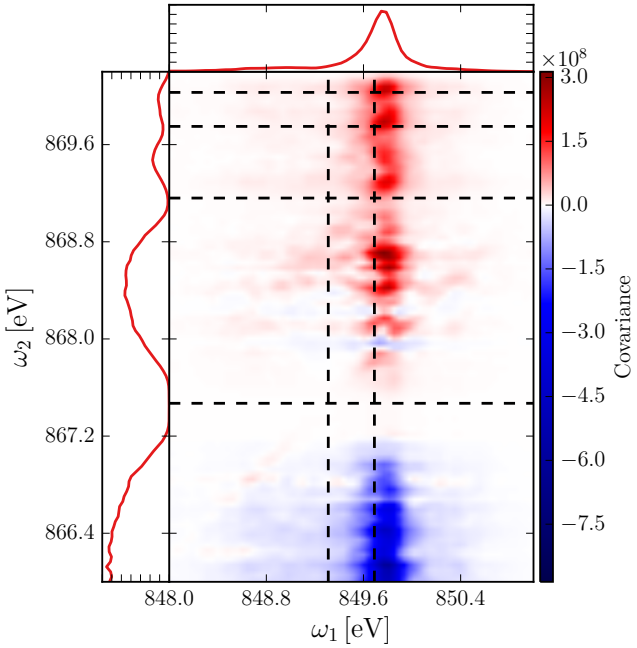

Figure 4.12.: Covariance map for a SASE ensemble with 867 eV central photon energy including a jitter of the central photon energy of ± 3 eV.

frequency is to use partial covariance mapping [167] instead of calculating a single covariance map over the whole ensemble. To calculate the partial covariance the central photon energies are binned into small intervals and the covariance for each interval is calculated separately and the results are then combined into a single covariance map.

Part II.

Experimental results

Chapter 5

Experimental demonstration of stimulated x-ray Raman scattering

This thesis includes results from two experimental campaigns that were carried out at the Linac Coherent Light Source (LCLS) at the SLAC National Accelerator Laboratory in Menlo Park, California. Both experiments were performed at the Atomic, Molecular and Optical (AMO) science instrumentation at LCLS [168]. The beamline provides a High-field Physics End-station to study the fundamental interaction of short and intense x-ray pulses with atoms and molecules. The available photon energy range at this End-station covers the soft x-ray region up to around 2 keV photon energy with at best a 1-2 µm focus at the interaction region. The goal of the first experimental campaign was to demonstrate stimulated x-ray Raman scattering in neon by resonant excitation with an XFEL below the K edge. In a second experimental campaign the stimulated x-ray Raman scattering in neon was reproduced with a higher spectral resolution.

5.1. Experimental Setup

The LCLS beam was focused down to spot sizes of $\approx$ 2 µm using Kirkpatrick-Baez (KB) focusing optics [169, 170]. The KB optics is a pair of curved mirrors in grazing incidence. The second mirror is placed after the first mirror at a right angle. One of the mirrors is horizontally deflecting while the other one is vertically deflecting to focus the x-rays to a point. The use of two curved mirrors placed after each other avoids the strong aberration effects one gets from using a single concave mirror [169]. The mirrors are made from a silicon substrate with a boron carbide (B_4C) reflective coating. The

mirror surface has to be extremely smooth with very low surface roughness to reflect the x-rays without scattering. The x-rays were focused into the 10 mm long gas cell

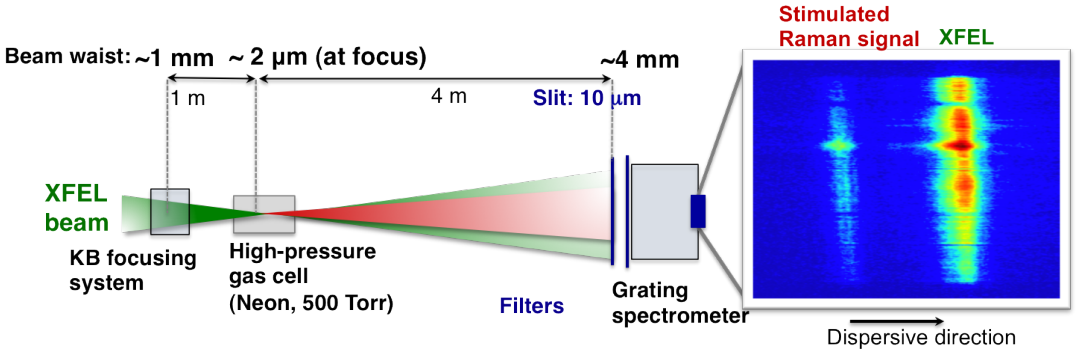

Figure 5.1.: Experimental setup.

that was embedded into the main vacuum chamber. The gas cell was filled with neon at a pressure of around 500 Torr. The gas cell was differentially pumped to limit the pressure in the main vacuum chamber. This means that there is an additional volume at both ends of the gas cell that is separated from the main vacuum chamber and the gas cell by thin Kapton foil. Kapton is a heat resistant and very durable plastic. These additional volumes are directly connected to vacuum pumps. This two step pumping process reduces the pressure gradient between the different stages. This allows to have a pressure of 500 Torr (666 mbar) in the gas cell and maintain a pressure of below 10^{-6} mbar in the main chamber. The focused XFEL pulses were used to drill holes in all four Kapton foils to allow the XFEL to pass through the gas cell. The stimulated x-ray emission has a similar spatial divergence as the XFEL pulse and also passes through the same exit holes in the Kapton foils. The emitted x-ray and the transmitted XFEL were detected in forward direction with a flat-field grazing incidence spectrograph.

In the first experiment a Princeton Instruments PIXIS-XO CCD camera was used to record the x-ray radiation with 2048 × 2048 pixels and 16 bit resolution. The Princeton Instruments camera had a very low readout speed and the repetition rate was below 1 Hz. For the second experiment a Andor Newton SO DO940P-BN with 2048 × 512 pixels with a pixel size of 13.5 × 13.5 µm was used. This CCD has a faster read-out rate compared to the PIXIS and can read full single-shot images at a maximum rate of 2 Hz. The read-out rate can be further increased by binning along the spatial resolution. The binning results in a reduced spatial resolution which can also lead to a reduction

in spectral resolution if the spectral lines are not vertical and have to be corrected afterwards, see Fig.5.2. Another possibility to increase the read-out rate is to crop the image and read out only a smaller part of the CCD detector if the signal does not cover the whole detector.

For stimulated x-ray emission and stimulated x-ray Raman scattering, single-shot spectra have to be recorded. The repetition rate for the experiment is limited by the read-out rate of the CCD detector. The 2D CCD detectors have a long read-out time of around 1 second, corresponding to a repetition rate of only 1 Hz. Integrating over several shots is not very interesting because it averages out the frequency dependent features that are fundamental to interpret Raman scattering measurements. Integrating over several 1000 shots is useful though in the initial stage of the experiment when trying to find and optimize the signal. When integrating over several LCLS pulses, one is not limited by the read-out rate of the CCD detector and can make use of the full LCLS repetition rate of 120 Hz. This enhances the signal and makes it easier to find the initial signal to start optimizing the experimental setup.

The low repetition rate makes it difficult to collect a large amount of single shot data. To interpret the results from RIXS measurement with incoherence SASE radiation a large amount of single shots are necessary to perform statistical analysis. An increase in read-out rate of the CCD detector would allow to collect more single shot data during the very limited beam time at big facilities like the LCLS. One possibility to increase the read-out rate of the detector is to bin rows in the spatial direction. This means that not every row is read out individually but the camera internally sums over several rows to increase the read-out rate. This results in a loss of spatial resolution which does not seam important, but it directly influences the spectral resolution as well. Due to misalignment of the spectrometer the dispersive axis is not completely horizontal and the spectral lines are therefore not completely vertical, see Fig. 5.2. This means that the spatial resolution directly influences the spectral resolution. This tilt error can be corrected during the analysis process by rotating the recorded 2D images to obtain vertical spectral lines. This correction though depends on the resolution of the spatial axis. A decrease in resolution for this axis by binning therefore leads to a reduction of spectral resolution as well. So increasing the read out rate by spatial binning sacrifices spectral resolution.

The other possibility is to use faster CCD detectors. The number of total pixels

and the size of the individual pixel have a large influence on the read-out time. So by choosing less total pixels or bigger pixel size the repetition rate can be enhanced by again sacrificing resolution. There is a lot of current development to build faster x-ray detectors [171–173], driven by the requirements of new XFEL radiation sources. The European XFEL for example will have a repetition rate of up to 27 kHz.

5.2. Data analysis

All of the data recorded by the LCLS data acquisition system is stored in xtc files for offline analysis. This binary file format can be read by one of the LCLS data analysis frameworks. The most common framework for analyzing the xtc files is psana. The psana framework has a C++ as well as a python interface, which makes it very accessible and easy to use. LCLS also provides automatic translation of the xtc files to the more common HDF5 file format. The HDF5 file format is a versatile file format to store large amounts of complex data objects. HDF5 has support for many languages and platforms and can also be read directly by MATLAB.

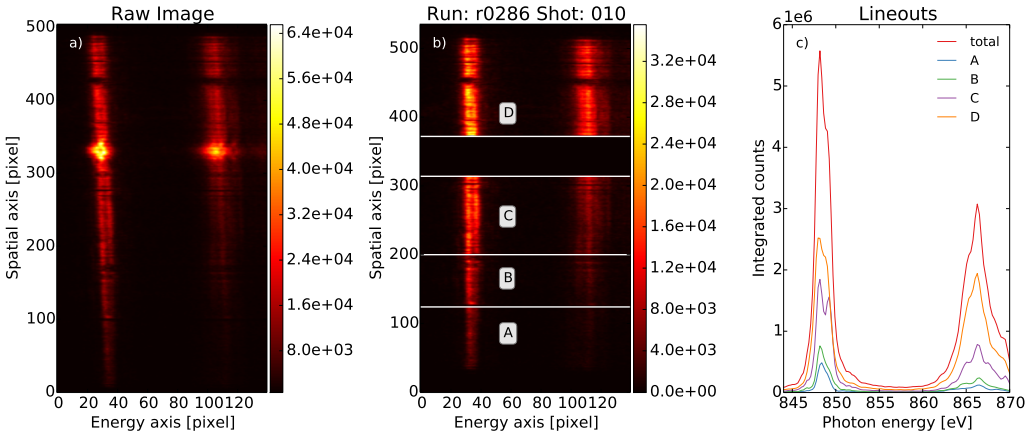

Figure 5.2.: Steps in the data analysis to produce spectra from the recorded 2D images. Single-shot measurement from the first experiment with a central photon energy of 872 eV and 1.3 mJ pulse energy. a) shows the measured raw 2D image. b) shows 2D image with subtraction of the background, removal of the saturated area and tilt correction. The spatial region is separated into regions with different intensity A-D by the white horizontal lines. c) shows the spectra by summing over the corresponding spatial part of the image in b).

To analyze the large amount of recorded LCLS data I extracted the necessary

information from the xtc files using psana and storing the data in HDF5 files. This has to be done directly on the LCLS computing cluster to have access to the LCLS psana framework. The generated HDF5 files were then copied to our local computers for further analysis. It is much easier to analyze the data on a local computer, especially for interactive visualization. The HDF5 files include the raw 2D detector image, the electron beam kinetic energy and the x-ray pulse energy measurements from the gas detector.

There are several analysis steps that have to be performed to turn the raw 2D images into spectra. The different steps are depicted in Fig. 5.2. The plot a) on the left shows the raw 2D data without any modifications. The horizontal axis is the dispersive direction and displays the intensity as a function of x-ray wavelength. The vertical axis represents the spatial profile of the x-ray beam. The image clearly shows two distinct lines with the photon energy increasing going from left to right. The left line is the amplified x-ray emission from neon and the right line is the transmitted LCLS beam. Both lines are not vertical but are titled. This tilt is an artifact of the alignment of the grating spectrometer. This causes the dispersive direction to be not completely horizontal at the camera. This tilt can be corrected by rotating the images clockwise by 0.87 degrees to make the lines vertical. The angle was chosen to give to the minimal spectral bandwidth for the stimulated emission line. This tilt is only a first order effect but there are higher order effects that cause the spectral lines to be curved rather than straight lines. These higher order effects are much more difficult to correct and require a detailed calibration of the spectrometer to obtain its full spectral resolution during the data analysis process. These higher order effects were not important for this experiment due to the limited spectral resolution and were therefore neglected. The higher order effects might have to be taken into consideration when going for a very high resolution below 0.1 eV. The corrected image with the tilt removed is depicted in Fig. 5.2b). The background of the CCD detector was also removed by subtracting a reference background image. The background image was measured without any x-ray exposure to capture only the camera noise floor. The bright spots in Fig. 5.2a) in both lines between spatial pixel 314 and 372 come from a hole in the filter in front of the camera. These parts of the image are saturated, meaning that the intensity value for those pixels is $2^{16} = 65536$, which is the maximum value for a detector with 16 bit resolution. The problem with these values is that the real intensity could be higher

but the CCD camera was not able to resolve it. Another problem is that if too many electrons are generated in one pixel element they can migrate to neighboring pixels and influence their intensity value as well. Those values thus cannot be considered accurate and the saturated areas in the image were set to zero. The spatial region of the image was further separated into regions with different intensities. This was done to evaluate if different parts of the beam with different intensities have varying spectra. The final step in generating spectra from the recorded images is to sum over the spatial region in the corrected image to generate spectral lineouts. The lineouts for the corresponding spatial regions are depicted in Fig. 5.2c) along with the total lineout over the complete spatial axis (still excluding the saturated region).

5.2.1. Determination of the central XFEL photon energy

When scanning the XFEL pulse around the K-edge of neon it is important to know its central photon energy. There is no way to directly determine the central photon of the XFEL pulse, because only the transmitted pulse after the gas cell was measured. It was not possible in this experimental setup to measure the incoming XFEL before going through the gas cell as well. Fortunately there is a direct relationship between the kinetic energy of the electron beam and the central XFEL photon energy. The kinetic energy of the electron beam is recorded for every single shot and is available in the xtc data files.

To determine the relationship between the electron beam kinetic energy and the central XFEL photon energy single-shot XFEL spectra were recorded without any gas in the gas cell. In the case of an empty gas cell the recorded spectra correspond to the incoming XFEL. The XFEL pulse just travels through vacuum and its spectrum is not altered by absorption or emission. From this the central photon energy can be determined by finding the position of the maximum peak in the recorded spectrum. The spectrometer has to be calibrated to convert the position of the maximum peak from pixel number to the actual central XFEL photon energy. Fig. 5.3 depicts the electron beam kinetic energy versus the calibrated central photon energy for a collection of recorded single-shot spectra. The plot shows an excellent linear relationship between the electron beam kinetic energy E_{ebeam} and the measured central XFEL photon energy

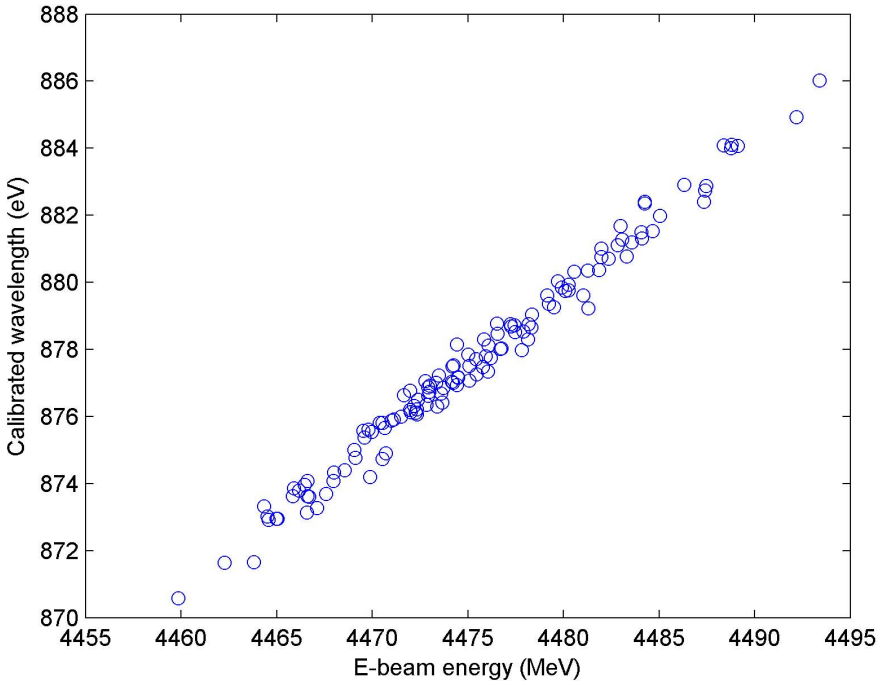

Figure 5.3.: Calibration of the central XFEL photon energy.

ω_{in}. Performing a linear regression on this data yields

$$\omega_{in}\,[\mathrm{eV}] = 0.4506 \times E_{\mathrm{ebeam}}\,[\mathrm{MeV}] - 1139.9\,[\mathrm{eV}]. \tag{5.1}$$

This is a convenient and easy method to get a very good estimation of the central XFEL photon energy without detecting the incoming XFEL spectrum. One only has to record a series of single-shot XFEL spectra with an empty gas cell. The data analysis and regression can be performed offline after the experiment.

5.2.2. Convert CCD counts to number of photons

To obtain the number of x-ray photons in the stimulated neon emission line and the transmitted XFEL pulse, the counts of the CCD camera have to be converted to photon numbers. The conversion depends on the instrument throughput and the gain settings of the CCD camera. The following relationship for the number of photons per count

on the CCD detector was used

$$n_{\mathrm{ph}}\left[\frac{\text{photons}}{\text{count}}\right] = \frac{3.65\left[\frac{\text{eV}}{\text{electron}}\right]\cdot g\left[\frac{\text{electrons}}{\text{count}}\right]}{\mathrm{h}\nu\,[\text{eV}]\;T_{\mathrm{instr}}\,T_{\mathrm{filter}}\,Q}\,. \tag{5.2}$$

Where $g = 0.94$ is the gain, i.e. the number of electrons per count (determined from the gain setting of the CCD camera). The Princeton Instruments PIXIS-XO CCD camera was operated at the 2 MHz readout rate in the low-noise mode. T_{instr} is the throughput of the spectrograph, T_{filter} is the transmission of the filters in front of the spectrometer and $Q = 0.825$ is the quantum efficiency of the CCD detector. The throughput of the spectrograph is determined by the transmission of the slit T_{slit}, the reflectivity of the two focusing mirrors (0.59^2) and the reflectivity of the grating (0.043). T_{slit} was determined by estimating the size of the beam on the plane of the slit from the intensity distribution of the line in the direction of the slit. The following filters were used in front of the CCD detector to attenuate the x-ray beam

Filter name	**Filter composition**
A2	1 µm Al / 0.65 µm Cu
A3	2 µm Al
B1	1.12 µm Al / 1.43 µm Ge
B3	4 µm Al
C1	0.2 µm Al
C2	0.3 µm Al / 1.5 µm Sm / 0.2 µm Al

Table 5.1.: Table of filter acronyms and their corresponding material composition.

The frequency dependent transmission coefficients for each material was taken from [174]. The transmissions for each material were multiplied to get the total transmission of each filter. The transmission curves for the filters are shown in Fig. 5.4. The sharp drop off in transmission for filter A2 at 933 eV is due to the Copper L_3 edge.

5.2.3. Online data analysis at LCLS

LCLS provides a graphical analysis tool (AMI) which can be used for online monitoring during the experiment. Online in this case means in real time and the data is available as soon as it is recorded by the detectors. This tool has access to every detector that is connected to the LCLS data acquisition system (DAQ). AMI is a general purpose analysis tool and can perform operations like generating spectra from 2D detector

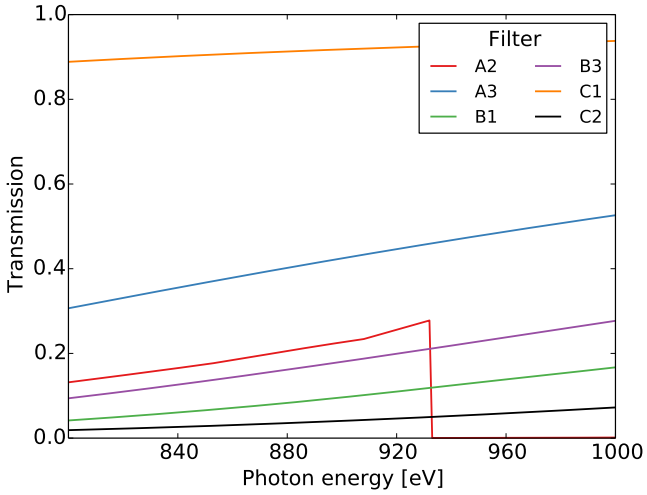

Figure 5.4.: Transmission as a function of photon energy for filters in table 5.1.

images by summing over the spatial dimension. It is a quite complex software that is maintained by the LCLS DAQ group.

To get a real time high spectral resolution feedback from the experiment, some additional specialized features are required. One of these features is image tilt correction. The spectral lines on the detector are not completely vertical lines but have some tilt, see Fig. 5.2. This tilt can be corrected by rotating the image until the spectral lines are vertical. This was especially important for optimizing the spectrometer using amplified K-α emission from neon. The narrow K-α line had a width of only several pixels on the detector, while the error due to the tilted images was on the same order. To get accurate estimates for the line width, tilt corrections are vital and they also have to be in real time to provide feedback for tuning the spectrometer during the experiment. Another important feature is the fitting of spectral lines to determine their bandwidth.

It is rather difficult to add these specialized features to the LCLS AMI general purpose analysis tool. To have a flexible online monitoring tool which fulfills the above requirements I developed an online monitoring software to read and analyze data in real time from the LCLS DAQ. LCLS provides a convenient way to obtain real time data from the DAQ monitoring nodes through a shared memory interface. The data can be read from shared memory using the LCLS analysis framework psana. This framework is also used for offline analysis of LCLS data, making most of the code reusable for offline

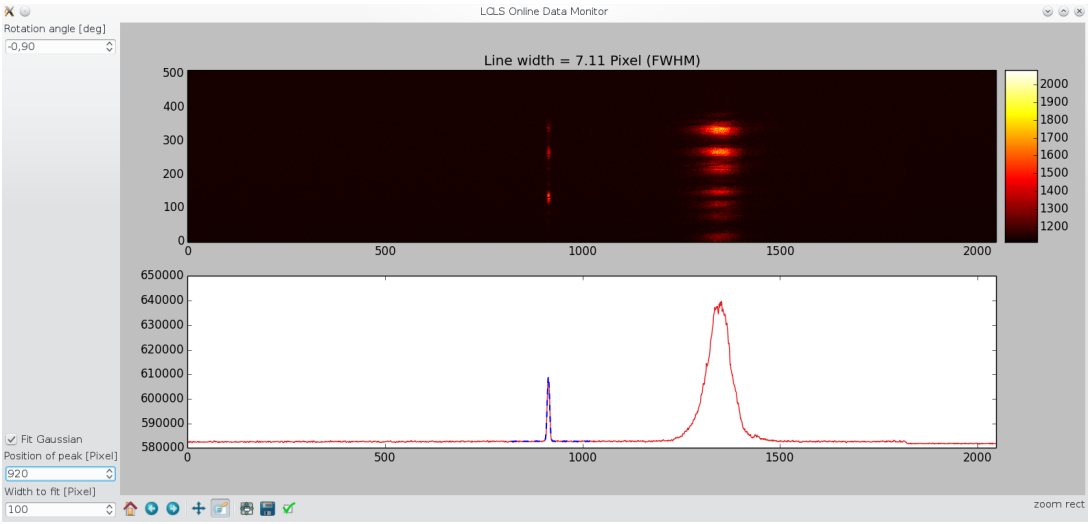

Figure 5.5.: Screenshot of the developed online monitoring program. Showing the tilt corrected 2D image from the detector and the corresponding spectrum with a Gaussian fit (blue dotted line) to determine the line width.

analysis as well. The tool was developed using a client server architecture. The server collects the data from the DAQ monitoring nodes and sends it to the client, which does the analysis. Separating the data collection from the analysis and visualization makes the software very flexible and easy to adapt. The server also has to be run on the DAQ monitoring mode, while the client can be run on any computer that can connect to the DAQ monitoring via the network. Fig. 5.5 shows a screen shot of the program interface. The program displays the 2D detector image and can correct the image tilt by rotating the image to get vertical lines. The lower part of the screen shot shows the corresponding spectrum by summing over the spatial dimension. The program can fit a Gaussian function to parts of the spectrum to determine line widths and displays the width (FWHM) at the top. The column on the left hand side has input field to change the rotation angle, enable fitting and adapt fitting parameters. The approximate peak position and the number of pixels around the peak position to be considered for the fit have to be set.

In the following I will give more detail on the architecture and show the important parts of the code for data acquisition. The online monitoring tool was written in the programming language Python. Python is a dynamic interpreted programming language. The execution of Python code itself is rather slow but due to the fast external

libraries it is fast enough to analyze and plot the data in real time for repetition rates of up to 10 Hz. The following code listing shows the code for the server application. The server reads in new data from the LCLS DAQ as soon as it arrives and passes it on to the client via the ZeroMQ messaging library. The server always has to be

```
import zmq
import psana
import numpy as np

context = zmq.Context()
socket = context.socket(zmq.PUB)
socket.bind("tcp://*:12322")

camera_src = psana.Source('DetInfo(AmoEndstation.0:Andor.0)')
data_source = psana.DataSource('shmem=0_1_AMO.0').events()

for evt in data_source:
    frame = evt.get(psana.Andor.FrameV1, camera_src)
    if frame:
        img = frame.data()
        buff = np.getbuffer(img)
        socket.send(buff)
```

Listing 1: Server that reads in detector images and sends them to the client for processing.

run on one of the DAQ monitoring nodes (hostnames "daq-amo-mon*", where * is the number of the monitoring node) to have access to the shared memory interface. The server loops over the *data_source* variable which contains the events and is updated as soon as a new event arrives. It then reads in the detector data using the LCLS psana framework. The detector is specified by the variable *camera_src* which holds the access information of the camera and is specific for each detector. In this case the Andor CCD camera at the AMO endstation was used. The variable has to be adapted if other detectors or endstations are used. If the camera frame exists the raw detector data is extracted and sent to the client for further processing and visualization.

The following listing shows the part of the online client for reading in the detector data. The client connects to the server described in the variable *hostname* to port 12322 and subscribes to any incoming messages. It then waits for data to arrive at the

```
import zmq
import numpy as np

hostname = 'tcp://daq-amo-mon01'
context = zmq.Context()
socket = context.socket(zmq.SUB)
socket.connect(hostname + ':12322')
socket.setsockopt(zmq.SUBSCRIBE, '')

while True:
    buff = socket.recv()
    img = np.frombuffer(buff, np.uint16).reshape(512, 2048)
    '''
      processing and visualization of the data comes here
    '''
```

Listing 2: Code for the online client to read in data that comes from the server application.

socket and stores the message into a buffer. The raw buffer is then converted to a 2D image of unsigned 16 bit integers with dimension 512 × 2048. This detector image can now be processed and visualized.

5.3. Results

Fig. 5.6 shows the spatial profile of the transmitted LCLS pulse and the atomic x-ray laser pulse for a single shot. The sharp cutoff at the edges come from the slit in front of the CCD detector. Both spatial profiles match almost perfectly and demonstrate that the spatial divergence of the stimulated emission beam matches the divergence of the LCLS beam.

To determine the emission line shape a large ensemble of single-shot spectra with varying incoming photon energy was recorded. Fig. 5.7 shows the raw 2D image along with the generated spectra for two shots out of the ensemble. Fig. 5.8 displays the collection of single-shot spectra sorted by the incoming central photon energy. The plot contains a total of 956 single-shots, with 222 shots with incoming photon energy below the K edge. The dynamic range (ratio between maximum and minimum pixel intensity value) is 1.5×10^4. The plot consists of shots from multiple runs where different filter

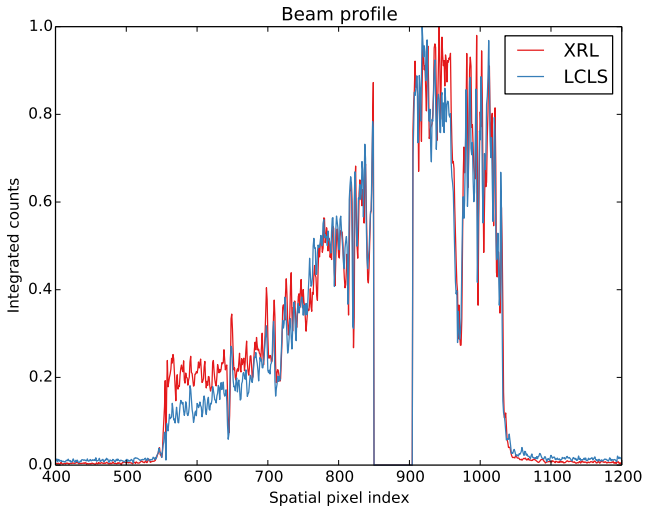

Figure 5.6.: Spatial beam profile of the XFEL and the stimulated emission beam.

combinations were used. To account for the different filters all shots were normalized by their respective filter transmission. The central photon energy of the incoming XFEL pulse was determined from the electron beam kinetic energy, see section 5.2.1. The transmitted XFEL pulses follow a diagonal line and show a strong attenuation for recorded photon energies above the 1s-3p resonance and the K edge due to absorption. The stimulated emission appears as a vertical structure at a recorded photon energy of around 850 eV. The broad XFEL bandwidth of around 7 eV FWHM covers the Rydberg series below the K edge as well as the continuum. This makes it difficult to distinguish the stimulated x-ray Raman scattering from the stimulated K-α emission from above edge excitation. There is no pronounced variation of the scattering intensity as a function of the incoming photon energy for shots below the K edge.

To study the emission line shape in more detail, Fig. 5.9a) shows the normalized emission line as a function of the XFEL photon energy. All shots were normalized by their maximum spectral intensity in order to identify the central emission frequency from every shot. The plot only contains shots that showed a clear emission line and all other shots were removed. This was done by going through all the spectra to confirm that they have a peak in the emission region which is at least 3 times stronger than the background. The shots below the K edge (870.2 eV) show a much larger variation in the central emission energy with a standard deviation of $\pm$ 0.4 eV compared to

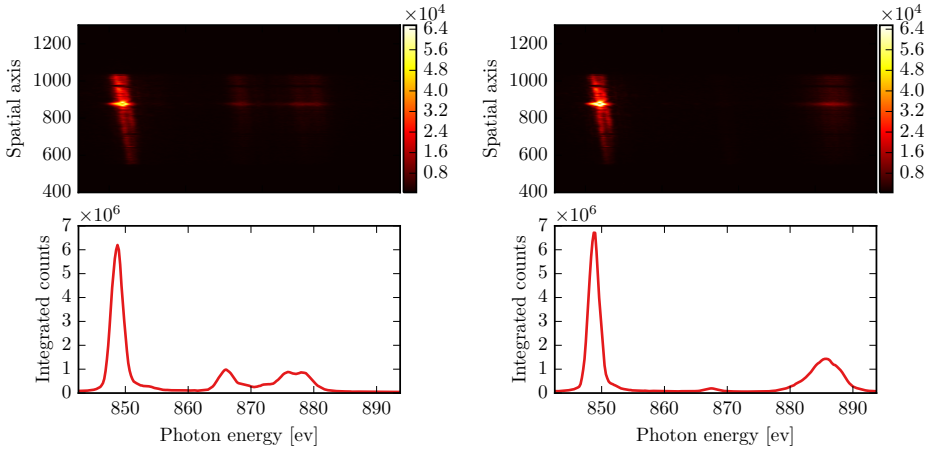

Figure 5.7.: Two raw single shot images from the first experiment. The spectrum below the images is generated by the procedure outlined in section 5.2.

the shots above the K edge with a standard deviation of ± 0.1 eV. This stochastic shift is a clear indication of stimulated x-ray Raman scattering with SASE pulses and differentiates the scattering line shape from the K-α emission above the edge. The emission spectrum and the stochastic shift of the Raman scattering line shape was discussed in section 4.3. The stimulated K-α emission has a fixed emission frequency that is independent of the incoming photon energy and the specific spectrum of the SASE pulse. To support this interpretation of the emission line shape, Fig. 5.9b) shows simulated single shot emission spectra, obtained from the theory presented in section 4. The theory includes resonant excitation as well as photo-ionization to describe both emission processes in a single model. The simulated spectra were convoluted with a Gaussian with 1 eV width to match the resolution of the spectrometer and to allow a comparison between the calculated and the measured line shape. The XFEL pulse parameters for the simulations were chosen to match the experimental values: 2×10^{12} photons, 40 fs pulse duration, 2 µm focal radius and 7 eV spectral bandwidth. The simulated emission spectra display the same features as the experimental data. They show the same stochastic shift of the emission line for shots below the K edge and the reproducible stable line shape for shots above the edge. The variation in linewidth for shots above the K edge is a result of saturation broadening.

To demonstrate the exponential amplification of the stimulated emission its signal strength is studied as a function of the incoming XFEL pulse energy. The stimulated

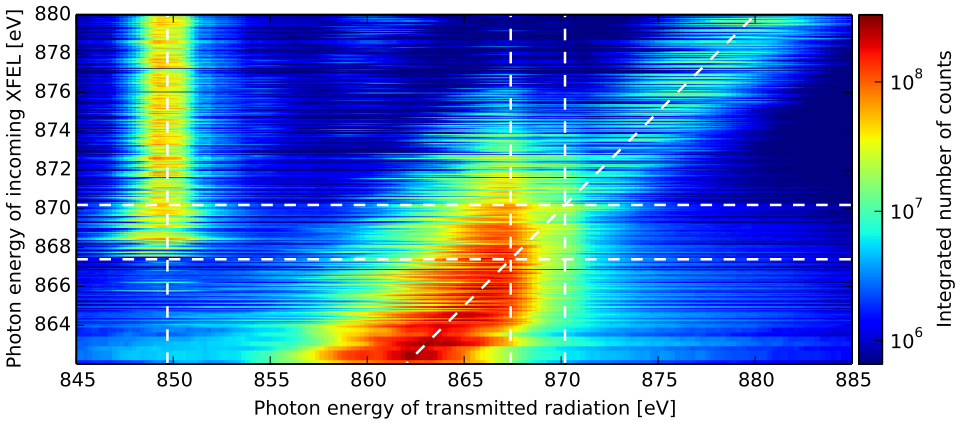

Figure 5.8.: Single-shot spectra assembled by incoming XFEL photon energy. The diagonal white dashed line follows the transmitted XFEL beam. The vertical dashed lines at 849.7 eV marks the emission line. The $1s^{-1} - 3p$ resonance at 867.5 eV and the neon K edge at 870.2 eV are marked by horizontal and vertical dashed lines.

Raman scattering and the stimulated K-α fluorescence are plotted separately depending on the incoming XFEL photon energy. The incoming pulse energy was varied by using a gas attenuator to absorb a part of the x-rays and reduce the pulse energy. The factor of attenuation can be varied by the gas pressure in the attenuator.

Fig. 5.10 shows the number of photons in the emission for pumping above the K edge (red points) and below the edge (blue points) along with theoretical values obtained from the simulation. The pulse energy values are measured by gas detectors at LCLS that are placed in the beamline before the focusing optics. This means the measured pulse energies values have to be rescaled with the transmission of the optics to correspond to the actual pulse energy on target. A beamline transmission of 18 % was assumed to get a good overlap between the measured values and theory. Varying the incoming pulse energy from 0.08 mJ to 0.35 mJ results in an increase of the emission by four orders of magnitude. This strong exponential dependence on the incoming pulse energy is a clear indication for amplification by stimulated emission. For shots with incoming XFEL photon energy above 870.2 eV the emission is dominated by stimulated K-α fluorescence. The stimulated K-α emission shows exponential gain followed by saturation for pulse energies above 0.16 mJ. The theoretical calculations with central photon energy of 877 eV (average incoming photon energy of shots above the edge) match the experimental data very well. The only free parameter was the transmission

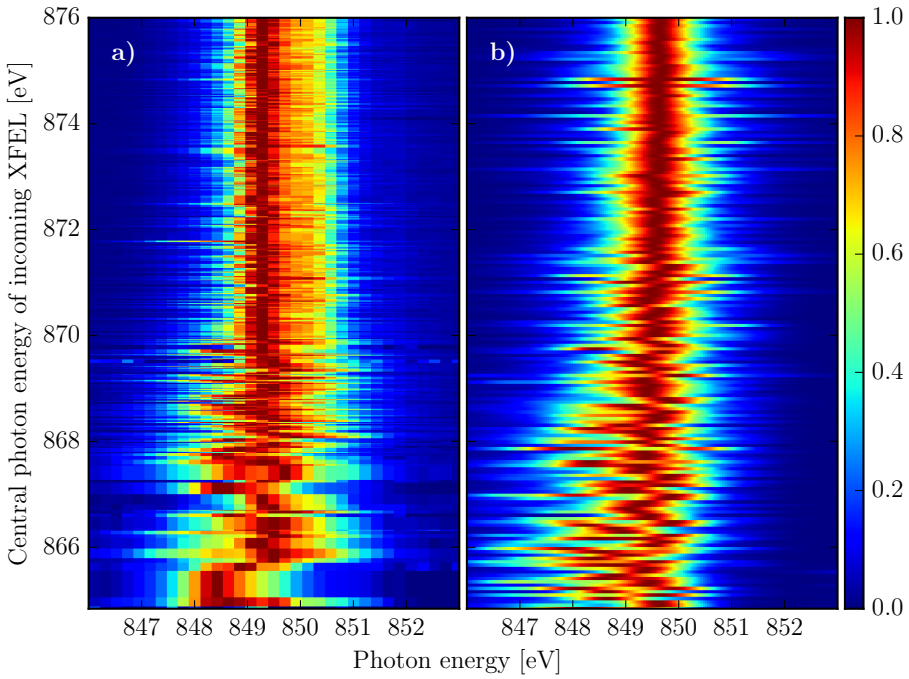

Figure 5.9.: a) Measured single shot emission line shapes as a function of the incoming XFEL photon energy. Every single shot is normalized by its maximum spectral intensity. Spectra that did not show any emission line were filtered out. b) Simulated emission spectra convoluted with a Gaussian with 1 eV FWHM to match experimental resolution [1].

of the LCLS beamline to match the incoming pulse energy.

For shots with photon energy smaller than 870.2 eV an increase of around two orders of magnitude was observed. The shot-to-shot fluctuation for the stimulated Raman scattering is also much stronger and the number of photons is overall weaker. Despite the strong resonant coupling only between 1 % to 10 % of the incoming XFEL photon overlap with the resonances and can excite core electrons. The stimulated Raman signal strongly depends on the incoming photon energy. Fig. 5.10 shows the predicted Raman signal strength from theory for different central photon energies between 865 eV and 869 eV. The calculations show that the Raman gain for 865 eV photon energy is significantly less then for 867 eV due to the bigger detuning from the resonances. For 869 eV there is also a significant contribution from the stimulated K-α fluorescence from photo-ionization to the emission signal, leading to the highest gain. The average

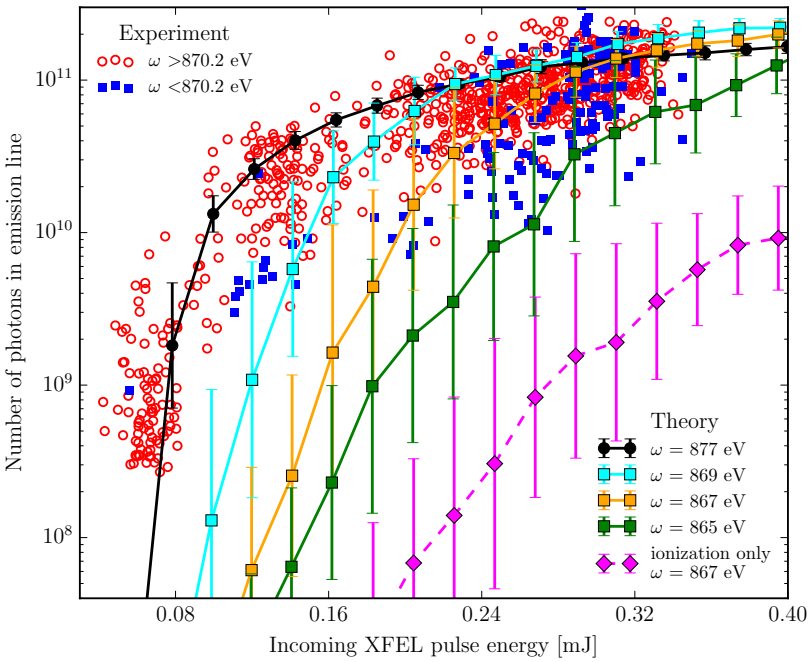

Figure 5.10.: Pump energy dependence of the stimulated emission. Measured number of photons in the emission line as a function of the incoming pulse energy for shots with central XFEL photon above the K edge (red dots) and below the K edge (blue squares). The lines show the number of photons in the emission obtained from theoretical calculations with different central photon energies. The lines correspond to the geometric mean and bars represent the standard deviation over an ensemble of 50 SASE pulses [1].

photon energy of the shots below the edge was 868 eV and the data points are within the standard deviation of the theoretical calculations. It appears that the theoretical calculations underestimate the stimulated Raman gain for low pulse energies. Reasons for the underestimation might be irregularities in the incoming XFEL pulses that are not included in the theoretical XFEL pulses: The XFEL pulses in the experiment showed shot-to-shot variations in the bandwidth, the pulse duration and sporadic spectral side bands at lower photon energies. The stimulated Raman scattering process is very sensitive to the incoming XFEL spectrum. In the saturation regime those effects do not have a big influence on the total emission, but the difference from those effects becomes apparent at lower pulse energies. To further strengthen the conclusion that the emission for shots below 870.2 eV result from stimulated x-ray Raman scattering,

Fig. 5.10 contains a theoretical curve for a calculation with 867 eV central photon energy neglecting the resonant scattering contribution. This curve illustrates that the stimulated K-α fluorescence is not sufficient to explain the measured emission signal. Neglecting the scattering contribution yields a curve that is almost two orders of magnitude below the experimental values. This confirms that stimulated x-ray Raman scattering is necessary to explain the measured signal.

Despite the limited statistics and a low spectral resolution of around 1 eV, stimulated x-ray Raman was observed for the first time. A stochastic line shift was found which is a result of pumping the scattering process with incoherent SASE pulses. To confirm these experimental results the stimulated Raman scattering in neon was reproduced in a second LCLS beam time (LCLS proposal number LB24) with higher spectral resolution and better statistics. Fig. 5.11 shows recorded single shot spectra as a

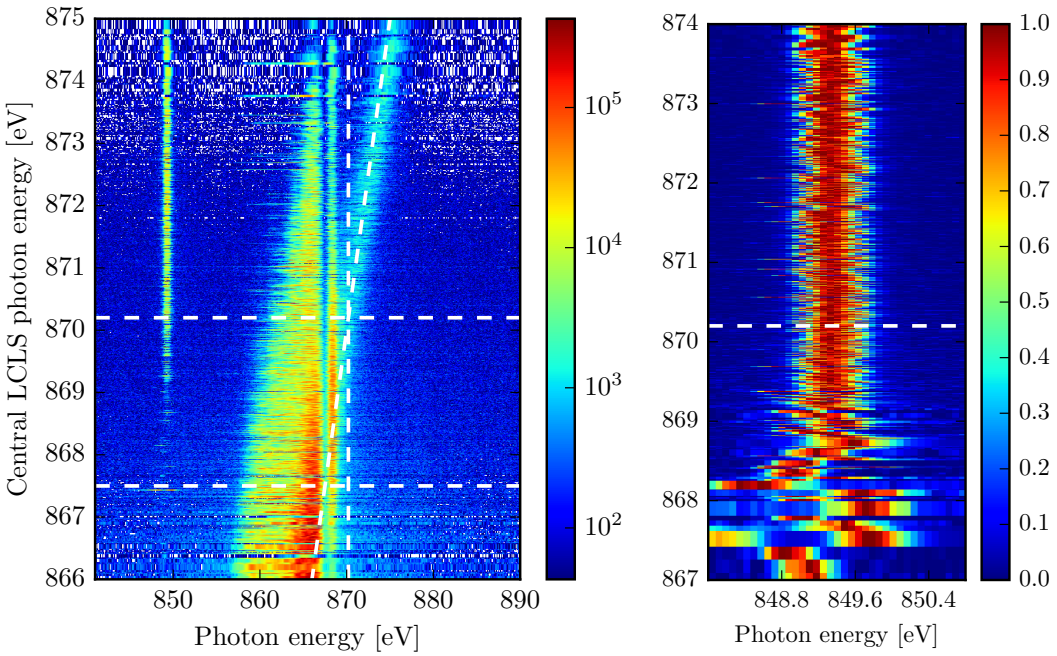

Figure 5.11.: Single shots as a function of the incoming LCLS photon energy from the second LCLS beam time. The right side shows the normalized emission spectra to study the line shape in more detail.

function of the incoming LCLS photon energy, similar to Fig. 5.8. The resolution of the spectrometer was around 0.3 eV in this case. The increased resolution compared to Fig.

5.8 makes the narrow absorption dip due to the 1s-3p resonance much more apparent and appears as a vertical structure around 867.5 eV photon energy to the left of the K edge. The Andor Newton CCD detector detector used in this beam time allowed to obtain better statistics by recording more single shots spectra. The CCD can record full single shot images with 2048×512 pixel at 1 Hz repetition rate. This allowed to record 4537 single shots of which 670 shots are below the K edge. This is more than a factor of three more single shots than in the first beam time. The right side of Fig. 5.11 shows the normalized single shot spectra to study the emission line shape. This plot only contains single shots that show a clear emission line by filtering out shots with a maximum spectral intensity lower than 2000 counts. The line shape below the K edge (870.2) displays the same stochastic shift already observed in Fig. 5.9a). The higher spectral resolution in this case makes the stochastic shift more apparent.

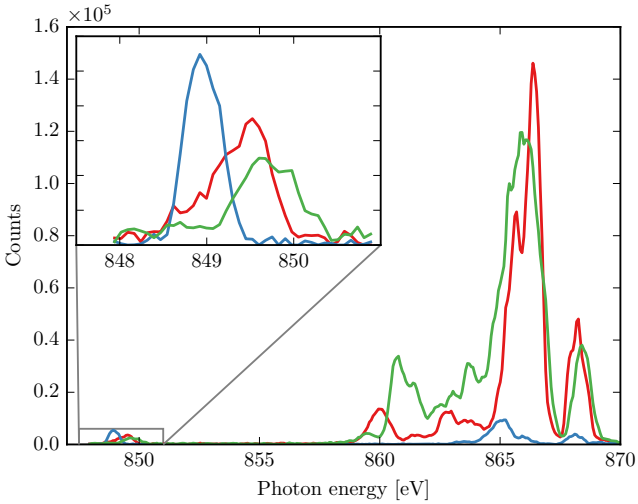

Figure 5.12.: Three single shot spectra for a central LCLS photon energy of 868 eV with 1.1 mJ incoming pulse energy.

Fig. 5.12 shows three single-shot spectra taken at 868 eV central LCLS photon energy. The inset displays the individual emission lines in more detail. Despite the similar central LCLS photon energy the individual emission line shapes are quite different.

Chapter 6

Summary and conclusion

This thesis covers the topic of stimulated emission processes in the x-ray regime in atomic gases. Stimulated emission in the x-ray regime by photo-ionization and stimulated x-ray Raman scattering have been a long-standing challenge. Stimulated x-ray emission has been proposed many years ago and has only recently been experimentally demonstrated. X-ray free electron lasers (XFELs) finally provide the necessary pump intensity to drive stimulated emission processes in the x-ray domain.

To obtain stimulated x-ray emission, pulses from the XFEL with photon energies above an inner-shell ionization edge are focused into an elongated gas medium. The XFEL pulse creates core-holes by photo-ionization and produces a population inversion between the inner-shell orbitals and the valence orbitals. Spontaneous emission in the beginning of the medium can propagate along the medium and gets amplified by stimulated emission. The semi-classical Maxwell-Bloch model, used to study amplified spontaneous emission in neon in chapter 3, revealed that the short lifetime of the upper state leads to unexpected pulse properties during the amplification. The transient x-ray laser does not show the usual spectral gain narrowing and its bandwidth stays constant in the linear gain regime. The amplification of the stimulated emission leads to the build-up of transform limited pulses, even if pumping with an incoherent x-ray source. The flux of current XFELs sources is sufficient to saturate the amplification process and generate short coherent x-ray pulses with few femtosecond pulse duration and around 10^{10} photons. This means that around 1% of the incoming pump photons have been converted into stimulated x-ray emission. A comparison of the common rate equation approach with the Maxwell-Bloch disclosed that the rate equation approach is not sufficient to model transient gain amplifiers with a short upper state lifetime. For a transient gain amplifier it is import to use the Maxwell-Bloch model to include the

gain dependent group velocity for the stimulated emission pulse. The reduced group velocity for the atomic x-ray laser is crucial for maintaining a high gain and balances the shifting of the population due to the pump pulse absorption. When pumping the amplification process with XFEL SASE pulses, the final pulse shape of the atomic x-ray laser varies greatly from shot to shot. The generated pulses can consist of several few femtosecond long spikes in the time domain.

When the XFEL pump pulse is tuned to the resonances below the ionization edge, the process of absorption and emission are no longer separate and lead to a single coherent inelastic scattering event. Spontaneous Raman scattering in the beginning of the medium or photons from the broadband XFEL pulse seed the scattering process and amplify the scattering signal by several orders of magnitude. The bandwidth of XFEL SASE pulses can cover both the resonant region and the above edge region. Theoretical calculations in chapter 4 include both contributions in a single model. This allowed to obtain a detailed understanding of the emission line shape and to distinguish the emission from resonant excitation and ionization. The stochastic nature of the incoherent SASE radiation was taken into account and leads to a complicated and rich structured line shape. The multiple spectral spikes in the broadband radiation can excite multiple resonances with different detunings and generate multiple peaks in the emission spectrum. With the help of statistical tools the spectral resolution of the scattering process can be reduced to the average bandwidth of a single spectral spike instead of the overall bandwidth of the pulse. This enables high resolution spectroscopy by stimulated x-ray Raman scattering with incoherent SASE radiation.

Chapter 5 shows the first experimental demonstration of stimulated x-ray Raman scattering in neon obtained at the LCLS. For the experiment SASE pulses from the LCLS around the K edge of neon were focused into a gas cell filled with neon and the emitted radiation in forward direction was detected with a grating spectrometer. The detailed understanding of the line shape of the scattered radiation from the theoretical modeling in chapter 4 helped in interpreting the experimental results. The experimental data allowed to differentiate the stimulated x-ray Raman scattering from the amplified spontaneous emission. The stochastic shift of the emission frequency for resonant excitation below the K edge is a clear indication for stimulated x-ray Raman scattering with a stochastic source. For the experiment an online monitoring tool was developed to obtain a real time feedback from the experiment. The online monitoring proved to

be very useful in optimizing the setup of the spectrometer and allowed to assess the data quality during the measurement.

Outlook

With the demonstration of stimulated x-ray emission techniques in atoms the challenge remains to extent these techniques to other sample environments and photon energy regimes. The constant development of x-ray free electron lasers opens up new opportunities for stimulated x-ray Raman scattering. The recent advancement of soft x-ray self-seeded pulses at LCLS with photon energies between 500 to 1000 eV [134] allows to generate stable and transform limited x-ray pulses. The self-seeding instrumentation is designed to be compact to only replace a single undulator section. The setup consists of an electron chicane and an x-ray monochromator. For self-seeding the first few undulators of LCLS are used to generate broadband incoherent SASE radiation with up to 5 µJ pulse energy. Afterwards the electron chicane separates the electron beam from the photon beam. The photon beam passes through a grating monochromator to select a narrow photon energy range from the broadband SASE spectrum. The electron chicane resets the electron bunch to a random distribution and washes out the microbuniching from the SASE radiation. The photon beam and the electron beam are then overlapped in space and time and propagate through the remaining undulators. This amplifies the selected narrowband spectrum to pulse energies of up to 1 mJ. The seeded x-ray pulses have a FWHM bandwidth of 175 meV. This narrow bandwidth contains around 40 % of the total pulse energy and the rest of the pulse energy is distributed over a broadband background. The seeded XFEL pulses exceed SASE pulses in peak brightness by a factor of around five due to their narrow bandwidth. With the narrowband and stable seeded pulses it is possible to observe the linear dispersion of the scattering process directly without the need for statistical analysis. Figure 6.1 compares stimulated x-ray Raman scattering with SASE pulses to Raman scattering with narrowband self-seeded pulses. The incoming photon energy of the XFEL pulses is scanned around the pre-edge resonances below the edge. For the stochastic SASE pulses the linear dispersion is not directly evident. For the seeded pulses on the other hand the contribution from the different scattering channels along with the linear dispersion is clearly visible. The narrowband self-seeded XFEL pulses thus enable a direct measurement of the Raman scattering process with high resolution.

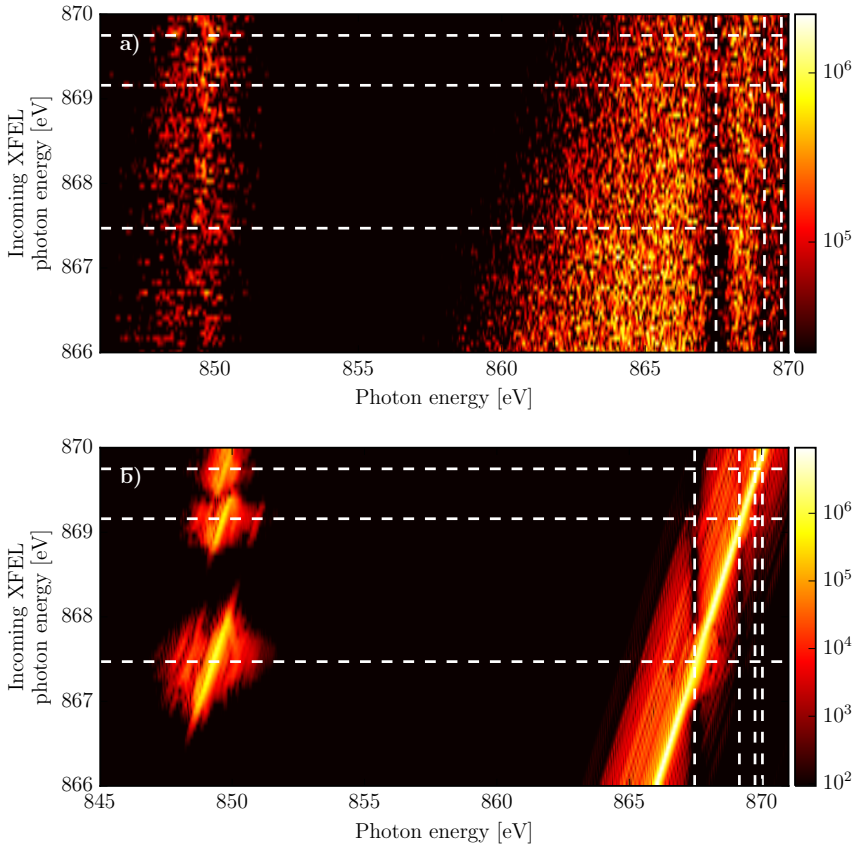

Figure 6.1.: Comparison of stimulated Raman scattering with SASE pulses a) and seeded XFEL pulses b).

A similar resolution can be obtained with SASE pulses making use of statistical analysis like covariance mapping as shown in section 4.5. This statistical analysis, however, requires a large amount of single shot spectra. With seeded pulses less single-shot spectra have to be collected, cutting down the required measurement time.

Extending stimulated emission techniques to the hard x-ray regime requires heavier elements with a shorter core-hole lifetime. Another challenge is the decreasing inner-shell photo-ionization cross section for heavy elements. The photo-ionization cross section at the manganese K edge for example is almost nine times smaller than at the neon K edge. Yoneda et al. demonstrated saturable absorption for hard x-rays in iron [140]. They focused XFEL pulses from SACLA with 7.1 keV photon energy onto iron

foils with a thickness of 20 µm. The incoming XFEL pulses reached x-ray intensities of up to $10^{20}\,\mathrm{W\,cm^{-2}}$ and the transmitted x-rays were detected with a dispersive spectrometer. They observed an increase in transmission by a factor of 10 around the iron K-edge compared to x-ray pulses with lower intensity. The intense x-ray pulses generate a highly excited solid density plasma [9] where electron–ion collisions play an important role. The highly excited plasma leads to a spectral shift of the iron K shell absorption edge. The strong depopulation of the inner-shell electrons leads to absorption bleaching and an increase in transmission. The absorption bleaching demonstrates that current XFEL facilities produce x-ray pulses with sufficient intensity to ionize almost every atom in thin metal foils. This is a prerequisite to obtain a population inversion in the medium, which is required for stimulated x-ray emission. Amplified spontaneous K-α emission in iron at 6.4 keV has already been observed (unpublished).

There has also been first evidence of stimulated emission at 90 eV in solid silicon [175]. XUV pulses from FLASH at DESY with a photon energy of 115 eV and a focus size of around 45 µm were illuminating a crystalline silicon surface in grazing incident with an incident angle of 45 degrees. Stimulated emission from solids requires a different geometry than gas phase and thin foil experiments due to the low penetration depth of soft x-rays in solid samples. In gas phase and thin foil experiments the medium is pumped longitudinally and the stimulated emission is directed in forward direction along the propagation direction of the incoming beam. For solids on the other hand the medium is pumped transversely and the pump beam and the emission beam propagate in different directions. The stimulated emission is directed into a shallow angle with respect to the surface and depends on the ratio of the penetration depth and the spot size of the pump pulse on the surface. The emission was measured for different angles and a maximum was found at an angle of 9 degrees. The intensity of the stimulated emission was about a factor of two above the spontaneous emission intensity.

One application of stimulated x-ray emission is the enhancement of signal in x-ray emission spectroscopy (XES). In XES the sample is excited by an x-ray pulse and the spontaneous fluorescence emission from the sample is detected. A big challenge in XES is to detect enough emitted photons. The fluorescence is emitted into the full 4π solid angle and only a few percent of the these photons can be captured and detected. By stimulating the x-ray emission, it is confined into a well defined direction with

a small solid angle. This results in a drastic reduction of the required measurement time and enhances the sensitivity of x-ray emission spectroscopy. X-ray emission is sensitive to the chemical environment and the x-ray emission energy depends on the configuration of the valence electrons [176, 177]. The chemical shift of the x-ray emission is more pronounced for the outer valence electrons than for the inner valence electrons. In spontaneous x-ray emission the emission from the inner valence electrons is stronger than the emission from the outer valence electrons. The outer valence emission can however be seeded and the subsequent stimulated emission quenches the inner-shell valence emission and allows to greatly enhance the outer valence emission. This approach is going to be tested for different manganese complexes (LCLS proposal number LG89). The two-color mode of LCLS is going to be used to photo-ionize 1s electrons in manganese and to seed the K-β emission. The hope is to quench the stronger K-α emission and to detect a shift of the emission energy for different manganese complexes in different oxidation states. The question is if the chemical information is preserved when stimulating the x-ray emission. The stimulated emission requires a population inversion which means that almost every manganese atom has to be ionized. If the density of the manganese atoms is high, the small distance between neighboring manganese atoms leads to interactions that can result in a shift of the x-ray emission. This effect could potentially overshadow the chemical shift and destroy the chemical information in the x-ray emission. To review this effect the density of the manganese complex is going to be varied from solid density thin foils to solutions with different manganese concentration. Going to low manganese concentration also mimics the condition for stimulated x-ray emission in large complex molecules. In photosystem II, for example, the reaction center consists of only four manganese atoms that are embedded into a large protein complex. In these environments the low density of the target atoms poses a big challenge for stimulated emission. In solution there is also an inhomogeneous broadening of the emission line due to the environment. Interaction with the solvent leads to a small individual shift of the energy levels for every atom that is transferred to the x-ray emission.

X-ray lasing in diatomic molecules has also been explored theoretically in nitrogen N_2 [178] and CO[179]. The vibrational dynamics in molecules prove to be crucial for the x-ray lasing process and x-ray lasing in molecules with current XFEL sources is feasible. For stimulated emission from molecules the alignment of the molecules however is quite

important as the emission dipoles are oriented in molecules. The molecules can be aligned with strong optical laser pulses [180–182]. There has been an experimental campaign at LCLS to observe stimulated x-ray Raman scattering. The LCLS was operating in the two color mode to provide a strong pump pulse at the oxygen $\pi^\star$ resonance and a much weaker pulse at a lower photon energy to seed the Raman scattering. Unfortunately the available pulse energy during the experiment was lower than anticipated and not sufficient to observe simulated x-ray Raman scattering in CO [183]. There is a new attempt (LCLS proposal number LI17) to observe stimulated x-ray Raman scattering in CO with seeded pulses making use of the new soft x-ray self seeding capabilities of LCLS [134]. The self-seeding allows to generate pump pulses with a much narrower bandwidth than SASE pulses which increases the available photon flux at the resonant pump transition.

Bibliography

[1] C. Weninger, M. Purvis, D. Ryan, R. A. London, J. D. Bozek, C. Bostedt, A. Graf, G. Brown, J. J. Rocca, and N. Rohringer, "Stimulated Electronic X-Ray Raman Scattering," Phys. Rev. Lett. **111**, 233902 (2013).

[2] C. Weninger and N. Rohringer, "Stimulated resonant x-ray Raman scattering with incoherent radiation," Phys. Rev. A **88**, 053421 (2013).

[3] C. Weninger and N. Rohringer, "Transient-gain photoionization x-ray laser," Phys. Rev. A **90**, 063828 (2014).

[4] J. Marangos, "Introduction to the new science with x-ray free electron lasers," Contemporary Physics **52**, 551 (2011).

[5] R. Neutze, R. Wouts, D. van der Spoel, E. Weckert, and J. Hajdu, "Potential for biomolecular imaging with femtosecond X-ray pulses," Nature **406**, 752 (2000).

[6] H. N. Chapman *et al.*, "Femtosecond X-ray protein nanocrystallography," Nature **470**, 73 (2011).

[7] S. Boutet *et al.*, "High-Resolution Protein Structure Determination by Serial Femtosecond Crystallography," Science **337**, 362 (2012).

[8] W. Liu *et al.*, "Serial Femtosecond Crystallography of G Protein–Coupled Receptors," Science **342**, 1521 (2013).

[9] S. M. Vinko *et al.*, "Creation and diagnosis of a solid-density plasma with an X-ray free-electron laser," Nature **482**, 59 (2012).

[10] S. Schorb *et al.*, "Size-Dependent Ultrafast Ionization Dynamics of Nanoscale Samples in Intense Femtosecond X-Ray Free-Electron-Laser Pulses," Phys. Rev. Lett. **108**, 233401 (2012).

[11] C. E. Graves *et al.*, "Nanoscale spin reversal by non-local angular momentum transfer following ultrafast laser excitation in ferrimagnetic GdFeCo," Nature Mater. **12**, 293 (2013).

[12] T. Kubacka *et al.*, "Large-Amplitude Spin Dynamics Driven by a THz Pulse in Resonance with an Electromagnon," Science **343**, 1333 (2014).

[13] M. Först *et al.*, "Melting of Charge Stripes in Vibrationally Driven $La_{1.875}Ba_{0.125}CuO_4$: Assessing the Respective Roles of Electronic and Lattice Order in Frustrated Superconductors," Phys. Rev. Lett. **112**, 157002 (2014).

[14] M. Dell'Angela *et al.*, "Real-Time Observation of Surface Bond Breaking with an X-ray Laser," Science **339**, 1302 (2013), pMID: 23493709.

[15] J. Kern *et al.*, "Simultaneous Femtosecond X-ray Spectroscopy and Diffraction of Photosystem II at Room Temperature," Science **340**, 491 (2013).

[16] L. Young *et al.*, "Femtosecond electronic response of atoms to ultra-intense x-rays," Nature **466**, 56 (2010).

[17] B. Rudek *et al.*, "Ultra-efficient ionization of heavy atoms by intense x-ray free-electron laser pulses," Nature Photon. **6**, 858 (2012).

[18] H. M. Quiney and K. A. Nugent, "Biomolecular imaging and electronic damage using x-ray free-electron lasers," Nature Phys. **7**, 142 (2011).

[19] E. K. Curwood, H. M. Quiney, and K. A. Nugent, "Determining electronic damage to biomolecular structures in x-ray free-electron-laser imaging experiments," Phys. Rev. A **87**, 053407 (2013).

[20] N. Rohringer and R. Santra, "X-ray nonlinear optical processes using a self-amplified spontaneous emission free-electron laser," Phys. Rev. A **76**, 033416 (2007).

[21] K. Tamasaku *et al.*, "Double core-hole creation by sequential attosecond photoionization," Phys. Rev. Lett. **111**, 043001 (2013).

[22] K. Tamasaku *et al.*, "X-ray two-photon absorption competing against single and sequential multiphoton processes," Nature Photon. **8**, 313 (2014).

[23] T. E. Glover *et al.*, "X-ray and optical wave mixing," Nature **488**, 603 (2012).

[24] S. Shwartz *et al.*, "X-ray second harmonic generation," Phys. Rev. Lett. **112**, 163901 (2014).

[25] R. Alonso-Mori *et al.*, "Energy-dispersive X-ray emission spectroscopy using an X-ray free-electron laser in a shot-by-shot mode," PNAS (2012), 10.1073/pnas.1211384109.

[26] Y. Zhang, J. D. Biggs, N. Govind, and S. Mukamel, "Monitoring long-range electron transfer pathways in proteins by stimulated attosecond broadband x-ray raman spectroscopy," J. Phys. Chem. Lett. **5**, 3656 (2014).

[27] J. M. J. Madey, "Stimulated Emission of Bremsstrahlung in a Periodic Magnetic Field," J. Appl. Phys **42**, 1906 (1971).

[28] A. Kondratenko and E. Saldin, "Generation of coherent radiation by a relativistic electron beam in an undulator," Part. Accel. **10**, 207 (1980).

[29] J. Andruszkow *et al.*, "First observation of self-amplified spontaneous emission in a free-electron laser at 109 nm wavelength," Phys. Rev. Lett. **85**, 3825 (2000).

[30] V. Ayvazyan *et al.*, "Generation of GW radiation pulses from a VUV free-electron laser operating in the femtosecond regime," Phys. Rev. Lett. **88**, 104802 (2002).

[31] V. Ayvazyan *et al.*, "A new powerful source for coherent VUV radiation: Demonstration of exponential growth and saturation at the TTF free-electron laser," Eur. Phys. J. D **20**, 149 (2002).

[32] Z. Huang and K.-J. Kim, "Review of x-ray free-electron laser theory," Phys. Rev. ST Accel. Beams **10**, 034801 (2007).

[33] J. Feldhaus, J. Arthur, and J. B. Hastings, "X-ray free-electron lasers," J. Phys. B: At. Mol. Opt. Phys. **38**, S799 (2005).

[34] D. H. Bilderback, P. Elleaume, and E. Weckert, "Review of third and next generation synchrotron light sources," J. Phys. B: At. Mol. Opt. Phys. **38**, S773 (2005).

[35] E. L. Saldin, E. A. Schneidmiller, and M. V. Yurkov, "Statistical properties of radiation from vuv and x-ray free electron laser," Opt. Commun. **148**, 383 (1998).

[36] E. L. Saldin, E. A. Schneidmiller, and M. V. Yurkov, "Coherence properties of the radiation from x-ray free electron laser," Opt. Commun. **281**, 1179 (2008).

[37] S. Roling *et al.*, "Temporal and spatial coherence properties of free-electron-laser pulses in the extreme ultraviolet regime," Phys. Rev. ST Accel. Beams **14**, 080701 (2011).

[38] S. Lee *et al.*, "Single shot speckle and coherence analysis of the hard X-ray free electron laser LCLS," Opt. Express **21**, 24647 (2013).

[39] C. David *et al.*, "Nanofocusing of hard x-ray free electron laser pulses using diamond based fresnel zone plates," Sci. Rep. **1** (2011), 10.1038/srep00057.

[40] H. Mimura *et al.*, "Generation of 1020 w cm-2 hard x-ray laser pulses with two-stage reflective focusing system," Nat. Commun. **5** (2014), 10.1038/ncomms4539.

[41] I. Grguraš *et al.*, "Ultrafast X-ray pulse characterization at free-electron lasers," Nature Photon. **6**, 852 (2012).

[42] S. Schulz *et al.*, "Femtosecond all-optical synchronization of an X-ray free-electron laser," Nat. Commun. **6**, 5938 (2015).

[43] M. Harmand *et al.*, "Achieving few-femtosecond time-sorting at hard X-ray free-electron lasers," Nature Photon. **7**, 215 (2013).

[44] L. H. Yu, "Generation of intense uv radiation by subharmonically seeded single-pass free-electron lasers," Phys. Rev. A **44**, 5178 (1991).

[45] Z. T. Zhao *et al.*, "First lasing of an echo-enabled harmonic generation free-electron laser," Nature Photonics **6**, 360 (2012).

[46] S. Ackermann *et al.*, "Generation of Coherent 19- and 38-nm Radiation at a Free-Electron Laser Directly Seeded at 38~nm," Phys. Rev. Lett. **111**, 114801 (2013).

[47] G. Geloni, V. Kocharyan, and E. Saldin, "Scheme for generation of highly monochromatic X-rays from a baseline XFEL undulator," arXiv:1003.2548 (2010).

[48] J. Amann *et al.*, "Demonstration of self-seeding in a hard-X-ray free-electron laser," Nature Photonics **6**, 693 (2012).

[49] F. Grüner *et al.*, "Design considerations for table-top, laser-based VUV and X-ray free electron lasers," Appl. Phys. B **86**, 431 (2007).

[50] M. Fuchs *et al.*, "Laser-driven soft-X-ray undulator source," Nature Phys. **5**, 826 (2009).

[51] A. R. Maier, A. Meseck, S. Reiche, C. B. Schroeder, T. Seggebrock, and F. Grüner, "Demonstration Scheme for a Laser-Plasma-Driven Free-Electron Laser," Phys. Rev. X **2**, 031019 (2012).

[52] C. Joshi, W. B. Mori, T. Katsouleas, J. M. Dawson, J. M. Kindel, and D. W. Forslund, "Ultrahigh gradient particle acceleration by intense laser-driven plasma density waves," Nature **311**, 525 (1984).

[53] W. P. Leemans, B. Nagler, A. J. Gonsalves, C. Tóth, K. Nakamura, C. G. R. Geddes, E. Esarey, C. B. Schroeder, and S. M. Hooker, "GeV electron beams from a centimetre-scale accelerator," Nature Physics **2**, 696 (2006).

[54] M. Fuchs *et al.*, "First milestone on the path toward a table-top free-electron laser (FEL)," in *AIP Conference Proceedings*, Vol. 1228 (2010) pp. 295–299.

[55] V. Ayvazyan *et al.*, "First operation of a free-electron laser generating GW power radiation at 32 nm wavelength," Eur. Phys. J. D **37**, 297 (2006).

[56] W. Ackermann *et al.*, "Operation of a free-electron laser from the extreme ultraviolet to the water window," Nature Photon. **1**, 336 (2007).

[57] P. Emma *et al.*, "First lasing and operation of an ångstrom-wavelength free-electron laser," Nature Photon. **4**, 641 (2010).

[58] T. Ishikawa *et al.*, "A compact x-ray free-electron laser emitting in the sub-ångstrom region," Nature Photon. **6**, 540 (2012).

[59] E. Allaria *et al.*, "Highly coherent and stable pulses from the FERMI seeded free-electron laser in the extreme ultraviolet," Nature Photon. **6**, 699 (2012).

[60] T. H. Maiman, "Stimulated Optical Radiation in Ruby," Nature **187**, 493 (1960).

[61] J. J. Rocca, "Table-top soft x-ray lasers," Rev. Sci. Instrum. **70**, 3799 (1999).

[62] M. A. Duguay and P. M. Rentzepis, "SOME APPROACHES TO VACUUM UV AND X-RAY LASERS," Appl. Phys. Lett. **10**, 350 (1967).

[63] T. S. Axelrod, "Inner-shell photoionization-pumped x-ray lasers. sulfur," Phys. Rev. A **13**, 376 (1976).

[64] H. C. Kapteyn, "Photoionization-pumped x-ray lasers using ultrashort-pulse excitation," Appl. Opt. **31**, 4931 (1992).

[65] N. Rohringer and R. London, "Atomic inner-shell x-ray laser pumped by an x-ray free-electron laser," Phys. Rev. A **80**, 013809 (2009).

[66] M. Ribière *et al.*, "Femtosecond coherent pulses in the keV range from inner-shell transitions pumped by a betatron source," Appl. Phys. B **101**, 753 (2010).

[67] S. Suckewer, C. H. Skinner, H. Milchberg, C. Keane, and D. Voorhees, "Amplification of stimulated soft x-ray emission in a confined plasma column," Phys. Rev. Lett. **55**, 1753 (1985).

[68] D. L. Matthews *et al.*, "Demonstration of a Soft X-Ray Amplifier," Phys. Rev. Lett. **54**, 110 (1985).

[69] B. J. MacGowan *et al.*, "Demonstration of x-ray amplifiers near the carbon K edge," Phys. Rev. Lett. **65**, 420 (1990).

[70] J. Dunn, A. L. Osterheld, R. Shepherd, W. E. White, V. N. Shlyaptsev, and R. E. Stewart, "Demonstration of X-Ray Amplification in Transient Gain Nickel-like Palladium Scheme," Phys. Rev. Lett. **80**, 2825 (1998).

[71] J. J. Rocca, Y. Wang, M. A. Larotonda, B. M. Luther, M. Berrill, and D. Alessi, "Saturated 13.2 nm high-repetition-rate laser in nickellike cadmium," Opt. Lett. **30**, 2581 (2005).

[72] Y. Wang *et al.*, "Demonstration of high-repetition-rate tabletop soft-x-ray lasers with saturated output at wavelengths down to 13.9nm and gain down to 10.9nm," Phys. Rev. A **72**, 053807 (2005).

[73] K. Lan, E. Fill, and J. Meyer-Ter-Vehn, "Photopumping of XUV lasers by XFEL radiation," Laser Part. Beams **22**, 261 (2004).

[74] J. Zhao, Q. L. Dong, S. J. Wang, L. Zhang, and J. Zhang, "X-ray lasers from inner-shell transitions pumped by the free-electron laser," Opt. Express **16**, 3546 (2008).

[75] N. Rohringer *et al.*, "Atomic inner-shell x-ray laser at 1.46 nanometres pumped by an x-ray free-electron laser," Nature **481**, 488 (2012).

[76] S. Mukamel, D. Healion, Y. Zhang, and J. D. Biggs, "Multidimensional Attosecond Resonant X-Ray Spectroscopy of Molecules: Lessons from the Optical Regime," Annu. Rev. Phys. Chem. **64**, 101 (2013).

[77] E. Mallet, P. Disseix, D. Lagarde, M. Mihailovic, F. Réveret, T. V. Shubina, and J. Leymarie, "Accurate determination of homogeneous and inhomogeneous excitonic broadening in ZnO by linear and nonlinear spectroscopies," Phy. Rev. B **87**, 161202 (2013).

[78] A. Zumbusch, G. R. Holtom, and X. S. Xie, "Three-Dimensional Vibrational Imaging by Coherent Anti-Stokes Raman Scattering," Phys. Rev. Lett. **82**, 4142 (1999).

[79] C. W. Freudiger, W. Yang, G. R. Holtom, N. Peyghambarian, X. S. Xie, and K. Q. Kieu, "Stimulated Raman scattering microscopy with a robust fibre laser source," Nat Photon **8**, 153 (2014).

[80] E. Ploetz, S. Laimgruber, S. Berner, W. Zinth, and P. Gilch, "Femtosecond stimulated Raman microscopy," Appl. Phys. B **87**, 389 (2007).

[81] C. W. Freudiger *et al.*, "Label-Free Biomedical Imaging with High Sensitivity by Stimulated Raman Scattering Microscopy," Science **322**, 1857 (2008).

[82] P. Nandakumar, A. Kovalev, and A. Volkmer, "Vibrational imaging based on stimulated Raman scattering microscopy," New J. Phys. **11**, 033026 (2009).

[83] P. Kukura, D. W. McCamant, S. Yoon, D. B. Wandschneider, and R. A. Mathies, "Structural Observation of the Primary Isomerization in Vision with Femtosecond-Stimulated Raman," Science **310**, 1006 (2005).

[84] G. S. Engel *et al.*, "Evidence for wavelike energy transfer through quantum coherence in photosynthetic systems," Nature **446**, 782 (2007).

[85] B. Spokoyny and E. Harel, "Mapping the Vibronic Structure of a Molecule by Few-Cycle Continuum Two-Dimensional Spectroscopy in a Single Pulse," J. Phys. Chem. Lett. **5**, 2808 (2014).

[86] E. Collini *et al.*, "Coherently wired light-harvesting in photosynthetic marine algae at ambient temperature," Nature **463**, 644 (2010).

[87] M. Cho, "Coherent Two-Dimensional Optical Spectroscopy," Chem. Rev. **108**, 1331 (2008).

[88] D. Abramavicius, B. Palmieri, D. V. Voronine, F. Šanda, and S. Mukamel, "Coherent Multidimensional Optical Spectroscopy of Excitons in Molecular Aggregates; Quasiparticle versus Supermolecule Perspectives," Chem. Rev. **109**, 2350 (2009).

[89] P. Hamm, J. Helbing, and J. Bredenbeck, "Two-Dimensional Infrared Spectroscopy of Photoswitchable Peptides," Annu. Rev. Phys. Chem. **59**, 291 (2008).

[90] A. C. Thompson, *X-ray data booklet* (University of Berkeley, 2001).

[91] A. A. Mrse *et al.*, "Solid-state NMR and XANES studies of lithium and silver silicate gels synthesized by the sol–gel route," J. Non-Cryst. Solids. **318**, 296 (2003).

[92] S. Tanaka and S. Mukamel, "Coherent X-Ray Raman Spectroscopy: A Nonlinear Local Probe for Electronic Excitations," Phys. Rev. Lett. **89**, 043001 (2002).

[93] U. Harbola and S. Mukamel, "Coherent stimulated x-ray Raman spectroscopy: Attosecond extension of resonant inelastic x-ray Raman scattering," Phys. Rev. B **79**, 085108 (2009).

[94] D. Healion, H. Wang, and S. Mukamel, "Simulation and visualization of attosecond stimulated x-ray Raman spectroscopy signals in trans-N-methylacetamide at the nitrogen and oxygen K-edges," J. Chem. Phys. **134**, 124101 (2011).

[95] A. Kotani and S. Shin, "Resonant inelastic x-ray scattering spectra for electrons in solids," Rev. Mod. Phys. **73**, 203 (2001).

[96] L. J. P. Ament, M. van Veenendaal, T. P. Devereaux, J. P. Hill, and J. van den Brink, "Resonant inelastic x-ray scattering studies of elementary excitations," Rev. Mod. Phys. **83**, 705 (2011).

[97] P. Marra, S. Sykora, K. Wohlfeld, and J. van den Brink, "Resonant Inelastic X-Ray Scattering as a Probe of the Phase and Excitations of the Order Parameter of Superconductors," Phys. Rev. Lett. **110**, 117005 (2013).

[98] V. Bisogni and other, "Femtosecond Dynamics of Momentum-Dependent Magnetic Excitations from Resonant Inelastic X-Ray Scattering in $CaCu_2O_3$," Phys. Rev. Lett. **112**, 147401 (2014).

[99] S. Grenier *et al.*, "d-d Excitations in Manganites Probed by Resonant Inelastic X-Ray Scattering," Phys. Rev. Lett. **94**, 047203 (2005).

[100] U. Bergmann, P. Glatzel, and S. P. Cramer, "Bulk-sensitive XAS characterization of light elements: from X-ray Raman scattering to X-ray Raman spectroscopy," Microchem. J. **71**, 221 (2002).

[101] P. L. Manning *et al.*, "Synchrotron-based chemical imaging reveals plumage patterns in a 150 million year old early bird," J. Anal. At. Spectrom. **28**, 1024 (2013).

[102] P. Eisenberger, P. M. Platzman, and H. Winick, "X-Ray Resonant Raman Scattering: Observation of Characteristic Radiation Narrower than the Lifetime Width," Phys. Rev. Lett. **36**, 623 (1976).

[103] T. J. Bürvenich, J. Evers, and C. H. Keitel, "Nuclear quantum optics with x-ray laser pulses," Phys. Rev. Lett. **96**, 142501 (2006).

[104] P. B. Corkum, "Plasma perspective on strong field multiphoton ionization," Phys. Rev. Lett. **71**, 1994 (1993).

[105] A. De Fanis, N. Saito, H. Yoshida, Y. Senba, Y. Tamenori, H. Ohashi, H. Tanaka, and K. Ueda, "Interference effects in the resonant photoemission channels to the Ne^+ $2p^4(^1D_2)3p$ ^2P, ^2D, and ^2F states in the ne $1s$ excitation region," Phys. Rev. Lett. **89**, 243001 (2002).

[106] N. Rohringer and R. Santra, "Strongly driven resonant Auger effect treated by an open-quantum-system approach," Phys. Rev. A **86**, 043434 (2012).

[107] J. D. Jackson, *Classical Electrodynamics* (John Wiley & Sons, New York, 1998).

[108] T. Gorkhover *et al.*, "Nanoplasma dynamics of single large xenon clusters irradiated with superintense x-ray pulses from the linac coherent light source free-electron laser," Physical Review Letters **108**, 245005 (2012).

[109] O. Larroche *et al.*, "Maxwell-Bloch modeling of x-ray-laser-signal buildup in single- and double-pass configurations," Phys. Rev. A **62**, 043815 (2000).

[110] B. Fidel, E. Heyman, R. Kastner, and R. Ziolkowski, "Hybrid Ray–FDTD moving window approach to pulse propagation," J. Comput. Phys. **138**, 480 (1997).

[111] F. Schwabl, *Statistical Mechanics* (Springer Science & Business Media, 2002).

[112] B. Bidégaray, A. Bourgeade, and D. Reignier, "Introducing physical relaxation terms in bloch equations," J. Comput. Phys. **170**, 603 (2001).

[113] A. Alvermann, H. Fehske, and P. B. Littlewood, "Numerical time propagation of quantum systems in radiation fields," New J. Phys. **14**, 105008 (2012).

[114] R. I. McLachlan and G. R. W. Quispel, "Splitting methods," Acta Numerica **11**, 341 (2002).

[115] C. Moler and C. V. Loan, "Nineteen dubious ways to compute the exponential of a matrix," SIAM Review **20**, 801–836 (1978).

[116] H. Tal-Ezer and R. Kosloff, "An accurate and efficient scheme for propagating the time dependent schrödinger equation," J. Chem. Phys **81**, 3967 (1984).

[117] A. L. Frapiccini *et al.*, "Explicit schemes for time propagating many-body wave functions," Phys. Rev. A **89**, 023418 (2014).

[118] V. Weisskopf and E. Wigner, "Berechnung der natürlichen linienbreite auf grund der diracschen lichttheorie," Z. Physik **63**, 54 (1930).

[119] A. Singer *et al.*, "Hanbury Brown–Twiss interferometry at a free-electron laser," Phys. Rev. Lett. **111**, 034802 (2013).

[120] R. Bonifacio, C. Pellegrini, and L. Narducci, "Collective instabilities and high-gain regime in a free electron laser," Opt. Commun. **50**, 373 (1984).

[121] S. Krinsky and R. L. Gluckstern, "Analysis of statistical correlations and intensity spiking in the self-amplified spontaneous-emission free-electron laser," Phys. Rev. ST Accel. Beams **6**, 050701 (2003).

[122] G. Vannucci and M. C. Teich, "Computer simulation of superposed coherent and chaotic radiation," Appl. Opt. **19**, 548 (1980).

[123] Q. Miao, J.-C. Liu, H. Ågren, J.-E. Rubensson, and F. Gel'mukhanov, "Dissociative X-ray Lasing," Phys. Rev. Lett. **109**, 233905 (2012).

[124] F. A. Hopf and P. Meystre, "Quantum theory of a swept-gain laser amplifier," Phys. Rev. A **12**, 2534 (1975).

[125] F. Hopf, P. Meystre, and D. W. McLaughlin, "Quantum theory of a swept-gain amplifier. II," Phys. Rev. A **13**, 777 (1976).

[126] I. V. Schweigert and S. Mukamel, "Probing valence electronic wave-packet dynamics by all x-ray stimulated raman spectroscopy: A simulation study," Phys. Rev. A **76**, 012504 (2007).

[127] J. D. Biggs, Y. Zhang, D. Healion, and S. Mukamel, "Two-dimensional stimulated resonance raman spectroscopy of molecules with broadband x-ray pulses," J. Chem. Phys **136**, 174117 (2012).

[128] F. Kannari and M. Obara, "Multilevel maxwell bloch-equation description of ultrashort laser pulse amplification in inhomogeneously broadened XeCl media," J. Opt. Soc. Am. B **7**, 1493 (1990).

[129] E. Oliva, P. Zeitoun, M. Fajardo, G. Lambert, D. Ros, S. Sebban, and P. Velarde, "Comparison of natural and forced amplification regimes in plasma-based soft-x-ray lasers seeded by high-order harmonics," Phys. Rev. A **84**, 013811 (2011).

[130] Y. Wang *et al.*, "Gain dynamics in a soft-x-ray laser amplifier perturbed by a strong injected x-ray field," Nature Photon. **8**, 381 (2014).

[131] F. Tissandier, S. Sebban, J. Gautier, P. Zeitoun, E. Oliva, A. Rousse, and G. Maynard, "Three-dimensional maxwell-bloch calculation of the temporal profile of a seeded soft x-ray laser pulse," Appl. Phys. Lett. **101**, 251112 (2012).

[132] R. D. Cowan, *The Theory of Atomic Structure and Spectra* (University of California Press, 1981).

[133] N. Rohringer, A. Gordon, and R. Santra, "Configuration-interaction-based time-dependent orbital approach for *ab initio* treatment of electronic dynamics in a strong optical laser field," Phys. Rev. A **74**, 043420 (2006).

[134] D. Ratner *et al.*, "Experimental demonstration of a soft x-ray self-seeded free-electron laser," Phys. Rev. Lett. **114**, 054801 (2015).

[135] P. Meystre and M. Sargent, *Elements of Quantum Optics* (Springer, 2007).

[136] L. W. Casperson, "Threshold characteristics of mirrorless lasers," J. Appl. Phys. **48**, 256 (1977).

[137] G. J. Pert, "Output characteristics of amplified-stimulated-emission lasers," J. Opt. Soc. Am. B **11**, 1425 (1994).

[138] B. Nagler *et al.*, "Turning solid aluminium transparent by intense soft x-ray photoionization," Nature Phys. **5**, 693 (2009).

[139] K. Hatada and A. Di Cicco, "Modeling saturable absorption for ultra short x-ray pulses," J. Electron Spectrosc. Relat. Phenom. **196**, 177 (2014).

[140] H. Yoneda *et al.*, "Saturable absorption of intense hard x-rays in iron," Nat. Commun. **5**, 5080 (2014).

[141] D. Rackstraw *et al.*, "Saturable absorption of an x-ray free-electron-laser heated solid-density aluminum plasma," Phys. Rev. Lett. **114**, 015003 (2015).

[142] L. Casperson and A. Yariv, "Pulse propagation in a high-gain medium," Phys. Rev. Lett. **26**, 293 (1971).

[143] R. Tommasini and E. Fill, "Excitation-velocity and group-velocity mismatch in amplified spontaneous emission lasers: A discussion on the transient gain x-ray lasers," Phys. Rev. A **62**, 034701 (2000).

[144] F. Strati and G. J. Tallents, "Analytical modeling of group-velocity effects in saturated soft-x-ray lasers pumped with a picosecond traveling-wave excitation," Phys. Rev. A **64**, 013807 (2001).

[145] F. A. Hopf, P. Meystre, M. O. Scully, and J. F. Seely, "Coherence brightening and laser lethargy in x-ray laser amplifiers," Phys. Rev. Lett. **35**, 511 (1975).

[146] F. A. Hopf, "Influence of slippage parameter on swept-gain amplifiers," Phys. Rev. A **30**, 3336 (1984).

[147] W. H. Press, S. A. Teukolsky, W. T. Vetterling, and B. P. Flannery, *Numerical Recipes 3rd Edition: The Art of Scientific Computing*, 3rd ed. (Cambridge University Press, Cambridge, UK ; New York, 2007).

[148] G. L. LAMB, "Analytical descriptions of ultrashort optical pulse propagation in a resonant medium," Rev. Mod. Phys. **43**, 99 (1971).

[149] J.-Z. Zhang and I. Galbraith, "Rabi oscillations of ultrashort optical pulses in 1.55 µm InGaAs/InGaAsP quantum-well amplifiers," J. Appl. Phys. **96**, 922 (2004).

[150] M. Kolarczik, N. Owschimikow, J. Korn, B. Lingnau, Y. Kaptan, D. Bimberg, E. Schöll, K. Lüdge, and U. Woggon, "Quantum coherence induces pulse shape modification in a semiconductor optical amplifier at room temperature," Nat. Commun. **4** (2013), 10.1038/ncomms3953.

[151] R. J. Glauber, *Wiley: Quantum Theory of Optical Coherence: Selected Papers and Lectures* (Wiley-VCH, 2006).

[152] M. Le Tacon *et al.*, "Intense paramagnon excitations in a large family of high-temperature superconductors," Nat Phys **7**, 725 (2011).

[153] M. P. M. Dean *et al.*, "Spin excitations in a single La_2CuO_4 layer," Nat. Mater. **11**, 850 (2012).

[154] P. Glatzel *et al.*, "The Electronic Structure of Mn in Oxides, Coordination Complexes, and the Oxygen-Evolving Complex of Photosystem II Studied by Resonant Inelastic X-ray Scattering," J. Am. Chem. Soc. **126**, 9946 (2004).

[155] Y.-J. Kim, J. P. Hill, H. Yamaguchi, T. Gog, and D. Casa, "Resonant inelastic x-ray scattering study of the electronic structure of Cu_2O," Phys. Rev. B **81**, 195202 (2010).

[156] E. E. Fill, S. J. van Enk, J. Zhang, and P. Lambropoulos, "Stimulated Raman scattering in helium with soft-x-ray laser radiation," Phys. Rev. A **54**, 5374 (1996).

[157] Y.-P. Sun, J.-C. Liu, C.-K. Wang, and F. Gel'mukhanov, "Propagation of a strong x-ray pulse: Pulse compression, stimulated Raman scattering, amplified spontaneous emission, lasing without inversion, and four-wave mixing," Phys. Rev. A **81**, 013812 (2010).

[158] E. Hudis, P. L. Shkolnikov, and A. E. Kaplan, "X-ray-stimulated electronic Raman scattering in neutral gases and inhibited ionization," J. Opt. Soc. Am. B **11**, 1158 (1994).

[159] W. Schuelke, *Electron Dynamics by Inelastic X-Ray Scattering* (Oxford University Press, 2007).

[160] G. Placzek, "Rayleigh-Streuung und Raman-Effekt," Handbuch der Radiologie **6**, 205 (1934).

[161] J. Mostowski and M. G. Raymer, "The buildup of stimulated raman scattering from spontaneous raman scattering," Opt. Commun. **36**, 237 (1981).

[162] R. W. Boyd, *Nonlinear Optics*, 3rd ed. (Academic Press, 2008).

[163] F. Gel'mukhanov and H. Ågren, "Resonant X-ray Raman scattering," Physics Reports **312**, 87 (1999).

[164] S. Carniato, R. Taïeb, L. Journel, R. Guillemin, W. C. Stolte, D. W. Lindle, F. Gel'mukhanov, and M. Simon, "Resonant X-ray Raman scattering on molecules: A benchmark study on HCl," J. Electron. Spectrosc. Relat. Phenom. **181**, 116 (2010).

[165] L. J. Frasinski, K. Codling, and P. A. Hatherly, "Covariance Mapping: A Correlation Method Applied to Multiphoton Multiple Ionization," Science **246**, 1029 (1989).

[166] L. J. Frasinski *et al.*, "Dynamics of Hollow Atom Formation in Intense X-Ray Pulses Probed by Partial Covariance Mapping," Phys. Rev. Lett. **111**, 073002 (2013).

[167] V. Zhaunerchyk, L. J. Frasinski, J. H. D. Eland, and R. Feifel, "Theory and simulations of covariance mapping in multiple dimensions for data analysis in high-event-rate experiments," Phys. Rev. A **89**, 053418 (2014).

[168] J. D. Bozek, "AMO instrumentation for the LCLS x-ray FEL," Eur. Phys. J. Spec. Top. **169**, 129 (2009).

[169] P. KIRKPATRICK and A. V. BAEZ, "Formation of Optical Images by X-Rays," J. Opt. Soc. Am. **38**, 766 (1948).

[170] R. Soufli *et al.*, "Development, characterization and experimental performance of x-ray optics for the LCLS free-electron laser," in *Proc. SPIE*, Vol. 7077 (2008) pp. 707716–707716.

[171] P. Denes, D. Doering, H. A. Padmore, J.-P. Walder, and J. Weizeorick, "A fast, direct x-ray detection charge-coupled device," Rev. Sci. Instruments **80**, 083302 (2009).

[172] D. Doering *et al.*, "Development of a compact fast CCD camera and resonant soft x-ray scattering endstation for time-resolved pump-probe experiments," Rev. Sci. Instruments **82**, 073303 (2011).

[173] A. Koch, M. Kuster, J. Sztuk-Dambietz, and M. Turcato, "Detector Development for the European XFEL: Requirements and Status," J. Phys.: Conf. Ser. **425**, 062013 (2013).

[174] B. L. Henke, E. M. Gullikson, and J. C. Davis, "X-Ray Interactions: Photoabsorption, Scattering, Transmission, and Reflection at E = 50-30,000 eV, Z = 1-92," Atomic Data and Nuclear Data Tables **54**, 181 (1993).

[175] M. Beye, S. Schreck, F. Sorgenfrei, C. Trabant, N. Pontius, C. Schüßler-Langeheine, W. Wurth, and A. Föhlisch, "Stimulated x-ray emission for materials science," Nature **501**, 191 (2013).

[176] P. Glatzel and U. Bergmann, "High resolution 1s core hole X-ray spectroscopy in 3d transition metal complexes—electronic and structural information," Coordination Chemistry Reviews **249**, 65 (2005).

[177] N. Lee, T. Petrenko, U. Bergmann, F. Neese, and S. DeBeer, "Probing Valence Orbital Composition with Iron Kβ X-ray Emission Spectroscopy," J. Am. Chem. Soc. **132**, 9715 (2010).

[178] V. Kimberg and N. Rohringer, "Amplified X-Ray Emission from Core-Ionized Diatomic Molecules," Phys. Rev. Lett. **110**, 043901 (2013).

[179] V. Kimberg, S. B. Zhang, and N. Rohringer, "X-ray lasing in the CO molecule," J. Phys. B At. Mol. Opt. Phys. **46**, 164017 (2013).

[180] B. Friedrich and D. Herschbach, "Alignment and trapping of molecules in intense laser fields," Phys. Rev. Lett. **74**, 4623 (1995).

[181] H. Sakai, C. P. Safvan, J. J. Larsen, K. M. Hilligso/e, K. Hald, and H. Stapelfeldt, "Controlling the alignment of neutral molecules by a strong laser field," J. Chem. Phys. **110**, 10235 (1999).

[182] H. Stapelfeldt and T. Seideman, "*Colloquium* : Aligning molecules with strong laser pulses," Rev. Mod. Phys. **75**, 543 (2003).

[183] J. Rocca, C. Menoni, and M. Marconi, *X-Ray Lasers 2014: Proceedings of the 14th International Conference on X-Ray Lasers* (Springer, 2015).

Acknowledgements

I would like to thank my supervisor Dr. Nina Rohringer for taking me on as her first PhD student and giving me the opportunity to work in the emerging field of high-intensity x-ray physics. It has been a very exciting journey and I have learned so many things over the years. I am grateful for her patience with me and all the interesting discussions we had that conveyed her excitement about physics and was extremely encouraging.

I would also like to take the opportunity to thank all the members of our group that I have worked with over the years: Victor Kimberg, Marcus Dahlström, Felix Aviat, Jhih-An You, Song Bin Zhang, Wen-Te Liao, Miguel Silva and Laurent Mercadier. It has been a pleasure working with you and I have had a lot of fun with all of you.

I would also like to thank the team at LCLS for the support they provided during our beamtimes and without their help the experiments would not have been possible.

I am thankful for all the interesting people I have met at CFEL and through our IMPRS graduate school. Anja Bleidorn and Sonia Utermann did a great job of running the graduate school and I am glad I could be a part of it.

I am very grateful for all the support from my family and friends, who have helped me tremendously in accomplishing this PhD.

Eidesstattliche Versicherung

Hiermit erkläre ich an Eides statt, dass ich die vorliegende Dissertationsschrift selbst verfasst und keine anderen als die angegebenen Quellen und Hilfsmittel benutzt habe.

Hamburg, den ....

(Clemens Weninger)